

PREPARED FOR SUBMISSION TO JHEP

KOBE-COSMO-24-03, TUM-HEP-1522/24, DESY-24-131, CERN-TH-2025-072

Gravitational waves from first-order phase transitions: from weak to strong

Chiara Caprini,^{a,b} Ryusuke Jinno,^c Thomas Konstandin,^d Alberto Roper Pol,^{a,1}
Henrique Rubira,^e Isak Stomberg^{d,f,2}

^a*Département de Physique Théorique, Université de Genève, CH-1211 Genève, Switzerland*

^b*Theoretical Physics Department, CERN, CH-1211 Genève, Switzerland*

^c*Department of Physics, Kobe University, Kobe 657-8501, Japan*

^d*Deutsches Elektronen-Synchrotron DESY, Notkestr. 85, 22607 Hamburg, Germany*

^e*Physik Department T31, Technische Universität München James-Frank-Straße 1, D-85748 Garching, Germany*

^f*IFIC, Universitat de València-CSIC, C/ Catedrático José Beltrán 2, E-46980, Paterna, Spain*

E-mail: chiara.caprini@cern.ch, jinno@phys.sci.kobe-u.ac.jp,
thomas.konstandin@desy.de, alberto.roperpol@unige.ch,
henrique.rubira@tum.de, isak.stomberg@ific.uv.es

ABSTRACT: We study the generation of gravitational waves (GWs) during a cosmological first-order phase transition (PT) using the recently introduced Higgsless approach to numerically simulate the fluid motion induced by the PT. We present for the first time GW spectra sourced by bulk fluid motion in the aftermath of strong first-order PTs ($\alpha = 0.5$), alongside weak ($\alpha = 0.0046$) and intermediate ($\alpha = 0.05$) PTs, previously considered in the literature. We find that, for intermediate and strong PTs, the kinetic energy in our simulations decays, following a power law in time. The decay is potentially determined by non-linear dynamics and hence related to the production of vorticity. We show that the assumption that the source is stationary in time, characteristic of compressional motion in the linear regime (sound waves), agrees with our numerical results for weak PTs, since in this case the kinetic energy does not decay with time. We then provide a theoretical framework that extends the stationary assumption to one that accounts for the time evolution of the source: as a result, the GW energy density is no longer linearly increasing with the source duration, but proportional to the integral over time of the squared kinetic energy fraction. This effectively reduces the linear growth rate of the GW energy density and allows to account for the period of transition from the linear to the non-linear regimes of the fluid perturbations. We validate the novel theoretical model with the results of simulations and provide templates for the GW spectrum for a broad range of PT parameters.

ARXIV EPRINT: [2409.03651](https://arxiv.org/abs/2409.03651)

¹Corresponding author: alberto.roperpol@unige.ch

²Corresponding author: isak.stomberg@ific.uv.es

Contents

| | | |
|----------|--|-----------|
| 1 | Introduction | 1 |
| 2 | Gravitational waves from a phase transition | 4 |
| 2.1 | Bubble nucleation histories | 4 |
| 2.2 | Relativistic hydrodynamic equations | 5 |
| 2.3 | Gravitational wave production | 6 |
| 2.4 | Gravitational waves from stationary sound waves | 8 |
| 2.5 | Gravitational waves from decaying sources | 10 |
| 2.6 | Effect of the Universe expansion | 13 |
| 3 | Numerical setup | 15 |
| 3.1 | Updates to the numerical setup | 15 |
| 3.2 | Simulations and parameter choices | 17 |
| 4 | Numerical results | 19 |
| 4.1 | Convergence analysis of the kinetic energy and GW amplitude | 22 |
| 4.2 | Time evolution of the kinetic energy | 27 |
| 4.3 | Dependence of the integrated GW amplitude with the source duration and GW efficiency | 32 |
| 4.4 | Gravitational wave spectral shape | 39 |
| 5 | Summary and conclusions | 47 |
| A | Computation of the gravitational wave production in simulations | 53 |
| B | Corrections to the kinetic energy for multiple bubbles | 55 |
| C | Preliminary results for vorticity | 61 |
| C.1 | Vorticity on the lattice | 61 |
| C.2 | Velocity power spectra | 62 |

1 Introduction

The door to a new era with the promise of groundbreaking discovery was opened with the inaugural direct detections, by the LIGO-Virgo collaboration, of gravitational waves (GWs) emanating from mergers of black holes and neutron stars [1–3]. The forthcoming observing run by the LIGO-Virgo-KAGRA (LVK) collaboration are expected to accumulate more events [4]. Efforts among Pulsar Timing Array (PTA) collaborations have furthermore unveiled convincing evidence of a stochastic gravitational wave background (SGWB) at

nano-Hertz frequencies [5–8]. While a compelling candidate for the source of this radiation is the superposition of supermassive black hole mergers, implying an astrophysical origin, it is important to point out that primordial sources of cosmological origin can also explain the observed signal (see, e.g., Refs. [9, 10]). These breakthroughs in GW detection give us ears to astrophysical events and cosmological history inaccessible through other means of observation.

Looking into the 2030s, the launch of the Laser Interferometer Space Antenna (LISA) mission [11, 12], designed to probe GWs in the unexplored milli-Hertz frequency band, is setting the stage for a potential overhaul of modern cosmology [13–15]. Until the time of launch, joint strides in data analysis techniques and theoretical progress are necessary to leverage the full potential of the LISA mission once it flies. It is in this spirit that studies on cosmological SGWB production gain their motivation.

Cosmological sources of GWs that can be explored by LISA include inflation, particle production, topological defects, and primordial black holes throughout different stages of the expansion history of the Universe (see Refs. [16, 17] and references therein). Of particular interest is the phenomenon of first-order phase transitions (PTs) [18] that could have occurred in the early Universe. While the Standard Model (SM) predicts a crossover at the electroweak scale [19–21], many theories beyond the Standard Model accommodate a first-order electroweak PT (see Ref. [22] and references therein). During such a transition, the order parameter initially becomes trapped in a false vacuum expectation value in the symmetric phase. Subsequently, vacuum or thermal fluctuations locally induce a transition to the true vacuum in the broken phase, forming tiny seeds of bubbles [23–25]. The released vacuum energy drives the expansion of these bubbles, which eventually collide with each other, generating anisotropic stresses in the energy distribution and thus sourcing GWs. This process is highly non-thermal, suggesting that the baryon asymmetry of the Universe might have its origin in it [26–30]. While bubble collisions themselves are an important source of GWs [31–39], it has been shown in Ref. [40] that compressional fluid motion in the linearized regime (i.e., sound waves) induced in the primordial plasma by the scalar walls often dominates the GW production for PTs when the broken-phase bubbles do not run away,¹ which is expected to be the case unless the PT is dominated by vacuum, e.g., for supercooled PTs [22, 45–47]. This occurs when the friction exerted on the bubble walls by the fluid particles is strong enough to balance the vacuum energy released and, hence, the bubbles reach a terminal velocity [36, 40, 46, 48, 49].

The production of GWs from fluid perturbations can be decomposed in two contributions: sound waves (or, for generality, acoustic/compressional turbulence) [40, 50–61] and vortical turbulence [32, 53, 55, 62–73]. While analytical modeling of GW production from fluid perturbations is important [38, 51, 53, 54, 59, 64, 71, 74], numerical simulations are essential for a comprehensive understanding of the entire process. It is believed that after a first-order PT, the fluid motion initially manifests as compressional motion and then

¹These results have been found in the absence of magnetic fields and for small fluid perturbations. A primordial magnetic field generated or present during the PT, and/or the production of non-linear fluid perturbations, can efficiently induce vortical motion [41, 42] due to the high conductivity and Reynolds number of the primordial plasma [43, 44].

develops non-linearly, allowing for the formation of shocks and vorticity [57, 61, 75], and the subsequent development of turbulence [76, 77]. The non-linear evolution is inevitable due to the large Reynolds number of the fluid in the early Universe [44]. The transition from the fully compressional to the vortical turbulence regime can be especially important in strong transitions, when non-linearities can play an important role.

Currently, large-scale simulations have been performed by the Helsinki-Sussex group, which numerically solve a coupled scalar field-fluid system [40, 50, 52, 78]. First-order PTs in the early Universe exhibit a significant hierarchy: this is the hierarchy between the typical scales inherent in the order parameter field (including the thickness of the walls) and those in the cosmological fluid (including the bubble size and the sound-shell thickness). For the electroweak PT, the hierarchical separation can be as large as $M_{\text{Pl}}/T \sim 10^{16}$, being M_{Pl} the Planck mass. This fact naturally leads to the idea of the Higgsless scheme proposed by part of the authors of the present paper [56, 58]. In this scheme, the microphysics of the wall is introduced as a non-dynamical (although space and time dependent) energy-injecting boundary condition within the bag equation of state [49, 79, 80], and the bubble walls are assumed to have reached a terminal velocity, such that the fluid perturbations reach a self-similar solution in a very short time scale (much shorter than the time scale for collisions) [49]. See also Refs. [46, 81, 82] for discussions on the bubble wall terminal velocity. As a result, the scheme is able to capture the macroscopic dynamics necessary for GW production without being required to also solve for the hierarchically smaller scales.

In this paper, we explore the previously uncharted realm of GWs sourced by fluid perturbations induced in strong first-order PTs.² We also update results for weak and intermediate transitions and compare with other results in the literature [52, 54, 58]. We perform approximately 1000 simulations involving a parameter scan over wall velocities $v_w \in [0.32, 0.8]$ in increments of 0.04 for weak ($\alpha = 0.0046$), intermediate ($\alpha = 0.05$), and strong ($\alpha = 0.5$) PTs, using the Higgsless approach, to clarify the dependence on the underlying physical quantities of various characteristics of the GW spectrum, especially focusing on its overall integrated amplitude. We then assess the long-term evolution of the system, and discuss indications of non-linearities in the fluid bulk motion and their impact on the GW production. A thorough assessment of the vorticity production possibly associated to the non-linearities deserves a dedicated study; here we simply include an appendix presenting preliminary results on the longitudinal and transverse components of the velocity field spectra.

The outline of the paper is as follows. In Sec. 2, we review the GW production in a PT. We first describe the bubble nucleation history and the conservation laws of the fluid perturbations in Secs. 2.1 and 2.2. Then, Sec. 2.3 presents the prescription used to compute the GW spectrum at present time from the numerical results (more detail is given in App. A). In Sec. 2.4, we review the GW sourcing under the stationary assumption, characteristic of the sound-shell model (which assumes linear fluid perturbations) [51, 54, 59, 60], and used to interpret numerical results of GW generation in weak and intermediate

²We clarify that hereby, by strong transitions, we refer to $\alpha = 0.5$ (see Eq. (2.6) for definition), still far from the supercooled regime where the scalar field potential energy dominates the energy content of the Universe, allowing for $\alpha \gg 1$ [39, 83].

PTs [40, 50, 52, 56, 58]. We then present a novel model in Sec. 2.5 that extends the unequal time correlator (UETC) to a locally stationary UETC, allowing us to account for the effect of the source decay. In Sec. 2.6, we extend this model to include the effect of the expansion of the Universe. In Sec. 3, we discuss updates to the previous Higgsless simulations [58], and summarize the physical and numerical setup of the simulations. In Sec. 4, we discuss the numerical results. We first present a convergence analysis for the kinetic energy and the integrated GW amplitude in Sec. 4.1, which is combined with a convergence analysis of the potential effects of under-resolving the fluid perturbations at the level of the bubble profiles, presented in App. B. The result of these convergence analyses is an estimate of the kinetic energy fraction when the entire volume is converted to the broken phase, which is then compared to the single-bubble kinetic energy fraction commonly used in GW studies. We then analyse in Sec. 4.2 the time evolution of the kinetic energy fraction showing that it can be fitted by a decaying power law in time, accurately reproducing the simulations. To investigate the origin of the observed decay, we briefly discuss the development of vorticity in App. C, but we leave a detailed treatment of the onset of vorticity for future work. The growth of the GW integrated amplitude with the source duration is presented in Sec. 4.3, together with estimates of the GW efficiency $\tilde{\Omega}_{\text{GW}}$. We investigate the GW spectral shape in Sec. 4.4 and fit the numerical results to a double broken power law, providing estimates for the positions of the relevant spectral scales. We summarize our results in Sec. 5, and present a template for the GW spectrum, which we will make publicly available via [CosmoGW](#) [84].

2 Gravitational waves from a phase transition

In this section, we describe the production of gravitational waves from the fluid perturbations induced in the primordial plasma by the nucleation of bubbles in a first-order PT. In Sec. 2.1, we review the nucleation history of broken-phase bubbles that is used in the Higgsless approach, and in Sec. 2.2, we review the relativistic hydrodynamic equations. In Sec. 2.3, we describe how the GW generation is tackled within the Higgsless simulations, and discuss its applicability (see also App A for details). In Sec. 2.4, we review the production of GWs under the assumption that the anisotropic stress UETC is stationary. This is usually assumed in the literature when the source of GWs corresponds to sound waves [22, 40, 50–52, 54, 59, 85]. In Sec. 2.5, we propose an extension of the stationary model to a locally stationary UETC, allowing to account for the dynamics of a source that is decaying in time. We also provide a proxy to extend our results to the expanding Universe in Sec. 2.6. We validate the applicability of the proposed model to the integrated GW amplitude in Sec. 4 against the results from our numerical simulations, described in Sec. 3.

2.1 Bubble nucleation histories

In the Higgsless approach [58], a fundamental assumption is that the broken-phase bubbles reach a terminal wall velocity v_w due to the friction exerted by the fluid particles [46, 49, 81, 82], such that v_w can be prescribed as an input of the simulations. This enables the

construction of *bubble nucleation histories*, encompassing nucleation times and locations, as well as the *predetermined* expansion of the bubbles. We assume an exponentially increasing-in-time probability of bubble nucleation, $P(t) \simeq P_n \exp[\beta(t - t_n)]$, where β determines the usual rate of bubble nucleation evaluated at the nucleation time t_n , such that the action S has been Taylor-expanded around this time [22]. The time dependence is hereby inherited from the temperature dependence of the tunnelling action S/T and the fact that the temperature scales inversely with the scale factor

$$\beta = \frac{d}{dt} \left(\frac{S}{T} \right) \Big|_{t=t_n} = -H T \frac{d}{dT} \left(\frac{S}{T} \right) \Big|_{T=T_n}, \quad (2.1)$$

where H is the Hubble scale. A detailed description of how such bubble nucleation histories are constructed is found in Ref. [58], and examples of how modified bubble nucleation histories can be constructed are found in Refs. [86, 87]. We note that in previous numerical work [50, 52, 78], bubbles are nucleated simultaneously. This is expected to have an impact on the spectral peak and the amplitude, but not on the spectral shape [52, 88].

2.2 Relativistic hydrodynamic equations

The relativistic hydrodynamic equations of motion are derived from the conservation of the energy-momentum tensor $T^{\mu\nu}$, which, in Minkowski space-time reads

$$\partial_\mu T^{\mu\nu} = 0. \quad (2.2)$$

These equations of motion hold during the PT under the assumption that the duration of the transition is much shorter than a Hubble time, i.e., $\beta/H_* \gg 1$, which allows to neglect the expansion of the Universe. They can also be applied to the fluid motion after the PT ends if the fluid is dominated by radiation particles: indeed, the conservation laws then become conformally invariant and hence reduce to those in Minkowski space-time by a conformal transformation [42, 89, 90]. We take $T^{\mu\nu}$ to be that of a perfect fluid

$$T^{\mu\nu} = u^\mu u^\nu w - \eta^{\mu\nu} p, \quad (2.3)$$

where $u^\mu = \gamma(1, v^i)$ is the fluid four-velocity, $\gamma = 1/\sqrt{1 - v^2}$ is the Lorentz factor, w and p are respectively the enthalpy and pressure in the system, and $\eta^{\mu\nu} = \text{diag}\{1, -1, -1, -1\}$ is the Minkowski metric tensor. The equations of motion couple to the state of the vacuum through the bag equation of state, for which we take the sound speed to be $c_s^2 = 1/3$,

$$p = \frac{1}{3} a T^4 - \epsilon, \quad w = T \frac{dp}{dT} = \frac{4}{3} a T^4, \quad (2.4)$$

with T being the temperature. The *bag constant* ϵ [49], defined as the difference in vacuum energy density between the symmetric and broken phases, is thus promoted to a time- and space-dependent quantity

$$\epsilon(t, \mathbf{x}) = \begin{cases} 0 & \text{inside bubbles,} \\ \epsilon & \text{outside bubbles,} \end{cases} \quad (2.5)$$

whose time evolution is uniquely determined for each bubble nucleation history by the terminal wall velocity v_w . We therefore neglect the model-dependent possibility that heating in the broken phase can slow down the expansion of the Higgs front when the latter propagates as a deflagration [78], and also that strong PTs can potentially lead to runaway behavior [46, 91, 92].

The relevant quantity for boundary conditions of the fluid at the Higgs interface is the difference in the trace of the energy-momentum tensor, $\theta = w - 4p$, normalized by the mean enthalpy at the nucleation temperature [80],

$$\alpha = \frac{\Delta\theta}{3w_n} = \frac{4\epsilon}{3w_n}, \quad (2.6)$$

where the second equality holds within the bag equation of state. We use this quantity in the following to parameterize the strength of the PT in the system [22]. The conservation laws for a relativistic perfect fluid are

$$\begin{aligned} \partial_t T^{00} + \nabla_i T^{i0} &= 0, \\ \partial_t T^{j0} + \nabla_i T^{ij}(T^{\mu 0}, \epsilon) &= 0. \end{aligned} \quad (2.7)$$

Note that $T^{ij}(T^{\mu 0}, \epsilon)$ depends on the state of the vacuum such that, effectively, the expanding bubbles perturb the fluid as the latent heat of the vacuum is (locally) deposited. For more details on these equations, we refer the reader to the original Higgsless reference [58] and the review [90].

2.3 Gravitational wave production

The GW spectrum as a present-time observable is computed using the following relation

$$\Omega_{\text{GW}}(k) = \frac{1}{\rho_{\text{tot}}} \frac{d\rho_{\text{GW}}}{d \ln k} = 3 \mathcal{T}_{\text{GW}} \left(\frac{H_*}{\beta} \right)^2 \mathcal{I}(k), \quad (2.8)$$

where ρ_{tot} is the total energy density of the Universe at present time, \mathcal{T}_{GW} is the transfer function given in Eq. (A.8), and k is the physical wave number, which can be converted to the frequency as $f = k/(2\pi)$.

The function $\mathcal{I}(k)$ represents the spectrum of the stochastic GW signal, and it is given by a double time integral of the anisotropic stress UETC, $E_{\Pi}(t_1, t_2, k)$ (see Eq. (A.10) in App. A), multiplied by the Green's function of the GW equation. We have introduced the prefactor $(H_*/\beta)^2$ in Eq. (2.8) to express \mathcal{I} in normalized time and wave number units $\tilde{t} \equiv t\beta$ and $\tilde{k} \equiv k/\beta$ (see App. A, in particular Eq. (A.11), for its derivation from the solution of the GW equation),

$$\mathcal{I}(\tilde{t}_*, \tilde{t}_{\text{fin}}, \tilde{k}) = \frac{k}{2} \int_{\tilde{t}_*}^{\tilde{t}_{\text{fin}}} \int_{\tilde{t}_*}^{\tilde{t}_{\text{fin}}} E_{\Pi}(\tilde{t}_1, \tilde{t}_2, \tilde{k}) \cos(\tilde{k}\tilde{t}_-) d\tilde{t}_1 d\tilde{t}_2, \quad (2.9)$$

where $\tilde{t}_- = \tilde{t}_1 - \tilde{t}_2$. Here \tilde{t}_* and \tilde{t}_{fin} denote the initial and final times of action of the GW source. In Eq. (2.9), the expansion of the Universe is not taken into account, and it therefore holds only if the GW production process lasts for less than one Hubble time,

$\tau_{\text{fin}} \equiv t_{\text{fin}} - t_* \ll H_*^{-1}$, where H_* is the Hubble rate at the PT time t_* . The fact that the duration of the PT, determined by the inverse of the nucleation rate β^{-1} , satisfies $\beta/H_* \geq 1$, does not imply that the GW sourcing time is also short. In particular, for GWs generated by fluid motion, the time scale of dissipation of the fluid kinetic energy is typically much longer than one Hubble time, as it is set by the kinematic viscosity in the early Universe, which is very small [44, 65]. However, the Higgless simulations are performed in Minkowski space-time, and therefore we neglect the Universe expansion in Eq. (2.9) and the following, to connect with the simulations formalism. We discuss in Sec. 2.6 how to extend our results to an expanding Universe.

The anisotropic stress UETC $E_{\Pi}(\tilde{t}_1, \tilde{t}_2, \tilde{k})$ can be estimated numerically. In particular, within the Higgless simulations, this numerical estimate leads to the following expression of the GW spectrum (see Eq. (A.15) and Refs. [56, 58]), given in the normalized units of the simulation

$$\mathcal{I}_{\text{sim}}(\tilde{t}_*, \tilde{t}_{\text{fin}}, \tilde{k}) = \frac{\tilde{k}^3}{4\pi^2 \tilde{V}} \int_{\Omega_{\tilde{k}}} \frac{d\Omega_{\tilde{k}}}{4\pi} \Lambda_{ijlm}(\hat{\mathbf{k}}) [\tilde{T}_{ij}(\tilde{t}_*, \tilde{t}_{\text{fin}}, \tilde{q}, \tilde{\mathbf{k}}) \tilde{T}_{lm}^*(\tilde{t}_*, \tilde{t}_{\text{fin}}, \tilde{q}, \tilde{\mathbf{k}})]_{\tilde{q}=\tilde{k}}, \quad (2.10)$$

being $\tilde{V} \equiv V\beta^3$ and Λ_{ijlm} the transverse and traceless operator

$$\Lambda_{ijlm}(\hat{\mathbf{k}}) = P_{il}P_{jm} - \frac{1}{2}P_{ij}P_{lm}, \quad \text{with } P_{ij} = \delta_{ij} - \hat{k}_i\hat{k}_j. \quad (2.11)$$

The function $\tilde{T}_{ij}(\tilde{t}_*, \tilde{t}_{\text{fin}}, \tilde{q}, \tilde{\mathbf{k}})$ is computed from the normalized stress-energy tensor $\tilde{T}_{ij}(t, \mathbf{x})$, sourcing the GWs, as [see Eq. (A.14)]

$$\tilde{T}_{ij}(\tilde{t}_*, \tilde{t}_{\text{fin}}, \tilde{q}, \tilde{\mathbf{k}}) = \int_{\tilde{t}_*}^{\tilde{t}_{\text{fin}}} d\tilde{t} e^{i\tilde{q}\tilde{t}} \int d^3\tilde{\mathbf{x}} e^{-i\tilde{\mathbf{k}}\cdot\tilde{\mathbf{x}}} \tilde{T}_{ij}(\tilde{t}, \tilde{\mathbf{x}}), \quad (2.12)$$

where $\tilde{T}_{ij}(t, \mathbf{x}) = w\gamma^2 v_i v_j / \bar{\rho}$, and $\bar{\rho} = \frac{3}{4}\bar{w} + \epsilon = \frac{3}{4}(1 + \alpha)\bar{w}$ is the average total energy density [see Eqs. (2.4) and (2.6)].

As shown in App. A, using Eq. (2.10) one can directly obtain from the simulation a quantity equivalent to the GW spectrum at present time [see Eq. (2.8)], under two assumptions: first, that the statistical homogeneity and isotropy of the early Universe can be accounted for through an angular integration over shells with fixed wave number k over the simulated single realization of the normalized source $\tilde{T}_{ij}(\tilde{t}_{\text{init}}, \tilde{t}_{\text{end}}, \tilde{q}, \tilde{\mathbf{k}})$; second, that the source has stopped operating by the end of the simulation \tilde{t}_{end} . Indeed, Eq. (2.8) implies a time average over oscillations at present time, which can be performed only when $\tilde{t} \gg \tilde{t}_{\text{fin}}$. However, it is often not computationally affordable to run a simulation until \tilde{t}_{fin} , especially for slowly decaying sources. In practice, the quantity $\tilde{T}_{ij}(\tilde{t}_{\text{init}}, \tilde{t}_{\text{end}}, \tilde{q}, \tilde{\mathbf{k}})$ is computed in the simulation over an interval of time $\tilde{t} \in (\tilde{t}_{\text{init}}, \tilde{t}_{\text{end}})$, where the sole criterion in choosing \tilde{t}_{end} is computational feasibility. However, the GW source has effectively stopped operating at a given wave number \tilde{k} also whenever the amplitude of the GW spectrum on that mode has reached its saturation amplitude, entering its free-propagation regime (cf. discussion in App. A). Therefore, the GW spectrum evaluated from the simulation is accurate for any wave number \tilde{k} that has already reached its saturated amplitude by the end of the simulation at \tilde{t}_{end} , even if $\tilde{t}_{\text{end}} < \tilde{t}_{\text{fin}}$. On the other hand, not all the modes in our

simulations have reached this regime. As in previous numerical work [40, 50, 52, 56, 58, 78], one therefore needs to take into account this limitation when interpreting the numerical results, especially for the low- k tail of the GW spectrum and for its peak amplitude [59], as we discuss in Sec. 4.

In the following, we will propose extending the stationary UETC usually assumed for sound waves (see Sec. 2.4) to a locally stationary UETC that can incorporate the decay of the source with time observed in the simulations of strong PTs and of some intermediate ones (see Sec. 2.5). As we will see, the proposed model will allow us to extrapolate our results from the final time of the simulations till the final time of GW production t_{fin} , to estimate the amplitude of the present-day GW spectrum. Note that also numerical viscosity, which in the simulations can dissipate kinetic energy over time, could limit the time and \tilde{k} range for which the simulations can actually be accurate. This can potentially affect the transfer of energy from the fluid perturbations to GWs, especially at large \tilde{k} .

2.4 Gravitational waves from stationary sound waves

In this section, we review the theoretical modeling of the GW production from sound waves from previous work. This is useful since we will present our numerical results in terms of quantities previously used in the literature,³ and also as an introduction to the formalism used in the next section to model decaying sources.

In the context of GW production from sound waves, it has extensively been assumed that the UETC is stationary, i.e., it only depends on the difference $t_- = t_1 - t_2$ [40, 50–54, 59, 62, 64, 93, 94],

$$E_{\Pi}(t_1, t_2, k) = 2 k^2 K^2 f(t_-, k), \quad (2.13)$$

where $K = \rho_{\text{kin}}/\bar{\rho}$ is the time-independent kinetic energy fraction, with $\rho_{\text{kin}} = \langle w\gamma^2 v^2 \rangle$ the mean kinetic energy density of the system. Note that the source is considered *stationary* but only within a finite duration $\tilde{\tau}_{\text{fin}} = \tilde{t}_{\text{fin}} - \tilde{t}_*$. Under the assumption of Eq. (2.13), Eq. (2.9) becomes

$$\mathcal{I}(\tilde{t}_*, \tilde{t}_{\text{fin}}, \tilde{k}) = k^3 K^2 \int_{\tilde{t}_*}^{\tilde{t}_{\text{fin}}} d\tilde{t} \int_{\tilde{t}_* - \tilde{t}}^{\tilde{t}_{\text{fin}} - \tilde{t}} \cos(k t_-) f(\tilde{t}_-, \tilde{k}) d\tilde{t}_-. \quad (2.14)$$

In the sound-shell model of Refs. [51, 54], the limits of the integral over \tilde{t}_- get extended to $\pm\infty$, allowing to separate the two integrals, such that the integral over \tilde{t} becomes the source duration, $\tilde{\tau}_{\text{fin}}$. Therefore, within the sound-shell model, the GW amplitude depends linearly on the source duration. The proportionality to $\tilde{\tau}_{\text{fin}}$ has usually been assumed in the literature, especially, but not exclusively, for GW production from sound waves [22, 40, 50–52, 54, 62, 93]. The duration of the sound-wave phase can be assumed to correspond to the shock time, which determines the time it takes for non-linearities and vorticity to develop in the fluid, $\tilde{\tau}_{\text{fin}} \equiv \tau_{\text{fin}}\beta \sim \tilde{\tau}_{\text{sh}} = \beta R_*/\sqrt{K}$, with $\beta R_* \equiv (8\pi)^{1/3} \max(v_w, c_s)$ being the mean

³The simulations concern the full hydrodynamical system, from initial compressional motion to the possible development of large fluid perturbations, which can occur in intermediate to strongly first order PTs. On the other hand, when the PT is weak, the linearized regime of fluid perturbations holds, and indeed we will see that the simulations recover the sound-wave system described in previous work.

separation of the bubbles at the end of the PT [22]. The aforementioned assumption that the integration limits get extended to $\pm\infty$ holds when the support of the UETC $f(\tilde{t}_-, \tilde{k})$ is small enough. In the sound-wave case, the UETC is highly oscillatory, and Ref. [59] has shown that, at the level of the GW spectrum, the assumption holds in the region $k\tau_{\text{fin}} \sim kR_*/\sqrt{K} \gg 1$. When $\tau_{\text{fin}}/R_* \sim 1/\sqrt{K} \gg 1$, i.e., when the kinetic energy is small, this covers all relevant wave numbers $kR_* \gg \sqrt{K}$, including the spectral breaks occurring at $k \gtrsim 1/R_*$ (see Sec. 4.4). However, if the kinetic energy is large, the GW spectrum gets modified with respect to the sound-shell prediction [59] of previous work [51, 54]. Finally, it can be shown that under the same assumptions, the remaining integral over \tilde{t}_- in Eq. (2.14) is proportional to $(\beta R_*)/c_s$ (see for instance App. B of Ref. [59]), such that

$$\mathcal{I}(\tilde{t}_*, \tilde{t}_{\text{fin}}, \tilde{k}) = \tilde{\Omega}_{\text{GW}} K^2 \beta R_* \tilde{\tau}_{\text{fin}} S(kR_*), \quad (2.15)$$

where we have absorbed the $1/c_s$ factor⁴ in $\tilde{\Omega}_{\text{GW}}$, which denotes the GW production efficiency, and S is a normalized spectral shape satisfying $\int d\ln k S(k) = 1$. Using Eq. (2.8), the final GW spectrum can be written as [22, 40, 50–52, 54, 59, 96, 97]

$$\Omega_{\text{GW}}(k) = 3 \mathcal{T}_{\text{GW}} \tilde{\Omega}_{\text{GW}} K^2 H_* R_* H_* \tau_{\text{fin}} S(kR_*). \quad (2.16)$$

As done in previous numerical studies [40, 50, 52, 54], the GW production efficiency $\tilde{\Omega}_{\text{GW}}$, in the situation in which the GW generation scales linearly with the source duration, can be estimated from the simulations via

$$\tilde{\Omega}_{\text{GW}} = \frac{\mathcal{I}_{\text{sim}}^{\text{int}}}{K^2 \beta R_* \tilde{T}_{\text{GW}}}, \quad (2.17)$$

where $\mathcal{I}_{\text{sim}}^{\text{int}} = \int d\ln k \mathcal{I}_{\text{sim}}$ [see Eqs. (2.10) and (2.15)], and $\tilde{T}_{\text{GW}} = \tilde{t}_{\text{end}} - \tilde{t}_{\text{init}}$ is the time interval of the simulation in which Eq. (2.10) is evaluated. We will use similar expressions to Eq. (2.17) in Sec. 4 to analyze our results. In particular, we will show that Eq. (2.15) and in turn (2.16) well describe the simulation results as long as the kinetic energy remains approximately constant in time after the PT ends, i.e., for weak PTs. For intermediate and strong PTs, on the other hand, the simulations show a decay in time of the kinetic energy. This requires a generalization of the stationary UETC assumption of Eq. (2.13), which is described in Sec. 2.5. We find that the GW spectrum (2.16) in this case is proportional to the time integral of K^2 , instead of to $K^2 \tau_{\text{fin}}$. This model is accurately validated by the numerical results in Sec. 4.3, and allows to still compute numerically the GW efficiency $\tilde{\Omega}_{\text{GW}}$, and estimate the expected final GW amplitude at the final time of GW production, even when the GW production does not scale linearly with the source duration.

Alternatively, previous work on Higgsless simulations presented the results for the GW amplitude in terms of the following parameterization [56, 58]:

$$Q'(k) = \left(\frac{\bar{\rho}}{\bar{w}}\right)^2 \frac{4\pi^2}{\tilde{T}_{\text{GW}}} \mathcal{I}_{\text{sim}}(\tilde{t}_{\text{init}}, \tilde{t}_{\text{end}}, \tilde{k}) \approx \frac{9\pi^2}{4\tilde{T}_{\text{GW}}} (1 + \alpha)^2 \mathcal{I}_{\text{sim}}(\tilde{t}_*, \tilde{t}_{\text{fin}}, \tilde{k}), \quad (2.18)$$

⁴In this paper, we do not study the dependence of the GW signal on c_s . For a study of the c_s dependence in the sound-shell model see, e.g., Ref. [95].

where the prefactor $(\bar{\rho}/\bar{w})^2$ in Eq. (2.18) takes into account that the authors in Refs. [56, 58] used the mean enthalpy to normalize T_{ij} in the definition of Q' instead of the total energy density $\bar{\rho}$, as done in our case [see text below Eq. (2.12)]. References [56, 58] found a strong dependence of the parameter $Q'/K^2 \sim \mathcal{I}_{\text{sim}}/(K^2 \tilde{T}_{\text{GW}})$ with v_w , and concluded that $\mathcal{I}_{\text{sim}} \sim K_\xi^2 \xi_{\text{shell}} \tilde{T}_{\text{GW}}$ [where K_ξ is given in Eq. (2.19) and ξ_{shell} in Eq. (4.15)]. However, in this paper we find that inserting R_* in Eq. (2.15) to describe the GW amplitude, instead of using Q'/K^2 , provides the right GW efficiency $\tilde{\Omega}_{\text{GW}}$, which is virtually independent of both v_w and the duration of the source τ_{fin} (see Sec. 4.3). This is connected to the fact that the GW source is the bulk fluid motion and not the bubble collisions. Therefore, normalizing with quantities characteristic of the PT, such as H_*/β , instead of with quantities characteristic of the fluid, such as $H_* R_*$, can lead to misinterpretation [64]. Indeed, the fluid is set into motion by the bubbles, whose characteristic scale is R_* after the end of the PT, and evolves with its own dynamical timescale afterwards; the duration of the PT, H_*/β , on the other hand, does not directly influence the fluid dynamics. The same consideration applies to the breaks of the GW spectrum, which should also be normalized with R_* . This intuitive argument is confirmed with simulations in the present analysis (cf. Sec. 4).

The kinetic energy fraction K is usually taken to be the one corresponding to a single bubble, which can be expressed as

$$K_\xi \equiv \frac{\kappa_\xi \alpha}{1 + \alpha}, \quad (2.19)$$

where α characterizes the strength of the PT [see Eq. (2.6)], and $\kappa_\xi \equiv \rho_{\text{kin}}^{\text{sb}}/\epsilon < 1$ is the single-bubble efficiency factor, where $\rho_{\text{kin}}^{\text{sb}}$ denotes the kinetic energy density of a single bubble [49]. We compare in Sec. 4 the kinetic energy fraction found in the simulations K with the single-bubble one, showing that the effect of collisions and non-linear dynamics alters the kinetic energy fraction with respect to K_ξ . Note that, in the sound-shell model, $K \neq K_\xi$ is time-independent but the exact value of $K/K_\xi \sim \mathcal{O}(1)$ depends on the PT parameters [51, 54, 59]. Similarly, Refs. [52, 78] have also reported maximum values of the kinetic energy fraction K_{max} in their simulations that differ from K_ξ . Therefore, using K_ξ for the GW production [cf. Eq. (2.16)] might lead to a wrong estimate of the amplitude.

2.5 Gravitational waves from decaying sources

As we show in Sec. 4, for strong and intermediate PTs, the kinetic energy starts to decay within the duration of the simulations, potentially due to the fact that the system enters the non-linear regime. Consequently, the linear scaling of the GW amplitude with τ_{fin} changes, impeding the use of Eq. (2.15) to estimate the GW efficiency.

In order to analyze such cases, we propose a generalization of Eq. (2.13), assuming a locally stationary UETC that allows to account for the time dependence of K^2 :

$$E_\Pi(t_1, t_2, k) = 2 k^2 K^2(t_+) f(t_-, k), \quad (2.20)$$

where $t_+ = \frac{1}{2}(t_1 + t_2)$. Note that locally-stationary kernels are acceptable as UETCs, since they give rise to positive-definite GW spectra (see discussion in Refs. [65, 72]). Then,

under the same approximation discussed above, i.e., that the two integrals in \tilde{t} and \tilde{t}_- of Eq. (2.14) can be separated by sending the limits of the one in \tilde{t}_- to $\pm\infty$, we find [59]

$$\mathcal{I}(\tilde{t}_*, \tilde{t}_{\text{fin}}, \tilde{k}) = k^3 \int_{\tilde{t}_*}^{\tilde{t}_{\text{fin}}} K^2(\tilde{t}_+) d\tilde{t}_+ \int_{-\infty}^{\infty} \cos(k\tilde{t}_-) f(\tilde{t}_-, \tilde{k}) d\tilde{t}_-, \quad (2.21)$$

such that $K^2 \tilde{\tau}_{\text{fin}}$ in Eq. (2.15) can be substituted by K_{int}^2 ,

$$K_{\text{int}}^2(\tilde{t}_*, \tilde{t}_{\text{fin}}) \equiv \int_{\tilde{t}_*}^{\tilde{t}_{\text{fin}}} K^2(\tilde{t}) d\tilde{t}. \quad (2.22)$$

This yields

$$\mathcal{I}(\tilde{t}_*, \tilde{t}_{\text{fin}}, \tilde{k}) = \tilde{\Omega}_{\text{GW}} K_{\text{int}}^2(\tilde{t}_*, \tilde{t}_{\text{fin}}) (\beta R_*) S(kR_*), \quad (2.23)$$

and the resulting GW spectrum is

$$\Omega_{\text{GW}}(k) = 3 \mathcal{T}_{\text{GW}} \tilde{\Omega}_{\text{GW}} \frac{H_*}{\beta} K_{\text{int}}^2 H_* R_* S(kR_*). \quad (2.24)$$

Note that K_{int}^2 reduces to $K^2(\tilde{t}_{\text{fin}} - \tilde{t}_*) = K^2 \tilde{\tau}_{\text{fin}}$ when K^2 is constant in time and one recovers Eq. (2.15) found in the stationary assumption. As already discussed in Sec. 2.4, when the UETC of the sound waves is provided solely by $f(t_-, k)$, the two integrals of Eq. (2.14) can be separated only for $k\tau_{\text{fin}} \gg 1$. The same applies in this case as the introduction of $K(t_+)$ in the UETC does not affect the integral over t_- in Eq. (2.21). These wave numbers include the peak of the GW spectrum when $\tau_{\text{fin}} \gg R_*$, meaning $\sqrt{K} \ll 1$. This last condition might seem at odds with the fact that we will apply this formalism to intermediate and strong PTs. Note, however, that the fluid kinetic energy fraction always remains small, of the order of the single-bubble one, K_ξ , even for intermediate and strong PTs [see Eq. (2.19) and Tab. 3]. Only for PTs where the vacuum energy dominates and the radiation component can be neglected, i.e., $\alpha \gtrsim 1$, one can reach values $K \sim 1$.

A similar UETC to the one in Eq. (2.20) has been considered, e.g., in Refs. [53, 61],

$$E_v(t_1, t_2, k) = \sqrt{E_v(t_1, k) E_v(t_2, k)} \cos(kc_s t_-), \quad (2.25)$$

where $E_v(k)$ is the velocity spectrum at equal times $t_1 = t_2$, defined such that

$$\langle v^2 \rangle = \int_0^\infty dk E_v(k). \quad (2.26)$$

The integral over t_1 and t_2 of this UETC can be reduced to the integral in Eq. (2.22) under the aforementioned assumptions (see discussion in Sec. V of Ref. [59]) and for small fluid perturbations. Therefore, we expect both UETCs to have the same impact on the integrated GW amplitude. Further analyses are necessary to understand how different UETCs influence the GW signal spectral shape.

We show in Sec. 4.2 that the kinetic energy evolution in the simulations can be fit with a decaying power law,

$$K(\tilde{t} > \tilde{t}_0) = K_0 \left(\frac{\Delta \tilde{t}}{\Delta \tilde{t}_0} \right)^{-b}, \quad (2.27)$$

where $b \geq 0$ and K_0 are parameters to be extracted from the numerical results, and \tilde{t}_0 corresponds to the time at which all the simulation box is in the broken phase, and the decay of the kinetic energy is well in place (see Sec. 4.2). $\Delta\tilde{t}$ and $\Delta\tilde{t}_0$ in Eq. (2.27) are time intervals with respect to the time-coordinate origin in the simulations, \tilde{t}_{ref} . Since the choice of \tilde{t}_{ref} is arbitrary, the value of $\Delta\tilde{t}_0$ should be considered as a parameter of the numerical fit. Similarly, one has $\Delta\tilde{t} = \tilde{t} - \tilde{t}_0 + \Delta\tilde{t}_0$, where only the interval of time since the end of the PT, $\tilde{t} - \tilde{t}_0$, is physically relevant.

Note that the decay rate exponent b could in principle be predicted within a physical model for the dynamical evolution of the fluid, and then compared to the simulation results, as done for instance in the case of magnetohydrodynamic turbulence, for which theoretical predictions on the decay rate exponent exist (see, e.g., Ref. [77]). However, this is still premature at the level of the present analysis, since we are missing such a model (even though a possible interpretation of the decay observed in simulations as due to the development of non-linearities is emerging in our results). For the kinetic energy fraction K_0 , on the other hand, there is an available proxy, i.e., the single-bubble one, K_ξ . We indeed study the relation between K_0 and K_ξ and analyze its dependence on the numerical discretization in Sec. 4.1 and App. B. We find that K_0 is not exactly K_ξ , as a consequence of the effects due to collisions during the PT. The simulations show that $K(\tilde{t})$ grows initially, proportional to the volume of the simulation in the broken phase (see App. B). Then, it reaches a peak value and enters the decay stage at times that are practically the same across the tested values of α and v_w (cf. Fig. 4).

From Eq. (2.22), using Eq. (2.27), we find that the dependence of K_{int}^2 with the source duration, $\tilde{\tau}_{\text{fin}} = \tilde{t}_{\text{fin}} - \tilde{t}_*$, is

$$K_{\text{int}}^2(\Delta\tilde{t}_*, \tilde{\tau}_{\text{fin}}) = K_0^2 \Delta\tilde{t}_* \left(\frac{\Delta\tilde{t}_0}{\Delta\tilde{t}_*} \right)^{2b} \frac{(1 + \tilde{\tau}_{\text{fin}}/\Delta\tilde{t}_*)^{1-2b} - 1}{1 - 2b}, \quad (2.28)$$

where we have introduced $\Delta\tilde{t}_* = \tilde{t}_* - \tilde{t}_0 + \Delta\tilde{t}_0$, and assumed that the GW production starts at $\tilde{t}_* \geq \tilde{t}_0$. Again, only the time interval $\tilde{t}_* - \tilde{t}_0$ is physically meaningful. When the source duration is very short $\tilde{\tau}_{\text{fin}}/\Delta\tilde{t}_* \ll 1$, this expression reduces to $K_{\text{int}}^2 \rightarrow K_0^2 \tilde{\tau}_{\text{fin}} (\Delta\tilde{t}_0/\Delta\tilde{t}_*)^{2b}$ for any value of b : indeed, in this case, the integral can be approximated as the product of the integrand evaluated at the lower boundary $\Delta\tilde{t}_*$ multiplied by the time interval itself, i.e., the source duration, and one goes back to the linear dependence with $\tilde{\tau}_{\text{fin}}$ as in the stationary source case, in which the kinetic energy is assumed constant in time (see Sec. 2.4). For long duration $\tilde{\tau}_{\text{fin}}/\Delta\tilde{t}_* \gg 1$, on the other hand, Eq. (2.28) takes the following asymptotic limits:

$$\begin{aligned} \lim_{\tilde{\tau}_{\text{fin}} \gg \Delta\tilde{t}_*} K_{\text{int}}^2(\tilde{\tau}_{\text{fin}}) &= \frac{K_0^2 \Delta\tilde{t}_0}{1 - 2b} \left(\frac{\tilde{\tau}_{\text{fin}}}{\Delta\tilde{t}_0} \right)^{1-2b}, & \text{when } 0 \leq b < \frac{1}{2}, \\ \lim_{\tilde{\tau}_{\text{fin}} \gg \Delta\tilde{t}_*} K_{\text{int}}^2(\Delta\tilde{t}_*) &= \frac{K_0^2 \Delta\tilde{t}_*}{2b - 1} \left(\frac{\Delta\tilde{t}_0}{\Delta\tilde{t}_*} \right)^{2b}, & \text{when } b > \frac{1}{2}. \end{aligned} \quad (2.29)$$

Hence, when the decay is sufficiently slow, $0 \leq b < 1/2$, K_{int}^2 is proportional to $\tilde{\tau}_{\text{fin}}^{1-2b}$, thus generalizing the linear dependence with $\tilde{\tau}_{\text{fin}}$ obtained in the stationary assumption

to a shallower growth with the source duration in the case of a slowly decaying source. On the other hand, when the decay rate is fast, $b > 1/2$, K_{int}^2 saturates to a fixed value, independent of the source duration. If $b = 1/2$, the dependence with $\tilde{\tau}_{\text{fin}}$ is logarithmic.

Equation (2.23) generalizes the description of the GW production to a decaying source, for which the assumption of local stationarity in time holds. It allows us to go beyond the usual assumption of the sound-shell model, valid for weak PTs, and it also allows us to estimate the GW efficiency $\tilde{\Omega}_{\text{GW}}$ when the kinetic energy is decaying with time, cf. Eq. (4.11). In Secs. 4.2 and 4.3, we validate the proposed model for the integrated GW amplitude and Eqs. (2.23) and (2.28) with the results of numerical simulations.

2.6 Effect of the Universe expansion

Neglecting the expansion of the Universe, the sound-shell model finds that a superposition of sound waves emits GWs with an amplitude proportional to the source duration τ_{fin} (see Eq. (2.16) and Refs. [40, 50–52, 54, 59, 62–64, 94, 96, 97]). This linear dependence on the source duration is typical of stationary sources when back-reaction (in this case, the decay of the source due to the GW production) is not taken into account. In the case of sound waves, the unbounded linear increase is expected to be cut off by the development of non-linearities. The locally stationary UETC proposed in Sec. 2.5 allows to account for a non-linear source that is decaying in time. We have found that, for a power-law decay with exponent $-b$, when the decay rate of the kinetic energy is slow enough, $b < 1/2$, the GW amplitude still increases unbounded proportional to τ_{fin}^{1-2b} [see Eq. (2.29)]. On the other hand, it saturates when $b > 1/2$.

Naturally, the expansion of the Universe inserts an extra decay component, changing the dependence of the GW spectrum with the source duration. In the stationary UETC case, to take into account the expansion of the Universe, the linear dependence with $H_*\tau_{\text{fin}}$ of Eq. (2.16) can be substituted by the factor $\Upsilon(\mathcal{H}_*\delta\eta_{\text{fin}}) = \mathcal{H}_*\delta\eta_{\text{fin}}/(1 + \mathcal{H}_*\delta\eta_{\text{fin}})$ [59, 93], where $\delta\eta_{\text{fin}} \equiv \eta_{\text{fin}} - \eta_*$ is the source duration in conformal time, and $\mathcal{H}_* = H_*a_*$ is the conformal Hubble rate:

$$\Omega_{\text{GW,exp}}(k) = 3 \mathcal{T}_{\text{GW}} \tilde{\Omega}_{\text{GW}} K^2 \frac{\mathcal{H}_*\delta\eta_{\text{fin}}}{1 + \mathcal{H}_*\delta\eta_{\text{fin}}} \mathcal{H}_* \mathcal{R}_* S_{\text{exp}}(k_c \mathcal{R}_*). \quad (2.30)$$

$\mathcal{R}_* = R_*/a_*$ and $k_c = a_*k$ are the comoving mean-bubble separation and wave number, such that $\mathcal{H}_*\mathcal{R}_* = H_*R_*$ and $k_c\mathcal{R}_* = kR_*$.

It is important to remark that, when including expansion, the results are no longer invariant under time translations, so we need to choose absolute values for conformal times. Assuming that the PT completes faster than one Hubble time, and that the GW sourcing occurs during radiation domination, we can set the initial and final conformal times of GW production to be $\mathcal{H}_*\eta_* = 1$ and $\mathcal{H}_*\eta_{\text{fin}} = 1 + \mathcal{H}_*\delta\eta_{\text{fin}}$ (one could also then normalize to $a_* = 1$, such that the conformal Hubble rate is $\mathcal{H}_* = H_*$). Note that Ref. [93] writes the factor Υ in physical time as $\Upsilon = 1 - 1/y$ with $y = \sqrt{1 + 2(t - t_s)H_s}$, and then associates the source lifetime in cosmic time $t - t_s$ to the time of onset of non-linearities, estimated to correspond to the shock formation time, $\tau_{\text{fin}} \sim \tau_{\text{sh}} \equiv R_*/\sqrt{K}$ (see also Refs. [98–100]). However, the conformal invariance of the fluid equations when the fluid is radiation-dominated only holds

if they are expressed in comoving lengths and conformal times [42, 89, 90]. Therefore, any characteristic scale or time inferred from the fluid dynamics in flat space-time, like τ_{sh} , can be used in the expanding Universe *only in terms of conformal time*. Consequently, it is the interval in conformal time instead of the interval in cosmic time that should be associated to the shock time when evaluating the expected time for non-linearities to develop. In summary, when extending the stationary UETC case, and therefore the sound-shell model, to an expanding Universe, one should set the duration of the GW sourcing to $\delta\eta_{\text{fin}} \sim \delta\eta_{\text{sh}} \equiv \mathcal{R}_*/\sqrt{K}$ in Eq. (2.30), so that $\Upsilon \sim \mathcal{H}_*\mathcal{R}_*/(\sqrt{K} + \mathcal{H}_*\mathcal{R}_*)$. Concerning the spectral shape $S_{\text{exp}}(k_c\mathcal{R}_*)$, the Universe expansion can influence the spectrum when the GW production is comparable or larger than the Hubble time, and the simulation results need to be complemented by analytical studies (cf. Ref. [59]), or simulations accounting for the Universe expansion need to be run (cf. Ref. [55]). In this work, we only discuss the spectral shape arising in the context of our simulations (see Sec. 4.4), and we defer a complete evaluation of the Universe expansion effect on the spectral shape to a future study.

In the locally stationary UETC case, extending Eq. (2.21) to apply in an expanding Universe [59], an effective integrated K^2 that can be used in Eq. (2.24) to estimate the effect of expansion is the following

$$K_{\text{int,exp}}^2 \equiv \int_1^{\tilde{\eta}_{\text{fin}}} \frac{d\tilde{\eta}}{\tilde{\eta}^2} K^2(\tilde{\eta}), \quad (2.31)$$

where normalized conformal times refer to $\tilde{\eta} = \eta/\eta_* = \eta\mathcal{H}_*$. Note that this is different than the normalization used when ignoring the expansion of the Universe for cosmic times, $\tilde{t} = t\beta$. When K^2 is constant in time, this reduces to

$$K_{\text{int,exp}}^2 = K^2 \int_1^{\tilde{\eta}_{\text{fin}}} \frac{d\tilde{\eta}}{\tilde{\eta}^2} = K^2 \Upsilon(\delta\tilde{\eta}_{\text{fin}}), \quad \text{for } K \text{ constant}. \quad (2.32)$$

Then, the resulting GW spectrum can be expressed as

$$\Omega_{\text{GW,exp}}(k) = 3 \mathcal{T}_{\text{GW}} \tilde{\Omega}_{\text{GW}} K_{\text{int,exp}}^2 \mathcal{H}_*\mathcal{R}_* S_{\text{exp}}(k_c\mathcal{R}_*). \quad (2.33)$$

Taking into account that the power-law decay in flat space-time should be taken in conformal time $K(\tilde{\eta}) = K_0 (\Delta\tilde{\eta}/\Delta\tilde{\eta}_0)^{-b}$ due to the conformal invariance of the dynamics for a radiation-dominated fluid, then we need to express the absolute times in a flat space-time as time intervals in conformal time, $\Delta\tilde{\eta} = \delta\tilde{\eta} + \Delta\tilde{\eta}_*$, where $\delta\tilde{\eta} = \tilde{\eta} - 1$ and $\Delta\tilde{\eta}_* = \Delta\tilde{\eta}_0 - \delta\tilde{\eta}_0$. The resulting integral for $2b \neq 1$ can be expressed as

$$K_{\text{int,exp}}^2 = K_0^2 \Delta\tilde{\eta}_0^{2b} \int_1^{\tilde{\eta}_{\text{fin}}} \frac{d\tilde{\eta}}{\tilde{\eta}^2} (\tilde{\eta} + \Delta\tilde{\eta}_* - 1)^{-2b} = K_0^2 \Upsilon_b(\delta\tilde{\eta}_{\text{fin}}), \quad (2.34)$$

where we have defined a suppression factor

$$\Upsilon_b(\delta\tilde{\eta}_{\text{fin}}) = \frac{\mathcal{F}_b(\delta\tilde{\eta}_{\text{fin}}) - \mathcal{F}_b(0)}{1 - 2b}, \quad (2.35)$$

with

$$\mathcal{F}_b(\delta\tilde{\eta}) = \left(\frac{\Delta\tilde{\eta}_* + \delta\tilde{\eta}}{\Delta\tilde{\eta}_0} \right)^{1-2b} \frac{\Delta\tilde{\eta}_0}{(\Delta\tilde{\eta}_* - 1)^2} {}_2F_1 \left[2, 1 - 2b, 2 - 2b, \frac{\Delta\tilde{\eta}_* + \delta\tilde{\eta}}{\Delta\tilde{\eta}_* - 1} \right], \quad (2.36)$$

being ${}_2F_1$ the hypergeometric function. The function Υ_b reduces to the one found for stationary sources when $b = 0$, i.e., $\Upsilon_0(\delta\tilde{\eta}_{\text{fin}}) \equiv \Upsilon(\delta\tilde{\eta}_{\text{fin}}) = \delta\tilde{\eta}_{\text{fin}}/(1 + \delta\tilde{\eta}_{\text{fin}})$ [59, 93]. We highlight that the emergence of a hypergeometric function has no deep physical meaning, since Eq. (2.36) arises from introducing the chosen fit $K(\tilde{\eta})$ in Eq. (2.31). The relevant physical quantity is the modification Υ_b with respect to Υ (i.e., with no decay of the source) obtained from the additional decaying function in the integral in Eq. (2.34). The value of $\Delta\tilde{\eta}_0 \equiv \Delta\tilde{\eta}_0/\mathcal{H}_*$ corresponds to the characteristic time interval $\Delta t_0 \equiv \Delta\tilde{t}_0/\beta$ used in the fit of K^2 in flat space-time, introducing the implicit dependence of the resulting GW spectrum on the ratio β/H_* through $\Delta\tilde{\eta}_0 = \Delta\tilde{t}_0 H_*/\beta$. We note that, in principle, using $\Delta\tilde{\eta}_* = \tilde{\eta}_* - \tilde{\eta}_0 + \Delta\tilde{\eta}_0$ in the integrand of Eq. (2.34) allows to compute the GW spectrum starting at any conformal time $\tilde{\eta}_* > \tilde{\eta}_0$. We also find that for any value of b , the functions $\Upsilon_b(\delta\tilde{\eta}_{\text{fin}})$ always reduce to the linear dependence with the source duration $\delta\tilde{\eta}_{\text{fin}}$ for short duration, $\delta\tilde{\eta}_{\text{fin}} \ll 1$. Then, the final GW spectrum becomes

$$\Omega_{\text{GW,exp}}(k) = 3 \mathcal{T}_{\text{GW}} \tilde{\Omega}_{\text{GW}} K_0^2 \Upsilon_b(\delta\tilde{\eta}_{\text{fin}}) \mathcal{H}_* \mathcal{R}_* S_{\text{exp}}(k_c \mathcal{R}_*), \quad (2.37)$$

where Υ_b is obtained from the integrated K_{int}^2 and in particular it is given by Eqs. (2.35) and (2.36) when the fit $K^2 = K_0^2 (\Delta\tilde{\eta}/\Delta\tilde{\eta}_0)^{-2b}$ holds at all times of the GW production. We emphasize that the suppression factor Υ_b works as a proxy to estimate the effect of the Hubble expansion, which has not been accounted for in our simulations performed in flat space-time.

As mentioned above, in Sec. 4.2 we use the numerical results of the simulations to find the values of the fit parameters b and K_0 for different PTs. Then, we validate the assumption that Eq. (2.23) applies within the duration of our simulations in Sec. 4.3, and provide an estimate of the GW amplitude as a function of the source duration $\delta\tilde{\eta}_{\text{fin}}$, for an expanding Universe using Eq. (2.37). We will further assume that the GW production starts when all the simulation domain is in the broken phase, i.e., $\tilde{\eta}_* = \tilde{\eta}_0$.

3 Numerical setup

In this section, we focus on describing the numerical setup of the Higgsless simulations: in Sec. 3.1, we comment on the updates in the numerical scheme with respect to Ref. [58], and in Sec. 3.2, we describe the simulation suite considered for this work.

3.1 Updates to the numerical setup

In this section, we highlight three updates to the Higgsless simulations with respect to Ref. [58] aimed at improving: (1) the time integration scheme, (2) the mapping between the discrete and the continuum momenta, and (3) the criterion for numerical stability in simulations of strong first-order PTs ($\alpha = 0.5$). For a complete description of the

Kurganov-Tadmor (KT) numerical scheme [101] used for the Higgsless simulations, we refer to Refs. [56, 58].

Commencing with (1), in practice, the integral in Eq. (2.12) must be computed numerically on the grid of space and time. For the space grid, this is accomplished through a fast Fourier transform routine [102]. For the time grid, in order to overcome the practical limitation of memory (i.e., storing a large number of 3D time slices), one needs to resort to another method. In the first iteration of the Higgsless simulation code, the discrete integral in time of Eq. (2.12) was approximated as

$$\tilde{T}_{ij}(\tilde{t}_{\text{init}}, \tilde{t}, \tilde{q}, \tilde{\mathbf{k}}) = \sum_{m=1}^{N_t} \delta\tilde{t}_m e^{i\tilde{q}\tilde{t}_m} \tilde{T}_{ij}(\tilde{t}_m, \tilde{\mathbf{k}}), \quad (3.1)$$

where the time coordinate is discretized in N_t intervals $[\tilde{t}_m - \tilde{t}_{m-1}]$ of size $\delta\tilde{t}_m = \tilde{t}_m - \tilde{t}_{m-1}$, i.e., through its Riemann sum, by stacking past time slices weighted by a complex factor from \tilde{t}_{init} until $\tilde{t} \leq \tilde{t}_{\text{end}} = \tilde{t}_{N_t}$ for each time step $\delta\tilde{t}_m$ over which the GWs are sourced. We assume a fixed time step, such that $\delta\tilde{t}_m = \delta\tilde{t}, \forall m$. In the current version, we improve upon this scheme by treating \tilde{T}_{ij} as a piecewise linear function interpolating between the support points, using a similar scheme to the one proposed in Ref. [66] for solving the GW equation. Since the integrand involving an oscillating exponential as well as the linearized \tilde{T}_{ij} is now analytically integrated, this modified routine allows to capture better the behavior at large k , alleviating the time-step $\delta\tilde{t}$ required to find accurate spectra in this regime (see discussion in Ref. [66]). However, no sizable discrepancies have been observed in the UV range of the GW spectra through this change for the dynamical range and choice of $\delta\tilde{t}$ used in our simulations.

Continuing with (2), we begin by noting that the first version of the Higgsless simulations employed a sin-prescription for the mapping of discrete momenta on the grid to their correspondents in the continuum. Care must be taken that on the grid of the simulation with N points per dimension, Fourier modes with momenta $-l_i$ and $N - l_i$ (in the i th direction) are equivalent and mapped to the same momenta in the continuum. At the same time, momenta of order $l_i \simeq N$ are equivalent to $l_i \simeq 0$ and should be considered soft. Depending on whether the observable under consideration is sensitive to the sign of the momentum, this motivated the mapping

$$\tilde{k}_i = \frac{2-a}{\delta\tilde{x}} \sin\left(\frac{a\pi l_i}{N}\right), \quad (3.2)$$

where $\delta\tilde{x} = \tilde{L}/N$, with $a = 1$ when the sign is relevant and $a = 0$ when it is not. In the current simulations, we generally use a *saw* description for the momenta

$$\tilde{k}_i = \begin{cases} 2\pi l_i / (N\delta\tilde{x}), & l_i < N/2, \\ 0, & N/2, \\ 2\pi(l_i - N) / (N\delta\tilde{x}), & l_i > N/2. \end{cases} \quad (3.3)$$

As such, the saw-prescription avoids different descriptions in different contexts (such as the space Fourier transforms for the GW estimate or for the numerical fluid evolution) and

maintains a good map of momenta all the way to $l_i \simeq N/2$, while the previous method is only accurate in the linear regime of the sine function. At the moment, we do not find substantial differences between the two implementations, but we expect the new implementation to improve the results when increasing the resolution of the Higgsless simulations.

The third point (3) concerns the choice of the maximal local velocity $a_{j+1/2}$ (on a staggered cell in direction j), appearing in Eq. (3.7) of Ref. [58]. In summary, this quantity enters the flux limiter used in the KT scheme to preserve the shock structures in the lattice by setting a minimal numerical viscosity that reduces spurious oscillations and improves the stability of the numerical scheme. In the limit of small fluid velocities, i.e., for weak and intermediate PTs, $a_{j+1/2} = c_s = 1/\sqrt{3}$ is a good choice. In the case of strong PTs, however, fluid velocities often supersede $1/\sqrt{3}$ and approach 1. To improve the numerical stability of the simulation, we therefore choose $a_{j+1/2} = 1$ for strong PTs. In the weak regime, the numerical changes due to this choice are negligible but for stronger PTs, it improves the stability of the code significantly. In rare occasions and close to shocks, the simulation can lead to unphysical fluid velocities (essentially $v > 1$) as a numerical artifact. In these cases, we opted to enforce the local fluid velocity to 1. This only happened in isolated points and had no measurable impact on the conservation of $T^{0\mu}$ or the GW spectra.

In all other regards, the current version of the Higgsless implementation is identical to the first version in Ref. [58].

3.2 Simulations and parameter choices

We list the parameters considered in this study in Tab. 1. We expand upon Ref. [58] by including in our parameter scan strong PTs with $\alpha = 0.5$. We thus run simulations for $\alpha \in \{0.0046, 0.05, 0.5\}$ and wall velocities $v_w \in \{0.32, 0.36, \dots, 0.76, 0.8\}$, where the dots

| | reference | seeds | single-bubble |
|---|-------------------------|-----------------------------------|--------------------------------|
| PT strength α | $\{0.0046, 0.05, 0.5\}$ | $\{0.0046, 0.05, 0.5\}$ | $\{0.0046, 0.05, 0.5\}$ |
| wall velocity v_w | $\in [0.32, 0.8]$ | $\{0.32/0.36, 0.6, 0.8\}$ | $\in [0.32, 0.8]$ |
| box size $\tilde{L}/v_w \equiv L\beta/v_w$ | $\{20, 40\}$ | $\{20, 40\}$ | $\{20, 40\}$ |
| sim. time $\tilde{t}_{\text{end}} \equiv t_{\text{end}}\beta$ | 32 | 32 | $\tilde{L}/[2 \max(v_w, c_s)]$ |
| grid size N | $\{64, 128, 256, 512\}$ | $\{64, 128, 256, 512\}$ | 512 |
| $\delta\tilde{t}/\delta\tilde{x}$ | $< 1/4$ | $< 1/4$ | $< 1/4$ |
| count. | 304 | $72 \times 9 \text{ seeds} = 648$ | 76 |

Table 1. Summary of simulation runs with physical and numerical parameter choices. *Reference* indicates the simulations constructed from a single reference bubble nucleation history (for each box size \tilde{L}/v_w), thereby eliminating statistical differences among the sample of reference simulations. *Seeds* refers to simulations constructed from a set of 9 additional bubble nucleation histories, allowing to infer statistical sample variance for 3 selected wall velocities $v_w = 0.32$ (0.36 for strong PTs), 0.6, and 0.8, which correspond to a deflagration, a hybrid, and a detonation for weak and intermediate PTs, while $v_w = 0.8$ is still a hybrid for strong PTs. *Single-bubble* refers to simulations with only one single centrally nucleated bubble, allowing us to study the convergence of self-similar profiles. We take a range of $v_w \in [0.32, 0.8]$ in increments of 0.04 besides for strong transitions ($\alpha = 0.5$) for which we take $v_w \in [0.36, 0.8]$. A total of 1028 simulations have been performed.

mean increases by 0.04, except for strong PTs where $v_w = 0.32$ is excluded due to the non-existence of deflagrations for $\alpha \gtrsim \frac{1}{3}(1 - v_w)^{-13/10}$ [49], implying a total of $3 \times 13 - 1 = 38$ PT parameter points. To extract our main results, we run *reference* simulations for each simulation box size, in which a single reference bubble nucleation history is used for all wall velocities, PT strengths, and grid sizes, thus eliminating the effect of sample variance when comparing the results for different parameter sets.

The bubble nucleation histories result in a number of bubbles of the order of $N_b \simeq \tilde{L}^3/(8\pi v_w^3)$, where $\tilde{L} \equiv L\beta$ is the simulation box size, nucleated following a statistical distribution that is exponential in time and uniform in space, as described in Sec. 2.1, and then removing bubbles that nucleate inside the future causal cone of previous bubbles to take into account the evolution of the broken-phase volume with time (see Ref. [58] for details). In our simulations, \tilde{L}/v_w takes on values of 20 and 40, yielding of the order of 300 and 2500 bubbles respectively. Using the same numerical resolution, simulations with $\tilde{L}/v_w = 40$ yield a reduction in the statistical variance by increasing the number of bubbles and by offering an increased resolution of the measured quantities in the IR regime, while simulations with $\tilde{L}/v_w = 20$ cover a larger dynamical range in the UV regime. For comparison, the number of bubbles for $\tilde{L}/v_w = 40$ ($N_b \simeq 2500$) in our work and previous Higgsless simulations [58] is in general larger than most⁵ of the previous numerical simulations of the fluid-scalar system [50, 52, 78], especially for intermediate PTs, allowing for a reduction of the statistical variance. A potential issue of small box sizes is that for small wall velocities, the shock in front of the wall of the first nucleated bubble might collide with its mirror images (due to the use of periodic boundary conditions) before the end of the PT. To avoid this issue, we take the minimum value of v_w to be 0.32 in our simulations, such that the numerical domain is filled with the broken phase before the largest bubble reaches the edges of the simulation box even for the smaller box $\tilde{L}/v_w = 20$.

For each of the 76 parameter points $\{v_w, \alpha, \tilde{L}/v_w\}$, we then run simulations with different number of grid points N^3 with $N \in \{64, 128, 256, 512\}$, yielding a total of $76 \times 4 = 304$ *reference* simulations. Running simulations of different grid sizes allows us to test the degree of convergence of our numerical results and to estimate physical quantities in the continuum limit by extrapolation (see Sec. 4.1). To ensure the stability of our simulations, we choose the number of time steps $N_t = \tilde{t}_{\text{end}}/\delta\tilde{t}$ to satisfy the Courant-Friedrichs-Lewy (CFL) condition $\delta\tilde{t}/\delta\tilde{x} < 1/4$ with $\delta\tilde{x} = \tilde{L}/N$. We have confirmed that even for strong transitions, increasing N_t beyond this threshold does not significantly change the numerical results. For each parameter point $\{v_w, \alpha, \tilde{L}/v_w\}$, we have also run *single-bubble* simulations to track the convergence of the self-similar fluid profiles, leading to 76 simulations. These results are presented in App. B and will be used to improve the extrapolated predictions of the *reference* multiple-bubble simulations in Sec. 4.1. We note that *single-bubble* simulations are only run until $\tilde{t}_{\text{end}} = \tilde{L}/[2\max(c_s, v_w)]$, being roughly the time when the fluid shell reaches the edge of the simulation domain.

⁵We note that Ref. [50] uses $N_b = 32558$ for a weak PT with $v_w = 0.44$, while it takes either $N_b = 988$, 125, or 37 for the rest of the PT parameter space. In Ref. [52], 5376 bubbles are used for some weak PTs, while 11 and 84 are used for other weak PTs, and for intermediate ones. Reference [78] considers 8 bubbles for all simulations.

In addition to the *reference* simulations, we also run multiple-bubble simulations based on 9 additional distinct bubble nucleation histories for all strengths, resolutions, and box sizes, for $v_w \in \{0.32/0.36, 0.6, 0.8\}$, where the lower $v_w = 0.32$ is used for weak and intermediate transitions, and $v_w = 0.36$ for strong ones. These velocities correspond to deflagrations, hybrids, and detonations, respectively, except for strong transitions for which also $v_w = 0.8$ corresponds to a hybrid. This implies a total of $3 \times 3 \times 2 \times 4 \times 9 = 648$ *seed* simulations from which the statistical variance of the results can be estimated. We will use these simulations to provide error bars in our measured quantities, corresponding to the standard deviation from the 10 different bubble nucleation histories in Sec. 4.

All *reference* and *seed* simulations are run between $0 < \tilde{t} \equiv t\beta < 32$ and the GW spectrum is extracted from the time interval spanning from $\tilde{t}_{\text{init}} = 16$ to $\tilde{t}_{\text{end}} = 32$. We set the origin of time coordinates, $\tilde{t}_{\text{ref}} = 0$, at a reference value such that the first bubble nucleates at $\tilde{t}_n = 0.5$, based on the invariance of our equations to time translations when the expansion of the Universe can be ignored. Then, the results of the simulations in flat space-time accurately model the PTs in an expanding Universe when $\beta/H_* \gg \tilde{t}_{\text{end}} = 32$. We specifically cut out the early times up to $\tilde{t}_{\text{init}} = 16$ to extract the contribution from the fluid perturbations after the collisions of bubbles, and to reduce the realization-dependent effects on the GW production. Consequently, we also neglect the contribution to the GW spectrum of the initial collisions (see also the discussion in Ref. [56]). In this regime, we then compute $\mathcal{I}_{\text{sim}}(\tilde{t}_{\text{init}}, \tilde{t}_{\text{fin}}, \tilde{k})$ that allows us to robustly test the scaling of Eq. (2.23) and compute the GW efficiency $\tilde{\Omega}_{\text{GW}}$ and the spectral shape $S(kR_*)$. The time $\tilde{t}_{\text{init}} = 16$ is shortly after the time when the broken phase fills up the whole volume of the simulation, $\tilde{t}_0 \simeq 10$, for the reference nucleation history with $\tilde{L}/v_w = 20$. We will consider times $\tilde{t} > \tilde{t}_0$ to fit the time evolution of the kinetic energy fraction $K(\tilde{t}) = K_0 (\tilde{t}/\tilde{t}_0)^{-b}$ in Sec. 4.2.

In total, we have performed 1028 simulations, which we summarize in Tab. 1, with an estimated time of $\sim 10^6$ CPU hours. We note that each large-resolution simulation ($N = 512$) takes $\sim 10^3$ CPU hours, a quite modest value that indicates the numerical efficiency of the Higgsless approach.

4 Numerical results

Before we present a detailed account of our numerical results, we would like to put them in perspective. Overall, our results can be summarized as follows:

- *Simulations of strong first-order PTs with $\alpha = 0.5$:* We present results of simulations of strong first-order PTs, covering a wide range of wall velocities and performing systematic checks of the numerical convergence of our results. For the first time, we obtain GW spectra from fluid motion for strong PTs.⁶ Simulations of strong PTs are more challenging when it comes to numerical stability and proper resolution of non-linearities. At the same time, stronger PTs lead to a larger GW signal and therefore are preferred for potential detection, hence the importance of developing

⁶Reference [78] also provides estimates of the kinetic energy and the integrated GW spectra for $\alpha = 0.5$, but does not present results about the spectral shape.

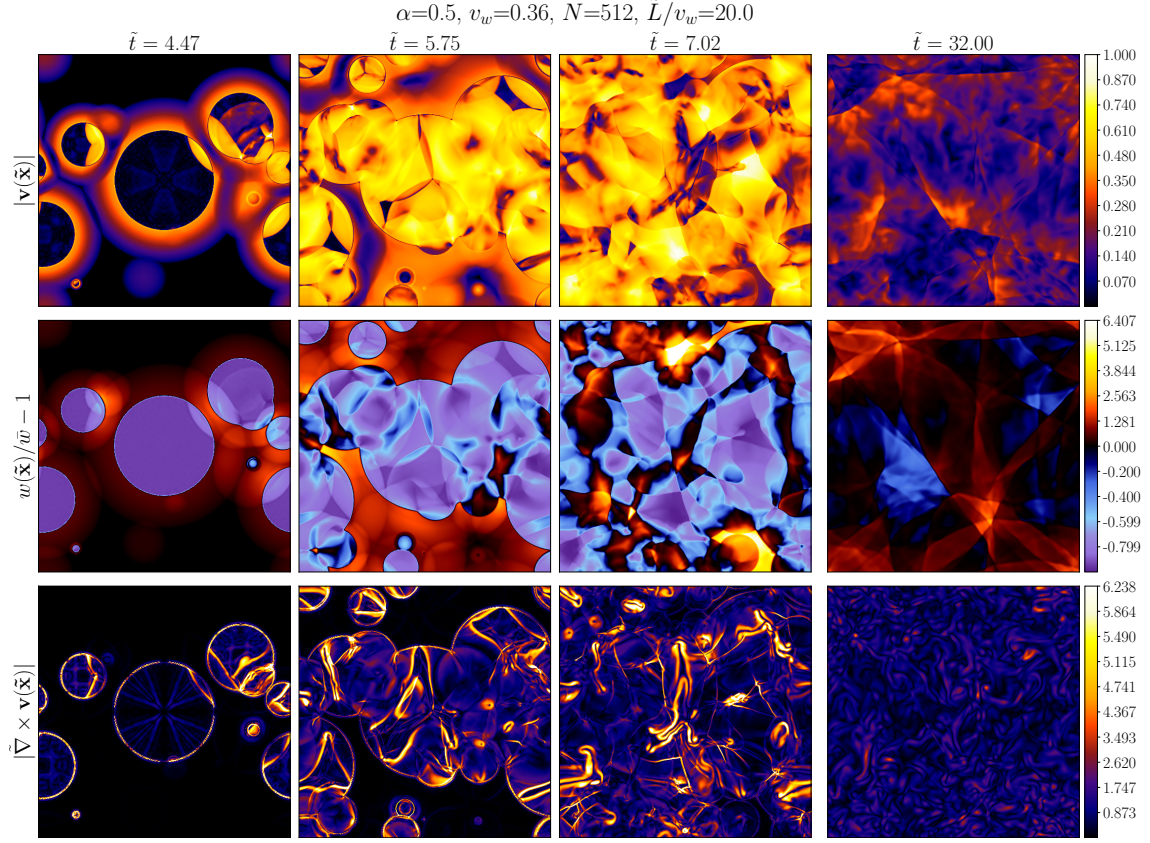


Figure 1. Velocity (upper panel), enthalpy fluctuations (middle panel), and vorticity (lower panel) in an xy -plane slice of the simulation volume at $z = 0$ and at different times \tilde{t} , for a strong PT with $\alpha = 0.5$ and wall velocity $v_w = 0.36$, which corresponds to a deflagration (see Fig. 13).

an accurate understanding of the resulting GW spectrum. We provide in Sec. 5 a template, based on the expected GW spectrum from compressional fluid perturbations (obtained within the assumption that the UETC of the source is stationary in time), but extended to intermediate and strong PTs, for which the kinetic energy decays (see Secs. 2.4 and 2.5). The resulting integrated GW amplitude is studied numerically in Sec. 4.3 and the model of Sec. 2.5 is validated against the numerical results. This allows us to incorporate information from our simulations to be used for phenomenological studies. We show in Fig. 1 a simulation example of a strong PT that corresponds to a deflagration with $v_w = 0.36$.

- *Development of non-linearities:* For strong PTs, and some intermediate PTs with confined hybrids, the simulations show several phenomena that probably stem from non-linear dynamics of the fluid. First and foremost, we observe a decay in the kinetic energy density of the fluid at late times (after the PT ends), which could be compatible with the formation of non-linearities leading to a cascading of energy from larger to smaller scales in the fluid perturbations, making the viscous dissipation at small scales more effective. Potentially due to this decay, we find that the amplitude

of the GW spectrum deviates from the linear dependence with the source duration predicted by the sound-shell model for weak PTs, under the assumption of source stationarity. For intermediate and strong PTs we observe that, as the simulation proceeds, the amplitude of the GW spectrum grows slower than linearly with the source duration. While we do not run the simulations sufficiently long to observe the ultimate saturation of the GW spectrum resulting from this behavior, we do indeed expect that the GW spectrum amplitude eventually saturates as the kinetic energy dampens and vorticity dominates the fluid motion [55, 70, 71]. The cascading of kinetic energy from large to small scales would also impact the UV part of the GW spectrum, from the k^{-3} found for sound waves [40, 50–52, 56, 58–60] towards a shallower spectrum, for example the $k^{-8/3}$ inferred from the assumption of Kolmogorov spectrum in vortical turbulence [53, 55, 62, 63, 65, 71, 103]. We indeed observe a shallower spectrum in the UV regime in simulations of intermediate and strong PTs. While these phenomena are all consistent with what would be expected from the development of non-linearities in the bulk fluid motion, a solid physical interpretation of the simulations would still require more evidence and more checking, as numerical resolution can become an issue in simulating intermediate and strong PTs. We test the numerical robustness of our results in the following of this section, and comment on future studies that would be required to confirm some of our findings. In particular, we present in App. C a preliminary study of the development of vorticity in our simulations, and also show the vorticity found in one of our simulations in the lower panel of Fig. 1.

- *Template parameterizations:* We express all our numerical findings in terms of a few physical quantities, to facilitate their use in phenomenological studies (numerical fits are sometimes still necessary, e.g., for the time-decay parameters). All quantities evaluated in the simulations are dimensionless, such that β/H_* does not enter in the numerical results, and only appears when we recover the physical quantities, as indicated in Eq. (2.8). This motivated the authors in Refs. [56, 58] to use the variable Q' [see Eq. (2.18)] to interpret the numerical results. In the present work, we instead characterize them with R_* and K_{int}^2 [see Eq. (2.23)]. This allows to capture the essential results of GW generation by fluid motion in a form as simple as possible, because R_* and K_{int}^2 are quantities determining the fluid dynamics, as opposed to quantities related to the PT such as β . Indeed, normalizing to R_* and K_{int}^2 , the GW efficiency $\tilde{\Omega}_{\text{GW}}$ becomes almost invariant over both v_w and duration of the source. Furthermore, we introduce K_{int}^2 to allow for deviations with respect to the linear dependence of the GW amplitude with the source duration, which is expected for stationary sources, but is no longer valid for decaying ones (see discussion in Secs. 2.4 and 2.5). We also provide in Sec. 2.6 a definition of $K_{\text{int,exp}}^2$ that allows to incorporate *a posteriori* the effect of the expansion of the Universe [see Eqs. (2.33) and (2.34)], taking into account the conformal invariance of radiation-dominated fluid dynamics [42, 90].

To test the validity of our numerical results, we pay special attention to the following

points, addressed throughout this section. In Sec. 4.1, we study the convergence of our results with respect to the grid spacing, $\delta\tilde{x}$. In Sec. 4.2, we study the time dependence of the fluid kinetic energy fraction K , and fit the decaying power law presented in Sec. 2.5 to the numerical results. In Sec. 4.3, we test the scaling of the GW spectrum with K_{int}^2 and R_* presented in Secs. 2.4 and 2.5, we analyze the evolution of the integrated GW amplitude with the source duration, and compute the GW efficiency $\tilde{\Omega}_{\text{GW}}$, according to Eq. (2.23). We also provide in Sec. 4.3 an estimate of the expected GW amplitude in a flat Minkowski space-time, based on the numerical results of Secs. 4.1–4.3, and in an expanding background, using the model presented in Sec. 2.6. Finally, in Sec. 4.4, we study the spectral shape of the GW spectrum obtained in the simulations. We pay special attention to the UV regime, where we find deviations with respect to the slope expected in the case of GW production by sound waves, i.e., k^{-3} . These deviations are compatible with the shallower decay with k that one would expect in the presence of a forward energy cascade due to non-linearities. However, while we observe both a decay of the kinetic energy and the distortions of the GW spectra, to be able to confirm the presence of a forward cascade in our simulations, a detailed study of the dependence of the kinetic spectra on the numerical parameters would be required. This is beyond the scope of the present analysis and we defer it to future work. Furthermore, the time evolution can also affect the spectral shape. Indeed, it is not in general expected that all wave numbers evolve with the source duration in the same way, as shown in Ref. [59]. Therefore, the assumption that all wave numbers follow the same evolution as the integrated amplitude, which is studied in Sec. 4.3, from the ending time of the simulations to the final time of GW sourcing can affect the resulting spectral shape, especially in the IR, where the assumption of infinitesimal compact support described in Sec. 2.5 might not necessarily be satisfied. The Universe expansion could also affect the resulting spectral shape, which is only computed in flat space-time, for long source durations, as we discuss in Sec. 2.6.

4.1 Convergence analysis of the kinetic energy and GW amplitude

In the present study, for each parameter point $\{\alpha, v_w\}$, we have run simulations at four resolutions $N \in \{64, 128, 256, 512\}$ and two box sizes $\tilde{L}/v_w \in \{20, 40\}$. The Higgsless simulations use relatively sparse grids compared to simulations with scalar fields [40, 50, 52, 78]. Therefore, the resolution is not always high enough to reproduce some of the self-similar fluid profiles surrounding the uncollided bubbles at the initial stages of the simulations. This occurs especially for parameter points with $v_w \lesssim v_{\text{CJ}}$, where v_{CJ} is the Chapman-Jouguet speed, determining the transition between hybrids and detonations. Indeed, the fluid profiles become very thin as v_w approaches v_{CJ} , and require a large number of lattice points to be properly resolved. Since the Chapman-Jouguet speed is $v_{\text{CJ}} = \{0.63, 0.73, 0.89\}$ respectively for $\alpha = \{0.0046, 0.05, 0.5\}$, for our choice of parameters (cf. Tab. 1), very thin profiles develop when (i) $v_w = 0.6$ and the PT is weak, (ii) $v_w = 0.72$ and the PT has intermediate strength, and (iii) $v_w = 0.8$ and the PT is strong. For reference, we show in App. B (see Figs. 13 and 15) the self-similar profiles of the fluid perturbations by uncollided expanding bubbles [49], computed by direct integration of the fluid equation across the wall using COSMOGW [84]. The development of the thin hybrid solutions appears clearly.

The fluid profile is described in terms of the variable $\xi \equiv r/(t - t_n)$, with r being the radial distance to the nucleation location and t_n the time of nucleation. Therefore, the resolution in ξ for a fixed N is initially low and then improves as time evolves. Despite, for the aforementioned cases with v_w close to v_{CJ} , this increase in resolution is not enough to fully resolve the self-similar profiles at the time of bubble collision, which is the relevant one for us. Indeed, we are interested in the GW production by fluid motion after bubble collision, and not resolving the single bubble fluid profile at the collision time affects the total kinetic energy available for the GW production. We study the rate of convergence of the kinetic energy in App. B, comparing multiple-bubble *reference* with *single-bubble* simulations. We confirm that the under-resolution of the fluid shell profiles for some set of parameters leads to an underestimation of the total kinetic energy available for the GW production, and we propose a method to partially correct for this under-estimation, also discussed at the end of this section.

In addition to the required resolution for thin self-similar profiles before collisions, as the fluid perturbations become non-linear, we expect large numerical resolution to be required also to fully capture the dynamics during and after collisions. In the following, we first analyze the convergence of the numerical results for multiple-bubble *reference* runs, to provide estimates of the time-integrated squared kinetic energy $K_{\text{int}}^2(\tilde{t}_{\text{init}}, \tilde{t}_{\text{end}})$, defined in Eq. (2.22), and of the integrated GW amplitude $\mathcal{I}_{\text{sim}}^{\text{int}} \equiv \int \mathcal{I}_{\text{sim}} d \ln k$, where $\mathcal{I}_{\text{sim}}(\tilde{t}_{\text{init}}, \tilde{t}_{\text{end}}, \tilde{k})$ is defined in Eq. (2.10), for initial and final times $\tilde{t}_{\text{init}} = 16$ and $\tilde{t}_{\text{end}} = 32$, corresponding to the time interval over which the GW spectrum is computed in the simulations. These quantities will be used in Secs. 4.3 and 4.4 to estimate the GW efficiency $\tilde{\Omega}_{\text{GW}}$ and the spectral shape $S(kR_*)$. We also provide estimates for the kinetic energy fraction K_0 evaluated at the time when the PT completes, $\tilde{t}_0 \simeq 10$. We will then attempt to improve this estimate by including the results of *single-bubble* runs studied in App. B, tracking the degree of convergence of each bubble at the time when they collide, and leading to a new estimate, \mathcal{K}_0 , defined in Eq. (B.4) (see App. B for details). Note that we will use the improved estimates \mathcal{K}_0 in the GW templates presented in Sec. 5.

In order to take the effect of numerical resolution into account, we study the numerical results as a function of the number of grid points N and attempt to improve our estimates by extrapolating our results to $N \rightarrow \infty$, based on the underlying assumption that the extrapolation method obtained for the computed values of N also applies for $N > 512$. On general grounds, it is possible to define a particular number of grid points N_* such that, for $N \gg N_*$, a simulation has reached a converged solution, meaning that the numerical results are unaffected, within some acceptable tolerance, by changing N : hence, we can assume that they accurately represent the continuum results. Empirically, we find that, for insufficient resolution, the kinetic energy fraction K is in general *underestimated* when the grid resolution is insufficient (see also App. B), as the velocity profiles around the peak are under-resolved. This motivates us to use the following function when extrapolating the numerical values of the kinetic energy fraction:

$$K = \frac{K_\infty}{1 + (N_*/N)^a}, \quad (4.1)$$

where a , N_* , and K_∞ are found by fitting the numerical results as a function of N . We also define the relative error in the kinetic energy, ε_K :

$$\varepsilon_K \equiv \frac{K_\infty - K}{K_\infty} = \left(\frac{\delta\tilde{x}}{\delta\tilde{x}_*} \right)^a + \mathcal{O} \left(\left(\frac{\delta\tilde{x}}{\delta\tilde{x}_*} \right)^{2a} \right), \quad (4.2)$$

where the last equality comes from expanding in $\delta\tilde{x}/\delta\tilde{x}_* \ll 1$ with $\delta\tilde{x}_* = \tilde{L}/N_*$, which holds when $N \gg N_*$. The last equality shows that the value of a in Eq. (4.1) indicates the degree of convergence of the numerical results.

The result of applying the convergence analysis based on Eq. (4.1) to the *reference* runs with multiple bubbles is shown in Fig. 2 (for the full evolution of the kinetic energy, see Sec. 4.2 and Fig. 4). In the top row of panels in Fig. 2, we show the rms kinetic energy fraction, computed from $K_{\text{int}}^2(\tilde{t}_{\text{init}}, \tilde{t}_{\text{end}})$ [see Eq. (2.22)]:

$$K_{\text{rms}}^2 \equiv \frac{1}{\tilde{T}_{\text{GW}}} \int_{\tilde{t}_{\text{init}}}^{\tilde{t}_{\text{end}}} K^2(\tilde{t}) d\tilde{t} = \frac{K_{\text{int}}^2(\tilde{t}_{\text{init}}, \tilde{t}_{\text{end}})}{\tilde{T}_{\text{GW}}}, \quad (4.3)$$

where $\tilde{T}_{\text{GW}} \equiv \tilde{t}_{\text{end}} - \tilde{t}_{\text{init}} = 16$. According to the model proposed in Sec. 2.5, $K_{\text{int}}^2 \equiv K_{\text{rms}}^2 \tilde{T}_{\text{GW}}$ is the relevant quantity entering in the GW amplitude $\mathcal{I}_{\text{sim}}^{\text{int}}$. The rms kinetic energy fraction is shown normalized by the single-bubble value K_ξ (see Tab. 3 for numerical values).

We focus on the simulations with $\tilde{L}/v_w = 20$, as these cover smaller scales than those with $\tilde{L}/v_w = 40$ for a fixed N , providing a better resolution of the kinetic energy density in the UV regime. The dots in Fig. 2 correspond to the four resolutions $N \in \{64, 128, 256, 512\}$, given in terms of $\delta\tilde{x}/v_w = 20/N$, while the continuous lines show the fit in Eq. (4.1). In Tab. 2, we provide the resulting values of the fit parameters of Eq. (4.1): K_∞^{rms} normalized by the single-bubble kinetic energy fraction K_ξ [see Eq. (2.19)], the degree of convergence a_K , and the relative errors ε_K as defined in Eq. (4.2), for the set of PT parameters shown in Fig. 2. In some simulations, the numerical results have already converged for $N = 512$, as indicated by a small relative error $\varepsilon_K \equiv |K - K_\infty|/K_\infty$ (see values in Tab. 2). Moreover, the fit in Eq. (4.1) represents well most of the simulations, in particular whenever the kinetic energy fraction is underestimated at low resolution, and remains almost constant over the simulation time. However, there are a few cases with $\alpha = 0.5$ and large v_w , in which the trend is different (depicted as dashed lines in Fig. 2). These exceptional cases correspond to strong PTs, in which non-linearities play a relevant role. As we will see in Sec. 4.2, where we study the time evolution of $K(t)$ for different N , in strong PTs, increasing the resolution leads to a *faster* decay of the kinetic energy density with time. Therefore, K_{rms} , which is time integrated, can become smaller when increasing N , inverting the trend with respect to Eq. (4.1). Whenever the fit of Eq. (4.1) is not valid, we take K_∞^{rms} to be the value computed in the simulations for $N = 512$, and the error ε_K is then estimated comparing this value to the one obtained for $N = 256$.

In the middle row of panels in Fig. 2, we show the integrated GW spectrum obtained in the code, $\mathcal{I}_{\text{sim}}^{\text{int}}$, as a function of $\delta\tilde{x}$, while the numerical values of the extrapolated $\mathcal{I}_\infty^{\text{int}}$, the fit parameter $a_{\mathcal{I}}$, and the relative error $\varepsilon_{\mathcal{I}}$ are given in Tab. 2. For the integrated GW

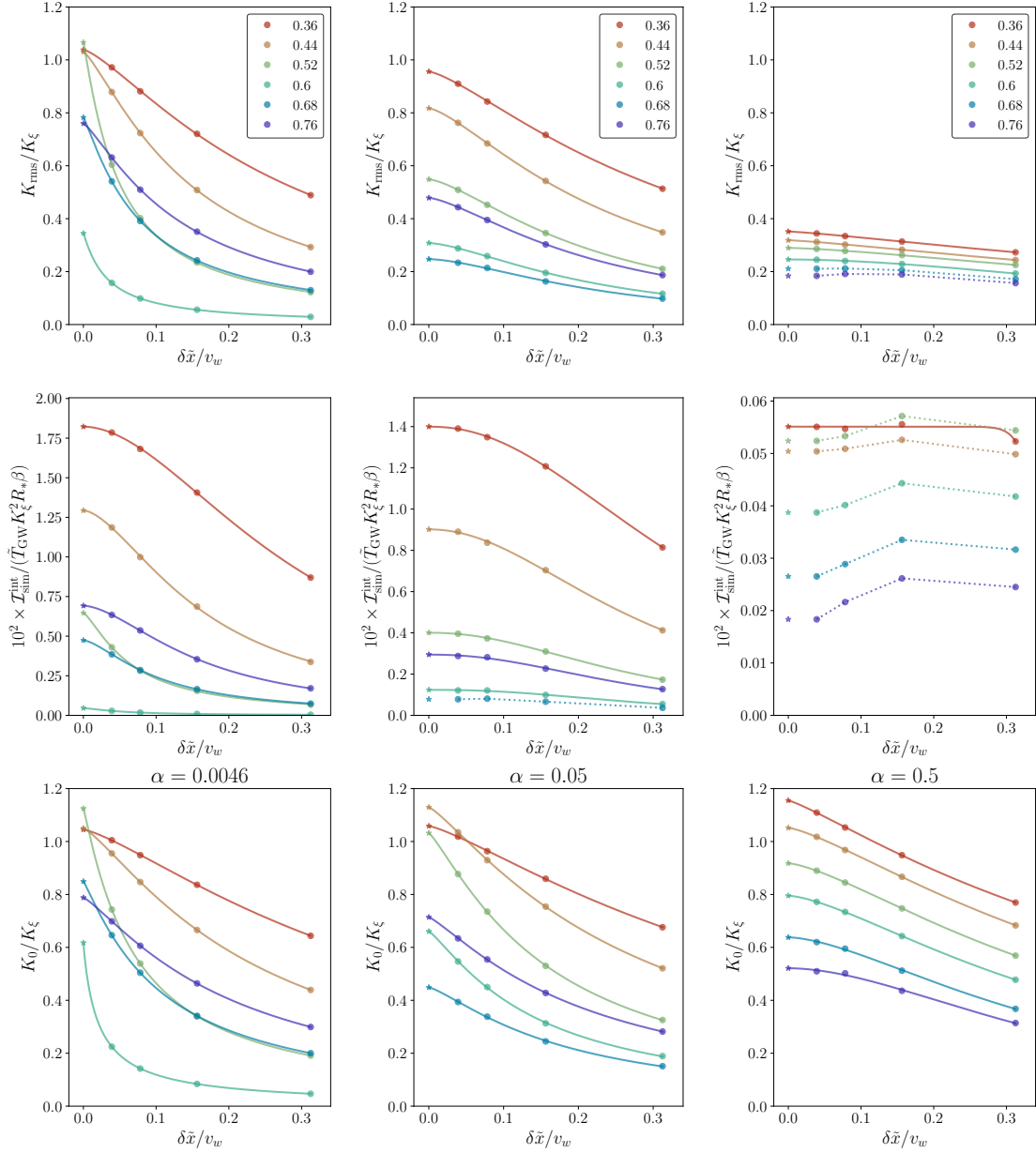


Figure 2. Plots showing the kinetic energy fraction K and the integrated GW spectrum $\mathcal{I}_{\text{sim}}^{\text{int}}$ as a function of grid spacing $\delta\tilde{x}/v_w = (\tilde{L}/v_w)/N$ for runs with $\tilde{L}/v_w = 20$. Upper and middle panels respectively show the rms value of the kinetic energy fraction $K_{\text{rms}} \equiv K_{\text{int}}/\tilde{T}_{\text{GW}}^{1/2}$, normalized by the single-bubble kinetic energy fraction K_ξ [see Eq. (2.19) and Tab. 3], and the integrated GW spectrum $\mathcal{I}_{\text{sim}}^{\text{int}}$, normalized by a reference value $\tilde{\Omega}_{\text{GW}} \sim 10^{-2}$ [40, 50, 52], and by $\tilde{T}_{\text{GW}} K_\xi^2 R_* \beta$, based on the expected scaling of Eq. (2.23). Both K_{rms} and $\mathcal{I}_{\text{sim}}^{\text{int}}$ are computed for $\tilde{t}_{\text{init}} = 16$ and $\tilde{t}_{\text{end}} = 32$, with $\tilde{T}_{\text{GW}} = 16$. The lower panels show the kinetic energy fraction at the time when all the simulation domain is in the broken phase around $\tilde{t}_0 \simeq 10$, K_0 , also normalised by K_ξ . Left, middle, and right columns are weak, intermediate, and strong PTs respectively. Solid lines show the least-squares fits of the extrapolation scheme given in Eq. (4.1) when the fit is valid, while dotted lines indicate the numerical trend when the fit is not valid (see discussion in the main text). Stars indicate the extrapolated values at $\delta\tilde{x} \rightarrow 0$.

spectrum, the fit of Eq. (4.1) is valid for weak and intermediate PTs, but not for strong PTs, for most of the wall velocities. Indeed, the quantity plotted in Fig. 2 is expected to be [see Eqs. (2.23) and (4.3)]

$$\frac{10^2 \times \mathcal{I}_{\text{int}}^{\text{sim}}}{\tilde{T}_{\text{GW}} K_{\xi}^2 R_* \beta} \simeq \frac{K_{\text{rms}}^2}{K_{\xi}^2}, \quad (4.4)$$

and the presence of the square of the rms kinetic energy worsen the effect already observed for K_{rms} , due to the particular behaviour of the time evolution of the kinetic energy with increasing resolution. In the cases when the fit is not valid, we take the extrapolated values in Fig. 2 as those obtained for the largest resolution runs with $N = 512$.

We find empirically that the exponent a in Eq. (4.1) usually varies between one and two, indicating that the dynamics of the system reduces the effective degree of convergence with respect to the one expected from the numerical scheme, which corresponds to second order [56, 58]. We expect that further decreasing $\delta\tilde{x}$ significantly below δx_* would be required to find an exact quadratic dependence of the error with $\delta\tilde{x}$. In any case, we note that for most of the PTs (besides highly confined profiles with $v_w \lesssim v_{\text{CJ}}$), we already find absolute errors below 10%, as indicated in Tab. 2. For confined profiles, the relative error is large, and we need to take into account that the extrapolated result K_{∞} presents a larger degree of uncertainty. In these simulations, we expect the lack of convergence to also become visible in the GW spectra: For example, we observe that the expected UV behavior, $S(k) \sim k^{-3}$, found in the sound-shell model [51, 54, 59, 60] and in PT simulations [40, 50, 52] is in these cases obscured by an exponential decay (see the discussion in Sec. 4.4

| α | \tilde{L}/v_w | v_w | $K_{\infty}^{\text{rms}}/K_{\xi}$ | a_K | ε_K | $\mathcal{I}_{\infty}^{\text{int}}$ | $a_{\mathcal{I}}$ | $\varepsilon_{\mathcal{I}}$ |
|----------|-----------------|-------|-----------------------------------|-------|-----------------------|-------------------------------------|-------------------|-----------------------------|
| 0.0046 | 20 | 0.36 | 1.04 | 1.34 | 6.41×10^{-2} | 9.97×10^{-10} | 1.88 | 2.04×10^{-2} |
| | | 0.44 | 1.03 | 1.29 | 1.47×10^{-1} | 2.11×10^{-9} | 1.64 | 8.26×10^{-2} |
| | | 0.52 | 1.07 | 1.11 | 4.33×10^{-1} | 5.35×10^{-9} | 1.34 | 3.35×10^{-1} |
| | | 0.60 | 0.35 | 1.06 | 5.44×10^{-1} | 5.36×10^{-9} | 1.36 | 3.83×10^{-1} |
| | | 0.68 | 0.78 | 1.16 | 3.08×10^{-1} | 2.35×10^{-9} | 1.51 | 1.87×10^{-1} |
| | | 0.76 | 0.76 | 1.26 | 1.69×10^{-1} | 1.19×10^{-9} | 1.69 | 8.38×10^{-2} |
| 0.05 | 20 | 0.36 | 0.96 | 1.35 | 4.80×10^{-2} | 8.65×10^{-6} | 2.16 | 6.70×10^{-3} |
| | | 0.44 | 0.82 | 1.40 | 6.72×10^{-2} | 1.24×10^{-5} | 2.04 | 1.26×10^{-2} |
| | | 0.52 | 0.55 | 1.46 | 7.21×10^{-2} | 1.33×10^{-5} | 2.14 | 1.20×10^{-2} |
| | | 0.60 | 0.31 | 1.54 | 6.52×10^{-2} | 1.04×10^{-5} | 2.43 | 2.13×10^{-2} |
| | | 0.68 | 0.25 | 1.61 | 5.52×10^{-2} | 8.10×10^{-6} | – | 3.49×10^{-2} |
| | | 0.76 | 0.48 | 1.44 | 7.37×10^{-2} | 6.98×10^{-6} | 2.21 | 2.28×10^{-2} |
| 0.5 | 20 | 0.36 | 0.35 | 1.25 | 2.06×10^{-2} | 1.82×10^{-3} | 25.03 | 7.14×10^{-4} |
| | | 0.44 | 0.32 | 1.27 | 2.05×10^{-2} | 2.18×10^{-3} | – | 9.55×10^{-3} |
| | | 0.52 | 0.29 | 1.44 | 1.26×10^{-2} | 2.79×10^{-3} | – | 1.74×10^{-2} |
| | | 0.60 | 0.25 | 1.85 | 3.97×10^{-3} | 2.56×10^{-3} | – | 3.68×10^{-2} |
| | | 0.68 | 0.21 | – | 3.97×10^{-3} | 2.26×10^{-3} | – | 8.88×10^{-2} |
| | | 0.76 | 0.18 | – | 3.91×10^{-2} | 1.80×10^{-3} | – | 1.80×10^{-1} |

Table 2. Numerical values of the fit parameters a , K_{∞}^{rms} , and $\mathcal{I}_{\infty}^{\text{int}}$ of Eq. (4.1) for the rms value of the kinetic energy fraction K_{rms}/K_{ξ} and the integrated GW amplitude $\mathcal{I}_{\text{sim}}^{\text{int}}$, respectively shown in the top and middle panels of Fig. 2. We present the relative errors ε computed by comparing the extrapolated values to those obtained in the largest resolution runs $N = 512$ when the fit works (see discussion in the main text). Otherwise (indicated with ‘–’ in the values of a), the error is computed from the relative difference between the two largest resolution runs, $N = 256$ and $N = 512$.

and the fit used in Ref. [58]).

Finally, we also display in Fig. 2 the kinetic energy fraction K_0 at the time when the PT ends, $\tilde{t}_0 \simeq 10$, computed after getting rid of oscillations over time as obtained from the fit in Eq. (4.7) (see discussion in Sec. 4.2 and Fig. 4). As we will see later, in the parameterization we choose, K_0 is essential to determine the amplitude of the GW spectrum, as apparent from Eqs. (2.23) and (2.28). Therefore, to correctly capture the GW amplitude we need to accurately reproduce K_0 . A first option can be to directly take the values K_∞^0 extrapolated from the fit of Eq. (4.1) (corresponding to the stars in the lowest panels of Fig. 2). However, the analysis performed in this section does not take into account that the self-similar profiles have not reached convergence at the time when the bubbles collide, but only models the overall effect of the lattice resolution. We have seen that this is good enough in most of the cases for time-integrated quantities like K_{rms} and $\mathcal{I}_{\text{sim}}^{\text{int}}$. However, K_0 is the kinetic energy shortly after collisions, and it is therefore more sensitive to what happens in the fluid self-similar profiles. In App. B, we present a methodology to estimate the required correction from the under-resolution of the fluid profiles. The corrected values \mathcal{K}_0/K_ξ are presented in Fig. 3, together with a modified “efficiency” κ_0 , such that

$$\mathcal{K}_0 \equiv \frac{\kappa_0 \alpha}{1 + \alpha}, \quad (4.5)$$

in analogy to Eq. (2.19). We find a general trend that $\mathcal{K}_0/K_\xi \gtrsim 1$ when $v_w < c_s$, while $\mathcal{K}_0/K_\xi \lesssim 1$ when $v_w > c_s$. If we take an average value of \mathcal{K}_0 over the PT parameters v_w and α , we find

$$\mathcal{K}_0 = 0.84_{-0.29}^{+0.24} K_\xi, \quad (4.6)$$

where the super and subscripts are the maximum and minimum values found over all wall velocities, indicating that the typical use of K_ξ for the kinetic energy would overestimate the GW production by a factor $(K_\xi/\mathcal{K}_0)^2$, which can be as large as $0.55^{-2} \sim 3.3$, for example when $\alpha = 0.5$ and $v_w = 0.8$ (see Fig. 2). For different PT parameters (α and v_w), one could take the values of Fig. 3 to predict the correction to the resulting GW amplitude. According to the locally stationary UETC presented in Sec. 2.5, we find that $K_{\text{int}}^2 \equiv K_{\text{rms}}^2 \tilde{T}_{\text{GW}}$ is the relevant quantity determining the GW amplitude. Therefore, based on the results of Ref. [58], Ref. [97] used the estimated value $K_{\text{rms}} \simeq 0.6 K_\xi$. However, we note that using the power-law fit presented in Sec. 2.5 and validated in Sec. 4.2, we can relate K_{int}^2 to the corrected values \mathcal{K}_0 and the decay rate b (as we will do in Sec. 4.3).

4.2 Time evolution of the kinetic energy

In this section, we evaluate the time evolution of the kinetic energy fraction K for different numerical resolutions N . We show the results of $K(\tilde{t})/K_\xi$ in Fig. 4 for the largest resolution runs $N = 512$ (upper panel), and for a range of $N = \{64, 128, 256, 512\}$ (lower panel). From the upper panels of Fig. 4 one can appreciate that, at late times $\tilde{t} \gtrsim \tilde{t}_0 \approx 10$, when the broken phase has filled the whole simulation volume, the kinetic energy decays with time. By analyzing how this decay depends on the numerical resolution, in the following we argue that the origin of this decay is most probably numerical for weak and most of intermediate

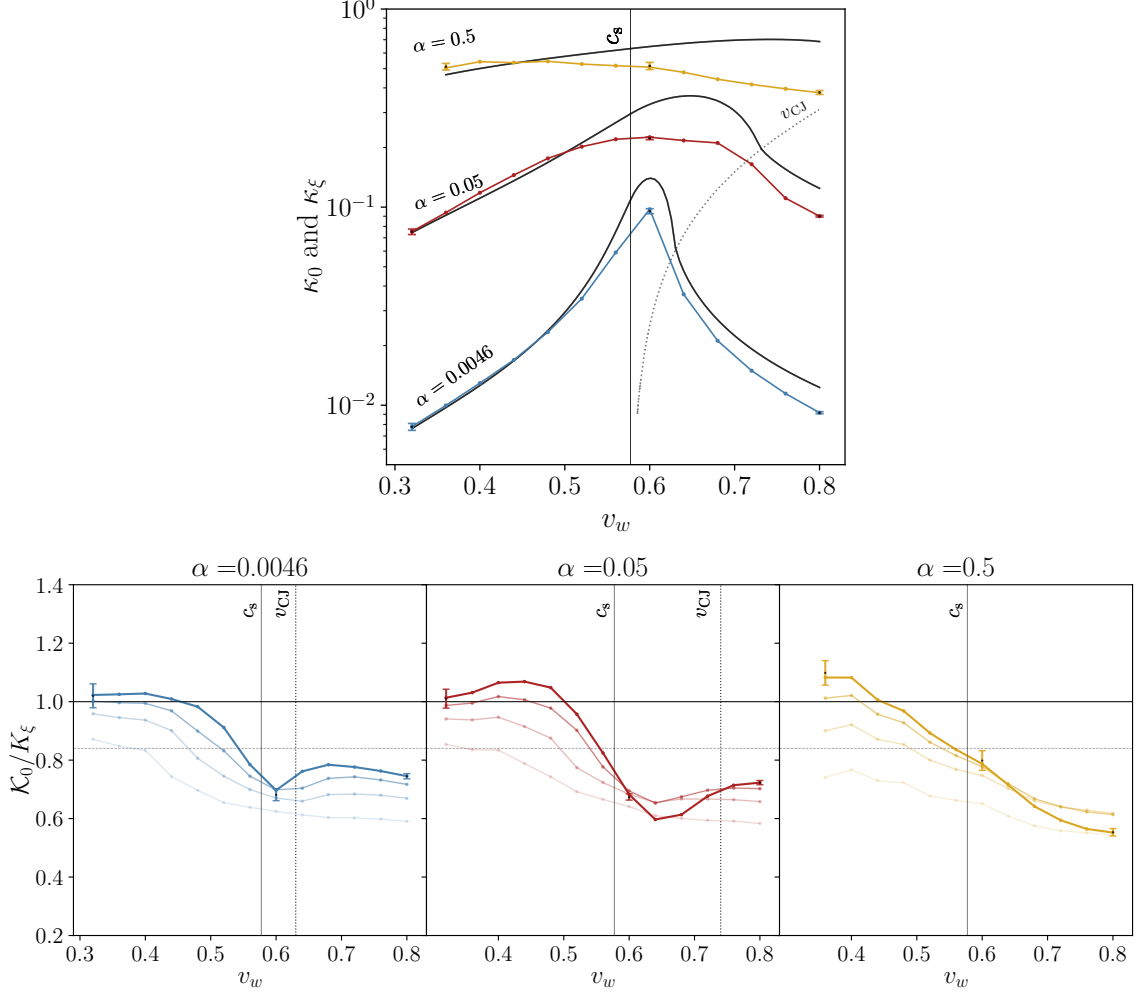


Figure 3. *Upper panel:* Kinetic energy efficiency $\kappa_0 \equiv K_0(1 + \alpha)/\alpha$ obtained from correcting the numerical K_0 when $N = 512$ and $\tilde{L}/v_w = 20$ (see App. B) for weak (blue), intermediate (red), and strong (orange) PTs, compared to κ_ξ (black) for self-similar solutions [see Eq. (2.19)]. Vertical line corresponds to c_s , and v_{CJ} is indicated by the dotted gray line. *Lower panel:* the single-bubble-corrected kinetic energy fraction at the time when the PT completes, K_0 , normalized to K_ξ for self-similar profiles [see Eq. (2.19)], for weak (left panel), intermediate (middle panel), and strong (right panel) PTs, as a function of v_w . Lines in increasing opacity correspond to increasing numerical resolution $N \in \{64, 128, 256, 512\}$. The horizontal line indicates the average value over v_w and α , $K_0/K_\xi \simeq 0.84$ [see Eq. (4.6)]. The vertical solid gray line indicates the sound speed, c_s , while the dashed lines indicate the Chapman-Jouguet velocity, v_{CJ} . Error bars show the standard deviation from 10 different bubble nucleation histories.

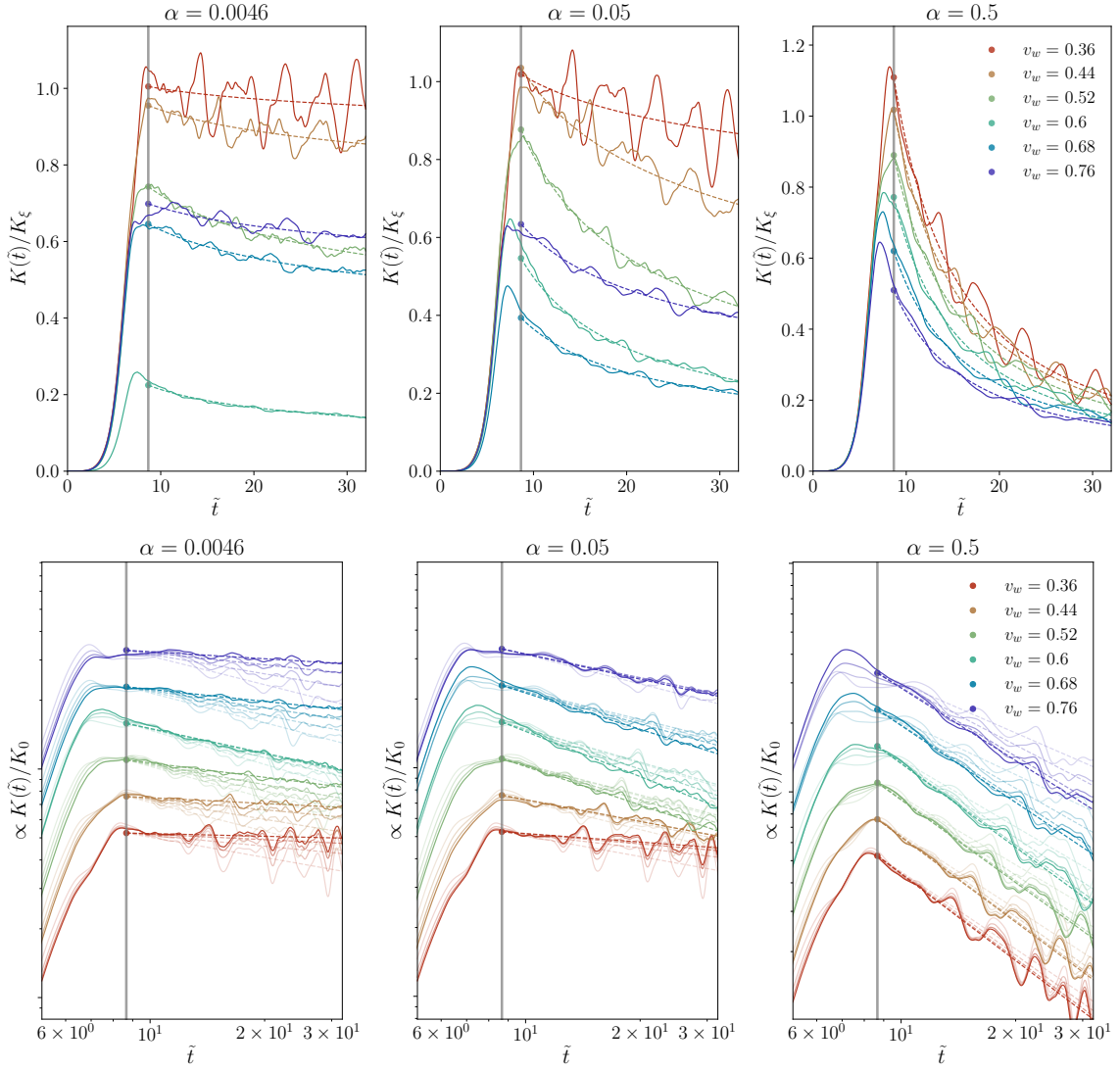


Figure 4. Evolution of the measured kinetic energy fraction $K(\tilde{t})$ normalized to the single-bubble values K_ξ [see Eq. (2.19) and Tab. 3] for weak (left columns), intermediate (middle columns), and strong (right columns) PTs, for $N = 512$ (solid lines) and $\tilde{L}/v_w = 20$, and the same wall velocities as those in Fig. 2. Dashed lines indicate the fits to the power-law decay of Eq. (4.7) at times $\tilde{t} > \tilde{t}_0$. Values corresponding to K_0/K_ξ are marked with circles. In the lower panel, the kinetic energy fraction is shown for different numerical discretizations $N = \{64, 128, 256, 512\}$ (solid lines with increasing opacity), normalized to the corresponding values of the fit K_0 at each resolution N . The results for each v_w are shifted by a constant to distinguish between wall velocities. This presentation in the lower panel is chosen to emphasize the dependence of the time decay on resolution.

PTs, while it is probably physical for intermediate PTs with thin hybrid profiles ($v_w \lesssim v_{\text{CJ}}$) and strong ones.

In Sec. 4.1 and App. B, we demonstrated that, at early times, while the self-similar profiles develop in each nucleated bubble before it collides, the kinetic energy is underestimated for low resolution (see Figs. 14 and 15). To study the dependence of the kinetic

energy decay rate with resolution, we show in the lower panels of Fig. 4 the evolution of $K(\tilde{t})$ normalized by the corresponding values of K_0 . For weak and most of intermediate PTs, one can appreciate that the decay of the kinetic energy with time becomes less pronounced as we increase the resolution N , which is consistent with the growth of both K_{rms} and K_0 with N observed in Fig. 2. Since the kinetic energy is typically damped by numerical viscosity,⁷ it is in general expected that the decay is less pronounced when the grid spacing is reduced: the weak and most of intermediate PTs conform with this expectation.

However, the opposite trend is found for intermediate PTs with thin hybrid profiles ($v_w \lesssim v_{\text{CJ}}$) and strong ones: in the decaying phase of the kinetic energy, the decay becomes steeper with smaller grid spacing (see the middle and right low panels of Fig. 4). In these cases, the enhancement of the decay with resolution would be consistent with the fact that, as the fluid shells carry larger kinetic energies at the time of collisions, non-linearities are enhanced. From energy conservation, we then expect that, as non-linearities develop, kinetic energy transfers from larger to smaller scales, where it can be converted to thermal energy at the scale determined by numerical viscosity. If this physical process damps kinetic energy more efficiently than the numerical dissipation, which might indeed happen in the case of strong PTs, we expect the decay to increase with resolution, as higher resolution means a better modeling of the physical damping process.

In addition to the time decay, K also oscillates in time. This occurs in particular for weak PTs, and is more pronounced for small v_w , away from hybrid solutions. In these cases, the oscillations can be associated to the sound-wave regime, where an oscillatory conversion between kinetic and thermal energies is expected, and confirmed by the fact that we conserve T^{00} to machine precision (see results in App. C of Ref. [58]).

To better quantify the decay of the kinetic energy with time, we use a power law, effectively getting rid of the oscillations over time. We fit the numerical results at times $\tilde{t} > \tilde{t}_0$ when the PT is complete, using the following power-law decay with time,

$$K(\tilde{t} > \tilde{t}_0) = K_0 \left(\frac{\tilde{t}}{\tilde{t}_0} \right)^{-b}, \quad (4.7)$$

where b indicates the power-law decay rate of K . This prescription has already been discussed in Sec. 2.5 (note that here we set the initial simulation time $\tilde{t}_{\text{ref}} = 0$), and accurately fits the numerical data as shown by Fig. 4. We have checked that it remains accurate up to $\tilde{t}_{\text{end}} = 64$ for an example strong PT with $\alpha = 0.5$ and $v_w = 0.8$. We define the half-life of the kinetic energy as the time when $K(\tilde{t}_0 + \tilde{\tau}_{1/2}) = \frac{1}{2}K_0$, i.e.,

$$\tilde{\tau}_{1/2} = \left(2^{\frac{1}{b}} - 1 \right) \tilde{t}_0. \quad (4.8)$$

We display in Fig. 5 the fit of the decay index b (left) as well as the half-life $\tilde{\tau}_{1/2}$ (right) as a function of v_w for weak, intermediate, and strong PTs.⁸ In the right panel of Fig. 5,

⁷In the Kurganov-Tadmor scheme used in our simulations [58], the numerical viscosity is expected to scale proportional to $(\delta\tilde{x})^3$ [101].

⁸This time, we refrain from extrapolating to infinite resolution due to the complex behavior of the index. We only plot the results obtained with the two largest resolutions $N = \{256, 512\}$, and with the best resolution in the UV regime, $\tilde{L}/v_w = 20$.

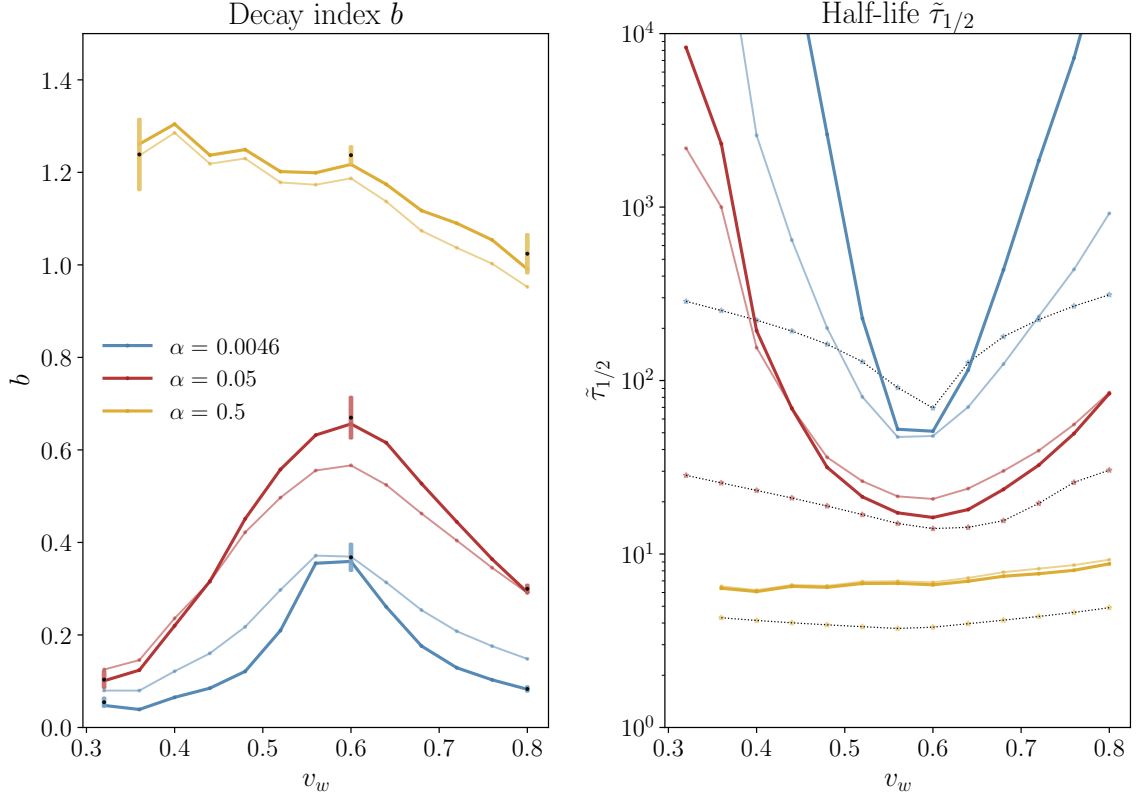


Figure 5. Decay index b (left panel) and half-life of the kinetic energy fraction $\tilde{\tau}_{1/2}$ (right panel) as a function of v_w for $N = \{256, 512\}$ in increasing opacity for weak (blue lines), intermediate (red lines), and strong (orange lines) PTs. Error bars in the left panel show the standard deviation from 10 different bubble nucleation histories for $N = 512$. Dashed black lines with colored stars in the right panel correspond to the shock time $\tilde{\tau}_{sh} = \beta R_*/\sqrt{K_\xi}$ (see values in Tab. 3), which we compare with $\tilde{\tau}_{1/2}$ as we expect both time scales to be inversely proportional to K_ξ .

we also plot the shock time, which corresponds to the time scale of shock formation in the plasma and it is expected to determine the time of decay into non-linear turbulent motion. Comparing the numerical $\tilde{\tau}_{1/2}$ to $\tilde{\tau}_{sh}$ is therefore useful to interpret the development of non-linearities in the simulations. In order to avoid the uncertainty due to the underestimation of the kinetic energy in simulations, we evaluate $\tilde{\tau}_{sh}$ with the kinetic energy ratio expected for uncollided bubbles, $\tilde{\tau}_{sh} = \beta R_*/\sqrt{K_\xi}$ (see Tab. 3 for numerical values). The shock time becomes $\tilde{\tau}_{sh} \simeq 4$ for strong PTs, $\tilde{\tau}_{sh} \sim \mathcal{O}(10)$ for intermediate PTs, and $\tilde{\tau}_{sh} \sim \mathcal{O}(100)$ for weak PTs. Therefore, the time scale for non-linearities to develop can be reached within the simulation for strong and some intermediate PTs, while weak PTs should remain in the linear regime for the entire duration of the simulations, and they would develop non-linearities at later times. In some intermediate PTs, the shock time is reached towards the end of our simulations. These expectations are in agreement with the simulation results. We briefly discuss in App. C the presence of vorticity in our simulations, and present some preliminary results. To properly evaluate the development of vortical motion more detailed work is needed.

For weak transitions, the rate of kinetic energy damping is reduced when increasing the resolution, as already discussed above in the context of the low panels of Fig. 4. We interpret this trend as due to the reduction of the numerical viscosity (see footnote 7). This is indeed confirmed by the behaviour of both b and $\tilde{\tau}_{1/2}$ with resolution, shown in Fig. 5, blue lines: the decay exponent diminishes with increasing resolution, while the half-life of the kinetic energy grows, and bears no relation with the shock time. This means that for weak transitions, the decay is always dominated by numerical viscosity. Only for the hybrid solution with $v_w = 0.6 \lesssim v_{\text{CJ}}$, when larger fluid velocities can be achieved (see self-similar profiles in Fig. 13), does b (and hence $\tilde{\tau}_{1/2}$) appear to stagnate with increasing resolution, pointing towards the onset of resolving the physics responsible for the damping. However, in this extreme case, the fluid profile is highly confined and the simulations are far from reaching the converged profiles (see Figs. 14 and 15), so it is not completely clear whether the obtained decay rate b is physical.

The results are more interesting in the case of intermediate transitions. For small v_w , corresponding to subsonic deflagrations, b decreases with increasing resolution, and $\tilde{\tau}_{1/2}$ increases correspondingly. However, for a large range of intermediate velocities $v_w \in \{0.52, 0.6, 0.68\} \lesssim v_{\text{CJ}}$, the trend is reversed. We interpret this point of reversal as a transition from a decay of the kinetic energy dominated by numerical viscosity to a decay determined by the development of non-linearities. We note that in this case, some of the confined hybrids are still under-resolved, but this is no longer the case for the subsonic deflagration with $v_w = 0.52$, indicating that the decay rate seems to be physical (see Figs. 4 and 15). Furthermore, a similar decay of the kinetic energy was already found for intermediate PT simulations of the scalar-fluid system [52, 78].

For strong transitions, we are universally in the regime where increasing the numerical resolution N leads to a larger decay rate, indicating that the physical non-linear decay dominates over the numerical viscosity. As discussed above, this is expected to be the case, as the expected time scale for non-linearities to develop, i.e., the shock formation time, is around $\tilde{\tau}_{\text{sh}} \simeq 5$, occurring during the duration of our numerical simulations. The fact that both b and $\tilde{\tau}_{1/2}$ are virtually independent on the value of v_w indicates that the possible under-resolution of the initial fluid profiles is no longer an issue as far as the fluid dynamics is concerned. However, this could also be a consequence of the low variability of K_ξ with v_w for strong PTs (see values in Tab. 3).

4.3 Dependence of the integrated GW amplitude with the source duration and GW efficiency

In this section, we analyze how the GW energy density depends on the source duration, with the aim of consolidating, with the result of simulations, both the model described in Sec. 2.4, and its generalization to decaying sources proposed in Sec. 2.5. For this purpose, we study two quantities as a function of the simulation time, which corresponds to the source duration: the integrated GW amplitude $\mathcal{I}_{\text{sim}}^{\text{int}} \equiv \int \mathcal{I}_{\text{sim}} d \ln k$, and the GW efficiency $\tilde{\Omega}_{\text{GW}}$.

The first quantity is shown in the upper panels of Fig. 6, where $\mathcal{I}_{\text{sim}}(\tilde{t}_{\text{init}}, \tilde{t}, k)$ is evaluated at $\tilde{t}_{\text{init}} = 16$, while \tilde{t} can vary from \tilde{t}_{init} to $\tilde{t}_{\text{end}} = 32$ [see Eq. (2.10)]. For weak

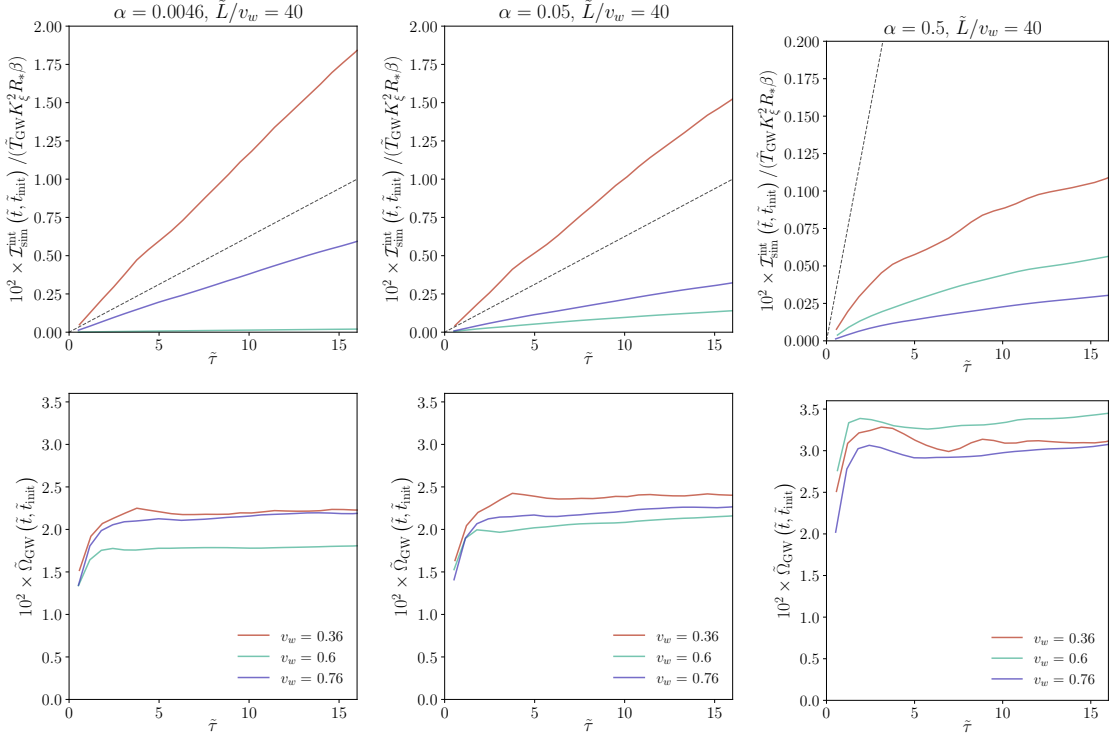


Figure 6. *Upper panel:* the numerical integrated GW amplitude found in the simulations with $\tilde{L}/v_w = 40$ and $N = 512$, as a function of the source duration $\tilde{\tau} \equiv \tilde{t} - \tilde{t}_{\text{init}}$ for weak (left columns), intermediate (middle columns), and strong (right columns) PTs. The integrated GW amplitude is normalized as in the middle panel of Fig. 2. Dashed lines correspond to the linear growth with $K_{\text{rms}}^2 = K_{\xi}^2$ and $\tilde{\Omega}_{\text{GW}} = 10^{-2}$. *Lower panel:* the GW production efficiency $\tilde{\Omega}_{\text{GW}}$ also as a function of time, computed using Eq. (4.11).

and some intermediate PTs, the usual stationary assumption of the sound-wave regime presented in Sec. 2.4 should apply, as illustrated in previous numerical work [40, 50, 52, 56, 58]. Indeed, we confirm that in these cases, K does not significantly evolve with time within the simulations (see Fig. 4). Therefore, according to the model of Sec. 2.4, we expect $\mathcal{I}_{\text{sim}}^{\text{int}}(\tilde{t}_{\text{init}}, \tilde{t})$ to grow linearly in time with the source duration $\tilde{\tau} \equiv \tilde{t} - \tilde{t}_{\text{init}}$, cf. Eq. (2.15):

$$\frac{\mathcal{I}_{\text{sim}}^{\text{int}}(\tilde{t}_{\text{init}}, \tilde{t})}{\tilde{T}_{\text{GW}} K_{\xi}^2 \beta R_{*}} = \tilde{\Omega}_{\text{GW}} \left(\frac{K}{K_{\xi}} \right)^2 \frac{\tilde{\tau}}{\tilde{T}_{\text{GW}}}, \quad (4.9)$$

where $\tilde{\tau}_{\text{fin}} = \tilde{t}_{\text{fin}} - \tilde{t}_{*}$ in Eq. (2.15) is now replaced by $\tilde{\tau}$, and we have normalized the left hand side as in the upper panels of Fig. 6 (and middle panels of Fig. 2). From this figure, one can appreciate that the linear dependence with the source duration of the GW amplitude, predicted by the sound-shell model, is indeed in good agreement with the simulation results for weak and some intermediate PTs. From Eq. (4.9), it appears that the slope of the linear growth, as plotted in Fig. 6, depends on the ratio $(K/K_{\xi})^2/\tilde{T}_{\text{GW}}$. For confined hybrids, e.g., for $\alpha = 0.0046$ and $v_w = 0.6$, the underestimation of the kinetic energy K with respect to the single bubble one K_{ξ} , due to poor numerical resolution (see Fig. 2 and discussion in

App. B), causes the slope to be small, and the GW amplitude to increase slowly.

On the other hand, for strong PTs with $\alpha = 0.5$, and also for $\alpha = 0.05$ with intermediate wall velocities $v_w \in \{0.6, 0.68\} \lesssim v_{\text{CJ}}$, the decay of K is significant within the time of our simulations, and we observe deviations with respect to the linear dependence with $\tilde{\tau}$. In these cases, the effect of the time evolution of K needs to be incorporated, as put forward in the context of the locally stationary UETC presented in Sec. 2.5, which proposes to generalize the linear growth to a growth proportional to $K_{\text{int}}^2(\tilde{t}_{\text{init}}, \tilde{t})$, see Eq. (2.23). The integrated GW amplitude plotted in Fig. 6 becomes then

$$\frac{\mathcal{I}_{\text{sim}}^{\text{int}}(\tilde{t}_{\text{init}}, \tilde{t})}{\tilde{T}_{\text{GW}} K_{\xi}^2 \beta R_*} = \tilde{\Omega}_{\text{GW}} \frac{K_{\text{rms}}^2}{K_{\xi}^2} = \tilde{\Omega}_{\text{GW}} \left(\frac{K_0}{K_{\xi}} \right)^2 \frac{\tilde{t}_{\text{init}}}{\tilde{T}_{\text{GW}}} \left(\frac{\tilde{t}_0}{\tilde{t}_{\text{init}}} \right)^{2b} \frac{(\tilde{t}/\tilde{t}_{\text{init}})^{1-2b} - 1}{1 - 2b}, \quad (4.10)$$

where the second equality corresponds to Eq. (2.28) (with $\tilde{t}_{\text{ref}} = 0$), and holds as long as the fit $K(\tilde{t}') = K_0 (\tilde{t}'/\tilde{t}_0)^{-b}$ accurately represents the numerical results at times $\tilde{t}' \in [\tilde{t}_{\text{init}}, \tilde{t}]$ (see Fig. 4). From Fig. 5, we see that $b > 1/2$ for strong PTs and intermediate ones with velocities close to v_{CJ} . Equation (4.10) then implies that the integrated GW amplitude grows slower than linearly for $\tilde{t} > \tilde{t}_{\text{init}}$, eventually saturating to a constant value if the duration is long enough [cf. also Eq. (2.29)]. Indeed, the simulations confirm this behaviour, as shown in Fig. 6, supporting the model proposed in Sec. 2.5.

Another way to test the validity of the models put forward in Secs. 2.4 and 2.5 is to study the GW efficiency $\tilde{\Omega}_{\text{GW}}$ defined in Eq. (2.17), which, according to them, should be constant with the source duration [cf. Eq. (2.15) and its generalization (2.23)]. Therefore, we plot in the lower panel of Fig. 6 the following ratio

$$\tilde{\Omega}_{\text{GW}}(\tilde{t}) = \frac{\mathcal{I}_{\text{sim}}^{\text{int}}(\tilde{t}_{\text{init}}, \tilde{t})}{K_{\text{int}}^2(\tilde{t}_{\text{init}}, \tilde{t})(\beta R_*)}, \quad (4.11)$$

with the objective of estimating the GW efficiency as a function of the source duration, while also including the effect of the decay of K . We note that when K does not significantly decay with time, $K_{\text{int}}^2 \rightarrow K^2 \tilde{T}_{\text{GW}}$ and Eq. (4.11) goes back to the usual definition Eq. (2.17), valid within the stationary assumption of the sound-shell model. After an initial steep increase with time, which is a just numerical artifact from abruptly starting the GW computation at \tilde{t}_{init} , $\tilde{\Omega}_{\text{GW}}(\tilde{t})$ stabilises to virtually constant values across all PT strengths and all values of v_w , again validating the generalization of the linear growth to a growth proportional to $K_{\text{int}}^2(\tilde{t}_{\text{init}}, \tilde{t})$ as found within the locally stationary UETC proposed in Sec. 2.5.

Since we find that $\tilde{\Omega}_{\text{GW}}(\tilde{t})$ is roughly constant with the source duration after incorporating K_{int}^2 in the scaling of the GW amplitude (see Eq. (4.11) and Fig. 6), in the rest of the paper we take its value at the end of the simulations \tilde{t}_{end} . The resulting GW efficiency $\tilde{\Omega}_{\text{GW}}(\tilde{t}_{\text{end}})$, computed from Eq. (4.11), is shown in Fig. 7 for different numerical resolutions N and box sizes $\tilde{L}/v_w = 20$ and 40, and also using the extrapolated values to $\delta\tilde{x} \rightarrow 0$ of $\mathcal{I}_{\text{sim}}^{\text{int}}$ and K_{int} , as described in Sec. 4.1 (see also Fig. 2). The error bars show the standard deviation obtained from 10 different bubble nucleation histories, corresponding to the *seeds* set of simulations listed in Tab. 1. We also compare in Fig. 7 the extrapolated $\tilde{\Omega}_{\text{GW}}(\tilde{t}_{\text{end}})$

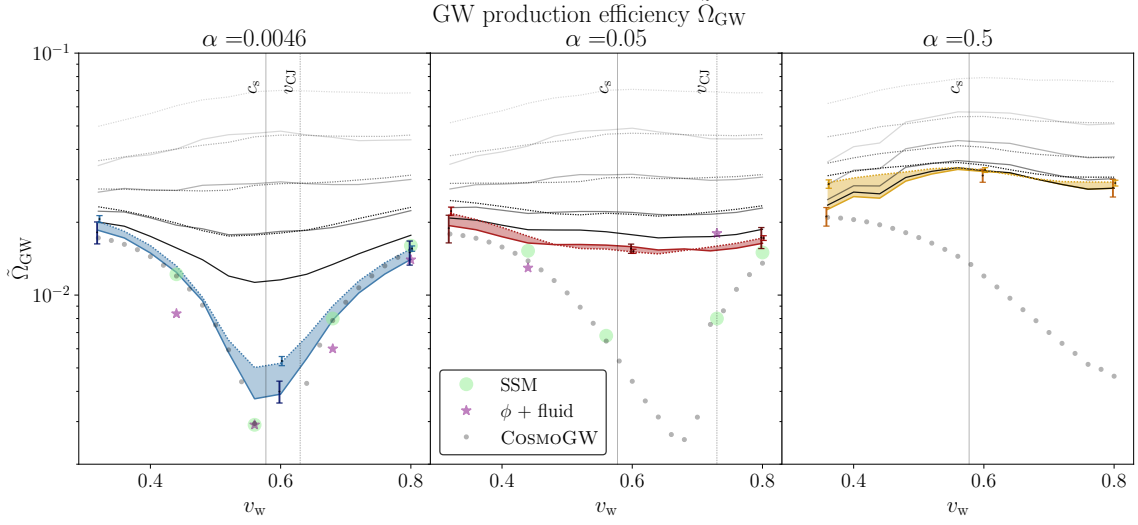


Figure 7. Gravitational wave production efficiency $\tilde{\Omega}_{\text{GW}}$ for weak (left), intermediate (middle), and strong (right) first-order PTs. Solid (dotted) lines correspond to $\tilde{L}/v_w = 20$ (40). Black lines with increasing opacity correspond to increasing resolutions $N \in \{64, 128, 256, 512\}$, while colored lines are the values extrapolated to the continuum limit $\delta\tilde{x} \rightarrow 0$. Green dots and violet stars mark $\tilde{\Omega}_{\text{GW}}$ as presented in Tabs. 2 and 3 of Ref. [54] corresponding to predictions from the sound-shell model (SSM) for exponential nucleation of bubbles [54] and scalar field-hydrodynamical simulations for simultaneous nucleation [52], respectively. Gray dots correspond to sound-shell model values found using the assumption described in Sec. 2.4, following App. B of Ref. [59], and computed using COSMOGW [84]. Error bars indicate the standard deviation from 10 different bubble nucleation histories for $\tilde{L}/v_w = 20$ (darker) and 40 (lighter).

with the values of the efficiency found using the sound-shell model [51, 54] as described in Sec. 2.4 (see also App. B of Ref. [59]), and with those obtained from numerical simulations of the full coupled scalar field-fluid system [50, 52]. Note that the latter are found using simultaneous bubble nucleation, which in general leads to smaller $\tilde{\Omega}_{\text{GW}}$ compared to exponential nucleation used in this work (see Tabs. 2 and 3 in Ref. [54]). We have also modified the values of $\tilde{\Omega}_{\text{GW}}$ from Refs. [50, 52, 54] to take into account that they consider $\beta R_* = (8\pi)^{1/3} v_w$, instead of the corrected $\beta R_* = (8\pi)^{1/3} \max(v_w, c_s)$ that we use in Eq. (2.23). Concerning the values of $\tilde{\Omega}_{\text{GW}}$ found using the sound-shell model, they should also be modified to include the structure that develops in the GW spectrum below the peak for some values of the PT parameters, an effect pointed out for the first time in Ref. [59]. However, we neglect this effect here, for two reasons: (1) as discussed in Sec. 2.4, when the kinetic energy is small, the stationary assumption of the sound-shell model is valid. Therefore, for weak PTs, the integral in wave numbers necessary to evaluate $\tilde{\Omega}_{\text{GW}}$ should not be strongly affected by including the correct spectral shape at low wave numbers. (2) the dynamical range in the IR available in our and previous simulations is usually not large enough to clearly reconstruct the exact spectral shape described in Ref. [59], see results in Sec. 4.4.

For weak transitions (left panel of Fig. 7 with $\alpha = 0.0046$), the extrapolated $\tilde{\Omega}_{\text{GW}}$

obtained from the Higgsless simulations accurately reproduces both the results of the sound-shell model and of the coupled scalar field-hydrodynamical simulations [50, 52]. The agreement between three independent approaches supports the conclusion that the dependence of $\tilde{\Omega}_{\text{GW}}$ with v_w may then be physical.

However, for intermediate PTs, we begin to observe deviations from the sound-shell model, in particular for large v_w . The middle panel of Fig. 7 shows that the v_w dependence present for weak PTs has flattened, and that the overall efficiency $\tilde{\Omega}_{\text{GW}}$ is larger than the sound-shell model results. We are reasonably confident that this result is physical, for two reasons. First of all, the extrapolation method described in Sec. 4.1 and presented in Fig. 7 as solid and dotted lines seems to behave very well, delivering agreement between the numerical results from both simulation domains $\tilde{L}/v_w = 20$ and 40. Second, our findings are also consistent with the two available data points for scalar field-hydrodynamical simulations from Ref. [52] (violet stars). As α grows, non-linearities become more relevant, and simulations are then necessary to push beyond the validity reach of the sound-shell model; however, only a few points of reference data for $\tilde{\Omega}_{\text{GW}}$ exist for intermediate PTs ($\alpha = 0.05$), and so far none⁹ for strong PTs ($\alpha = 0.5$). Still, the broad agreement between the results of the Higgsless and of the scalar field-hydrodynamical simulations points towards a consistent departure from linearity in the fluid perturbations and, hence, from the sound-shell model, at least for the point at large v_w (i.e., 0.76). We note that the reference data points $\tilde{\Omega}_{\text{GW}}$ in Refs. [52, 54] are computed assuming a linear growth with the source duration as in Eq. (2.15): hence, incorporating K_{int} as in Eq. (2.23) can modify the value of $\tilde{\Omega}_{\text{GW}}$ when the source decays. Furthermore, small discrepancies with the numerical results of Ref. [52] might also be due to the different nucleation histories considered (simultaneous in Ref. [52] and exponential in our simulations).

Finally, for strong PTs, we observe even larger efficiencies overall (see the right panel of Fig. 7). In this case as well, the impact of the non-linearities washes out the dependence of $\tilde{\Omega}_{\text{GW}}$ on the wall velocity. Again, extrapolation seems to work overall, as the extrapolated values agree reasonably well for the two simulation sizes $\tilde{L}/v_w = 20$ and 40. We note that, for weak PTs, the relative difference between the extrapolated values and those obtained in our largest resolution runs with $N = 512$ is rather large. Hence, the values provided in Fig. 7 are still subject to numerical errors, related to the values of $\varepsilon_{\mathcal{I}}$ listed in Tab. 2. Indeed, we find these relative differences to be larger for weak PTs (up to 50% for extremely thin profiles, and usually below 10% otherwise), where we can compare our extrapolated results to those found within the sound-shell model, while for intermediate and strong PTs, the relative difference of our extrapolated values to the numerical results for the largest resolution $N = 512$ are below 10% for all wall velocities.

It is very important to remark that the definition of $\tilde{\Omega}_{\text{GW}}$ in terms of the integrated kinetic energy $K_{\text{int}}^2(\tilde{t}_{\text{init}}, \tilde{t}_{\text{end}})$ reduces its variation with the wall velocity and with the strength of the PT significantly — compared to normalizing it to a stationary kinetic energy ratio (e.g., to K_ξ or to K_0) multiplied by the source duration, as done previously.

⁹Reference [78] presents results of $\Omega_{\text{GW}}/\Omega_{\text{GW,exp}} = \mathcal{I}_{\text{sim}}^{\text{int}}/\mathcal{I}_{\text{exp}}^{\text{int}}$, where $\mathcal{I}_{\text{exp}}^{\text{int}}$ would correspond to the value found using Eq. (2.15) with $K = K_\xi$ and $\tilde{\Omega}_{\text{GW}} = 10^{-2}$. The ratio that ref. [78] presents therefore corresponds to a combined estimate of $\tilde{\Omega}_{\text{GW}} K_{\text{rms}}^2/K_\xi^2$ and extraction of $\tilde{\Omega}_{\text{GW}}$ for comparison is not straightforward.

This is due to the decay found in the kinetic energy that is not captured by the stationary assumption for the UETC of the sound-shell model (see discussion in Sec. 2.5 and numerical results in Sec. 4.2). Furthermore, the universality of $\tilde{\Omega}_{\text{GW}}$ is also due to the use of Eq. (2.23) instead of Q'/K^2 considered in previous work [56, 58], as discussed in Sec. 2.4.

The average of the extrapolated values of $\tilde{\Omega}_{\text{GW}}$ over v_w , for each strength α , from the simulations, are the following:

$$10^2 \tilde{\Omega}_{\text{GW}} = \begin{cases} 1.04^{+0.81}_{-0.67}, & \text{for } \alpha = 0.0046; \\ 1.64^{+0.29}_{-0.13}, & \text{for } \alpha = 0.05; \\ 3.11^{+0.25}_{-0.19}, & \text{for } \alpha = 0.5, \end{cases} \quad (4.12)$$

where the super and subscripts refer to the maximum and the minimum over v_w of the extrapolated values.¹⁰ Note that Eq. (4.12) only takes into account the variation of $\tilde{\Omega}_{\text{GW}}$ with v_w , but not from numerical inaccuracies, since it provides the extrapolated values.

As discussed in Sec. 2.3 and App. A, in principle the GW signal evaluated from the simulations corresponds to the physical one detectable today only if the source has stopped operating by the end of the simulation \tilde{t}_{end} . For weak and most of intermediate PTs, the decay of the kinetic energy is very mild, and the bulk fluid motion is still sourcing GWs at the end of the simulation: indeed, in these cases we find a linear growth rate with the source duration (see Fig. 6) and, hence, the free-propagation regime of the GW amplitude has not been reached across all wave numbers. This result is in agreement with previous simulations [40, 50, 52], and with the sound-shell model [54]. In this case, in order to provide a proxy for the GW signal today, the usual assumption in the literature is that the linear growth persists until the development of non-linearities at $\tilde{t}_* - \tilde{t}_{\text{init}} \equiv \tilde{\tau}_{\text{fin}} \sim \tilde{\tau}_{\text{sh}} \simeq \beta R_*/\sqrt{K}$ (see values in Tab. 3), and that after this time, the source is abruptly switched off [22, 85]. This leads to the linear dependence with $\tilde{\tau}_{\text{fin}}$ of Eqs. (2.15) and (2.16). For PTs where the non-linearities timescale has been reached within the duration of the simulation, i.e., strong and some intermediate PTs (see discussion in Sec. 4.2 and the right panel of Fig. 5), the decay of the kinetic energy reduces the GW sourcing during the simulation. Nevertheless, we find that, even though the GW amplitude is growing with the source duration much slower than linearly, it is still growing after $\tilde{\tau}_{\text{sh}}$, and actually until the final time of our simulations (cf. the upper panels of Fig. 6 for $\alpha = 0.05$ and 0.5). This means that, also in these cases, the simulations have not run long enough to reach the end of the GW sourcing. More importantly, this shows that the growth of the GW amplitude with the source duration persists after the development of non-linearities for an additional duration that cannot be predicted with current simulations.

Indeed, the power-law decay model of the kinetic energy $K^2(\tilde{t}) \propto \tilde{t}^{-2b}$ inferred from the simulations (see Sec. 4.2), allows us to extrapolate the resulting GW amplitude by extending K_{int}^2 to times beyond the final time of the simulation, using Eq. (2.23). According to this model, the GW amplitude Eq. (4.10) grows asymptotically for $\tilde{t} \gg \tilde{t}_*$ proportional

¹⁰Based on the parameterization of Eq. (2.16) and the results of Ref. [58], Ref. [97] reported a value $A_{\text{sw}} = 3\tilde{\Omega}_{\text{GW}} \simeq 0.11$, slightly larger than the extrapolated values in Eq. (4.12) with our updated numerical simulations and results.

to $\mathcal{I}_{\text{sim}}^{\text{int}} \sim \tilde{t}^{1-2b}$ for $b < \frac{1}{2}$, $\mathcal{I}_{\text{sim}}^{\text{int}} \sim \ln \tilde{t}$ for $b = \frac{1}{2}$, and $\mathcal{I}_{\text{sim}}^{\text{int}} \sim \tilde{t}^0$ for $b > \frac{1}{2}$ [see also Eq. (2.29)]. For the weak and intermediate PTs that are featuring slow decay, with $0 \leq b < \frac{1}{2}$, the GW amplitude keeps growing unbounded, and the linear growth predicted by the sound-shell model gets generalized to $\mathcal{I}_{\text{sim}}^{\text{int}} \sim \tilde{t}^{1-2b}$. On the other hand, as discussed below Eq. (4.10), $b > \frac{1}{2}$ for strong and some intermediate PTs: in these cases, the GW amplitude then saturates to a constant value in the limit $\tilde{t} \gg \tilde{t}_*$. We emphasize that these results seem to indicate that, after the fluid perturbations enter the non-linear regime, the GW amplitude still takes some time to saturate to its free-propagation value. Hence, the usual procedure that consists in assuming a linear growth cut at $\tilde{\tau}_{\text{fin}} = \tilde{\tau}_{\text{sh}}$ most probably underestimates the GW amplitude. For strong PTs we find that, because of the large decay of the source, the GW amplitude at the end of the simulation has almost reached its saturated value. Hence, the uncertainty on the exact saturation time has a much smaller impact on the amplitude of the GW spectrum.

These considerations hold as long as the UETC assumed in Sec. 2.4 describes the source dynamics. However, we expect that the UETC deviates from our model as vortical motion and turbulence dominates [53, 64, 71, 94]. Further analyses and simulations are necessary to fully understand this regime. In the present work, we have characterized the initial phase in which non-linearities and vortical motion start to develop for intermediate and strong PTs, during which we find that the proposed model describing the source UETC as locally stationary works well for the duration of the simulations. We therefore propose effectively stopping the GW sourcing after an appropriate choice of the source duration $\tilde{\tau}_{\text{fin}}$, which we leave as a free parameter in our current estimates.

In Fig. 8, we compare the integrated GW amplitude obtained in the simulations (also shown in the upper panel of Fig. 6) with the prediction from our locally stationary model for the UETC presented in Sec. 2.5. Furthermore, we also show the effect of the expansion of the Universe, following the model presented in Sec. 2.6. Because of this, the integrated GW amplitude is plotted as a function of conformal time, $a_*\beta\delta\eta_{\text{fin}} \equiv a_*\beta\eta_{\text{fin}} - \beta/H_*$ (we remind that $a_*\eta_* \equiv a_*\mathcal{H}_*^{-1} = H_*^{-1}$ and that $\delta\eta_{\text{fin}}$ denotes the source duration in conformal time). The analytical, integrated GW amplitude is obtained from the scaling of Eq. (2.23), leading to Eq. (4.10), adopting the power-law fit $K(\eta) = K_0(\Delta\eta/\Delta\eta_0)^{-b}$, assuming that the GW production starts at the time when the PT is completed $a_*\beta\Delta\eta_0 \simeq 10$, and using the decay rate b provided in Fig. 5 for each parameter set. This agrees extremely well with the integrated GW amplitude obtained from the simulations $\mathcal{I}_{\text{sim}}^{\text{int}}/(K_\xi^2\beta R_*)$, provided we (i) correct for the initial time of GW production from $a_*\beta\Delta\eta_0 \simeq 10$ to $a_*\beta\Delta\eta_{\text{init}} = 16$ by adding the integrated $K_{\text{int}}^2(\eta_0, \eta_{\text{init}})$ to the numerical integrated GW amplitude plotted in Fig. 8, and (ii) we use the extrapolated values K_0 presented in Sec. 4.1 to account for the corrections due to the under-resolution of the self-similar profiles. Note that we are extending the validity of the scaling of Eq. (2.23), and of the power law in Eq. (2.27), outside the regime in which they have been tested by simulations: namely, in the interval $\eta \in [\eta_0, \eta_{\text{init}}]$, and to times after the end of the simulations, $\eta \in [\eta_{\text{end}}, \eta_{\text{fin}}]$. The effect of the expansion of the Universe is accounted for according to Eq. (2.31), leading to Eq. (2.34); we further choose as examples the values $\beta/H_* = 100$ and 1000.

It is important to remark that in general GWs start to be sourced from the time of

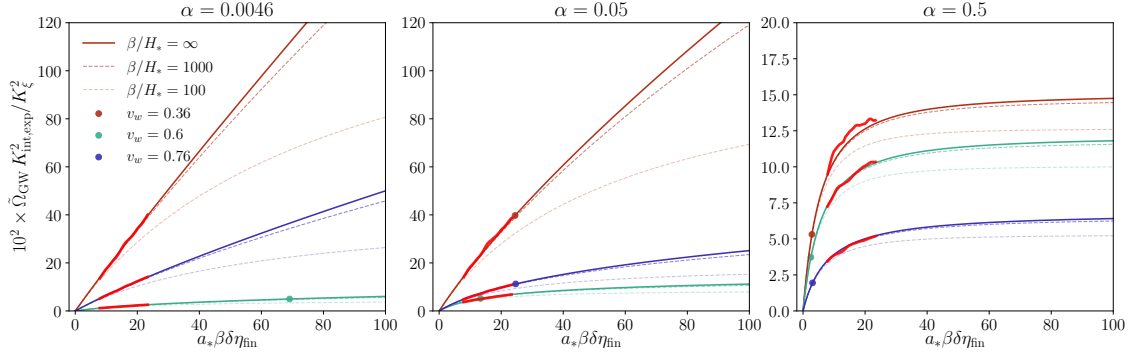


Figure 8. Dependence of the GW integrated amplitude with the conformal source duration $a_*\beta\delta\eta_{\text{fin}} = a_*\beta\eta_{\text{fin}} - a_*\beta\eta_*$, assuming that the GW production starts at $\eta_* = \eta_0$, normalized by the reference value $\tilde{\Omega}_{\text{GW}} \simeq 10^{-2}$ [52] and by $K_{\xi}^2 R_* \beta$ [cf. Eq. (4.10)], for wall velocities $v_w = 0.4, 0.56$, and 0.8 . Red segments indicate simulation results, already plotted in Figure 6 but here re-scaled by the extrapolated values of the kinetic energy fraction at \tilde{t}_0 , \mathcal{K}_0^2 , found in Sec. 4.1 (see Fig. 3), and adding the expected contribution to the GW production from the interval of time $\eta \in [\eta_0, \eta_{\text{init}}]$. We remind that in the simulations $\Delta\eta_0 \simeq 10/(\beta a_*)$ and $\Delta\eta_{\text{init}} = 16/(\beta a_*)$. Solid lines indicate the expected amplitudes extrapolated to times after the end of our simulations according to the model of Sec. 2.5, neglecting the Universe expansion ($\beta/H_* \rightarrow \infty$), while dashed lines correspond to the expected amplitudes after including expansion according to the model of Sec. 2.6, for $\beta/H_* = 1000$ and 100 in decreasing opacity. Dots indicate the shock formation time $a_*\beta\delta\eta_{\text{sh}} = \beta R_*/\sqrt{K_{\xi}}$ (see values in Tab. 3), which determines the expected scale for non-linearities to develop (they do not appear in the plot for weak PTs with $v_w = 0.4$ and 0.8).

the first bubble collision. However, in this work we are neglecting the GW production before \tilde{t}_0 , the time at which the full simulation volume is in the broken phase: this implies that the GW amplitude extrapolated from the simulations is underestimated. Indeed, by the time \tilde{t}_0 , K has already significantly decayed in strong PTs, as can be appreciated by Fig. 4. However, in the collision regime the results are expected to strongly depend on the nucleation history; furthermore, the stationary and locally stationary assumptions might not be valid, neither would be the power-law decay description of the kinetic energy evolution. The GW production near the collision regime is therefore beyond the scope of the present analysis, and deserves further study.

4.4 Gravitational wave spectral shape

In this section, we present the numerical results concerning the spectral shape for weak, intermediate, and strong transitions and a range of wall velocities. We present fits to the data and extract spectral features. Results for weak and intermediate transitions were previously obtained in hybrid simulations in Ref. [56] and Higgsless simulations in Ref. [58]. Utilizing the improved Higgsless code, we update the results of Ref. [58] and present new results for strong transitions. In addition to updating the results, we present scaling relations derived from normalizing to R_* rather than to β , evidently revealing a better scaling behavior of the knee position in the spectrum associated with the typical bubble size.

The findings in Ref. [58] indicate that the GW spectrum $\Omega_{\text{GW}}(k)$ is characterized by a double broken power law: at small k , a $\Omega_{\text{GW}}(k) \propto k^3$ scaling was observed, which is also expected from causality [64]. At large k , the spectrum decays as $\Omega_{\text{GW}}(k) \propto k^{-3}$. At intermediate scales, a linear scaling regime $\Omega_{\text{GW}}(k) \propto k$ was observed. Due to limited resolution, the spectrum appears to exponentially decay beyond a damping scale k_e as a result of numerical viscosity. At scales around or beyond the Nyquist wave number, $\Omega_{\text{GW}}(k)$ behaves erratically and is always neglected for the purpose of analysis and parameter extraction.

To capture the behavior of the spectral shape $S(\tilde{k}) \equiv \mathcal{I}_{\text{sim}}(\tilde{k})/\mathcal{I}_{\text{sim}}^{\text{int}}$, we use the following double broken power law function,

$$S(k, k_1, k_2, k_e) = S_0 \left(\frac{k}{k_1} \right)^{n_1} \left[1 + \left(\frac{k}{k_1} \right)^{a_1} \right]^{-\frac{n_1+n_2}{a_1}} \left[1 + \left(\frac{k}{k_2} \right)^{a_2} \right]^{-\frac{-n_2+n_3}{a_2}} e^{-(k/k_e)^2}, \quad (4.13)$$

which corresponds to the shape function used, e.g., in Refs. [96, 97], with an additional exponential damping factor effective above the damping scale $k > k_e$. We expect that the exponential damping found in the simulated spectra is purely due to numerical viscosity so we disregard the parts of the spectra where the exponential damping is relevant. Assuming $k_1 < k_2$ and $k < k_e$, the fitting parameters correspond to the slopes n_1 , n_2 , and n_3 , such that $S(k) \sim k^{n_1}$ at small wave numbers $k < k_1$, $S(k) \sim k^{n_2}$ at intermediate $k_1 < k < k_2$, and $S(k) \sim k^{n_3}$ at large $k > k_2$. The parameters a_1 and a_2 allow to control the sharpness/smoothness of the spectral shape around the knee and peak at k_1 and k_2 . S_0 is a normalization constant defined by the condition that $\int S d \ln k = 1$. We note that the choice $a_1 = 2$, $a_2 = 4$, $n_1 = 3$, $n_2 = 1$, and $n_3 = -3$ renders Eq. (4.13) equivalent to

$$S_f(k, k_1, k_2, k_e) = S_0 \times \frac{(k/k_1)^3}{1 + (k/k_1)^2 [1 + (k/k_2)^4]} \times e^{-(k/k_e)^2}, \quad (4.14)$$

which was previously used in Ref. [56]. Equation (4.13), however, allows for a more adaptable recovery of the GW spectrum peak position and slopes by adapting the sharpness/smoothness of the spectral shape around the knee and the peak to the one found in the numerical data.

We expect the characteristic knee and peak of the GW spectra to be determined by the scale of the fluid perturbations R_* . Another important length scale is the fluid-shell thickness [51, 54]

$$\xi_{\text{shell}} := \xi_{\text{front}} - \xi_{\text{rear}}, \quad (4.15)$$

where

$$\xi_{\text{front}} = \begin{cases} \xi_{\text{shock}}, & \text{for deflagrations and hybrids,} \\ v_w, & \text{for detonations,} \end{cases} \quad (4.16)$$

and

$$\xi_{\text{rear}} = \begin{cases} v_w, & \text{for deflagrations,} \\ c_s, & \text{for detonations and hybrids.} \end{cases} \quad (4.17)$$

The scale $R_* \xi_{\text{shell}}$ is expected to determine the peak of the GW spectrum [22, 40, 50, 52, 54, 59, 99].

Fitting to the numerical data

We fit Eq. (4.13) to our numerically computed GW spectra and thus extract spectral features from our data. We show in Fig. 9 the numerical GW spectra $\mathcal{I}_{\text{sim}}(\tilde{t}_{\text{init}}, \tilde{t}_{\text{end}}, \tilde{k})$ found in the simulations with numerical resolution $N = 512$ and box sizes $\tilde{L}/v_w = 20$ and 40, for a range of wall velocities, and for weak, intermediate, and strong PTs, together with the analytical fits. We use $\tilde{t}_{\text{init}} = 16$ and $\tilde{t}_{\text{end}} = 32$ to evaluate the GW spectra. In the fitting procedure, we impose the constraint that $k_1 < k_2$. However, since k_e does not represent a physical scale, we do not require that $k_2 < k_e$, but allow k_e to take on any value independently. In the cases where $k_2 > k_e$, the spectral peaks are not resolved properly and suffer from numerical viscosity.

In obtaining the fit, we neglect the first bin for simulations with $\tilde{L}/v_w = 20$ and the first two bins for $\tilde{L}/v_w = 40$ to avoid the associated significant statistical scatter. We cut the spectra in the UV where the fit including the exponential damping deviates from the broken power law with no exponential damping. While in Fig. 9 we show fits of Eq. (4.13) to the spectra for different v_w , in Fig. 10 we show the fitted spectral features k_1 , k_2 , and k_e as functions of v_w for weak ($\alpha = 0.0046$), intermediate ($\alpha = 0.05$), and strong ($\alpha = 0.5$) PTs. We present these characteristic wave numbers in units of $1/\beta$ and $1/R_*$ to evaluate the resulting dependence on v_w and determine the scale characterizing the spectral knee and peak. We note that the maximum value of the spectral shape used in Eq. (4.13) is located at k_{peak} , which does not in general exactly coincide with k_2 (see discussion in Ref. [97]) and their relation depends on the fitting parameters. Only when $k_2/k_1 \gg 1$, we can find the analytical relation $k_{\text{peak}} = k_2(-n_2/n_3)^{1/a_2}$. However, this separation of scales is only expected for thin fluid shells, i.e., $v_w \lesssim v_{\text{CJ}}$, and only found in our simulations for weak PTs. We show the resulting spectral peaks obtained numerically from the fit in the right columns of Fig. 10.

Extraction of the scale of exponential damping k_e gives us a handle on the reliability of the measurement of other parameters and the peak; clearly, finding $k_2 > k_e$ means we are in a regime where damping already dominates on scales larger than the peak in the spectrum. In this case, even though for weak transitions k_2 is found to track $1/\xi_{\text{shell}}$ well above $k_2 > k_e$, as can be appreciated from the middle column of Fig. 10 (which means that we are potentially recovering a trend expected from physical considerations), caution should be taken in interpreting k_2 and k_{peak} as true physical parameters. However, for intermediate and strong PTs, we do not find any evidence for k_2 to be determined by ξ_{shell} , as previously pointed out in Ref. [58]. Using our numerical results with $\tilde{L}/v_w = 20$, which present better resolution in the UV, averaged over v_w , we find the following values for k_2 ,

$$\frac{k_2 R_*}{2\pi} \simeq \begin{cases} (0.49 \pm 0.024)/\Delta_w, & \alpha = 0.0046, \\ 0.93 \pm 0.13, & \alpha = 0.05, \\ 0.45 \pm 0.042, & \alpha = 0.5, \end{cases} \quad (4.18)$$

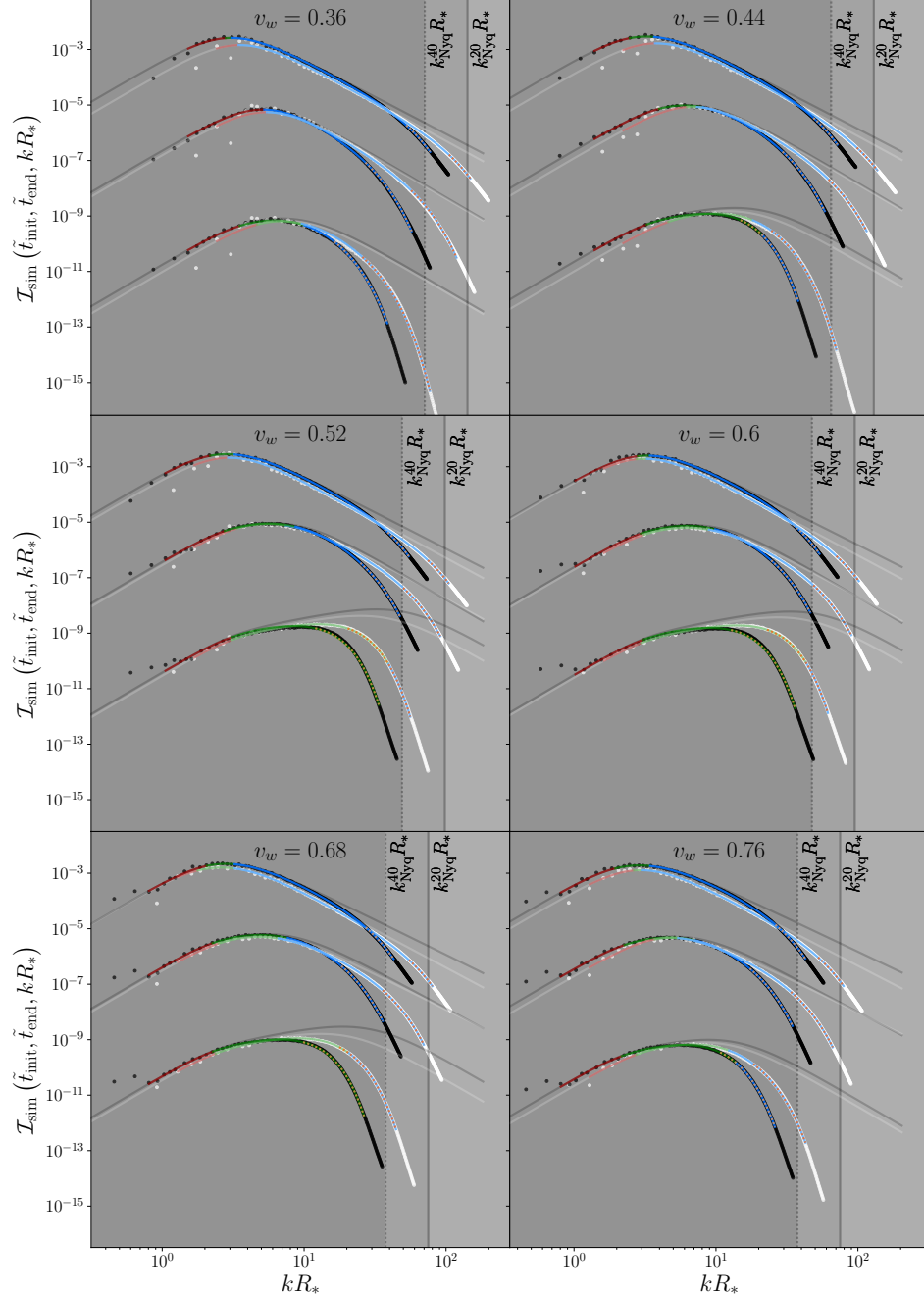


Figure 9. Fits of Eq. (4.13) to the numerical results from weak, intermediate, and strong PTs (in each plot, amplitudes increase with larger α) with $N = 512$ for a range of v_w , and for $\tilde{L}/v_w = 20$ in brighter colors (white dots for the numerical data), and $\tilde{L}/v_w = 40$ in darker colors (black dots for the numerical data). Red lines indicate wave numbers below the knee k_1 , green indicates intermediate wave numbers $k_1 < k < k_2$, and blue corresponds to wave numbers above the peak k_2 . The dotted orange lines indicate wave numbers $k > k_e$, where exponential damping dominates. The light and dark gray lines indicate the resulting fitted double broken power laws excluding the exponential damping. Vertical lines indicate the Nyquist wave numbers $k_{\text{Nyq}} R_* = \beta R_* N / \tilde{L}$.

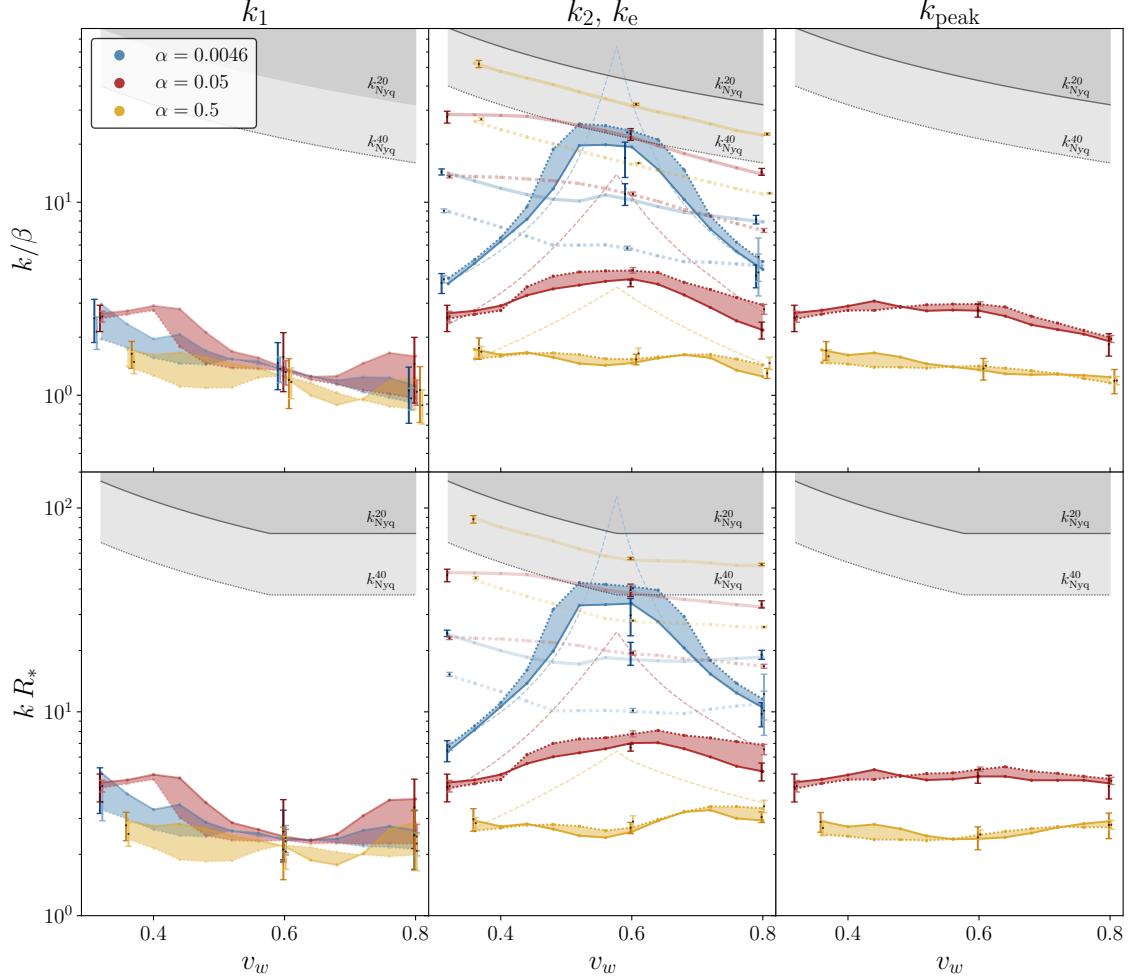


Figure 10. Fitted characteristic wave numbers k_1 (left column), k_2 and k_e (middle column), and k_{peak} (right column) for weak (blue), intermediate (red), and strong (orange) PTs, using simulations with $N = 512$ and $\tilde{L}/v_w = 20$ (40) in solid (dotted) lines. Gray regions indicate the Nyquist frequency $k_{\text{Nyq}} = N/\tilde{L}$. In the upper panel, wave numbers are normalized as $\tilde{k} \equiv k/\beta$, as presented in Ref. [56], while in the lower panel, they are normalized as $k R_*$. Thick colored lines of low opacity in middle column indicate k_e for $\tilde{L}/v_w = 20$ (40) in solid (dotted) lines. In the upper middle panel, thin color dashed lines indicate $1/\xi_{\text{shell}}$, while in the lower middle panel, they are proportional to $1/\Delta_w$ with an amplitude chosen to fit the values of $k_2 R_*$ at low v_w [see Eq. (4.18) for fitted value of weak PTs]. In the right column, the lower opacity regions indicate the peak as obtained using the double broken power-law fit of Eq. (4.13). We omit the values for weak PTs as they depend on the inclusion/exclusion of the exponential damping.

where the indicated uncertainty corresponds to the range in the measurements among the *reference* simulations, and $\Delta_w = \xi_{\text{shell}} / \max(v_w, c_s)$ is the normalized sound-shell thickness. Sample variance from the 10 nucleation histories, shown by the error bars in Fig. 10, is generally of the order of the scatter with wall velocity. On the other hand, the numerical values at the knee, expected to be related to the fluid perturbations scale R_* , are found to be

$$\frac{k_1 R_*}{2\pi} \simeq 0.39 \pm 0.1. \quad (4.19)$$

We note that both scales $k_1 R_*$ and $k_2 R_*$ (for intermediate and strong transitions) present very small variability with v_w , indicating a rather universal behavior. For weak PTs, $k_2 R_* \Delta_w$ is also almost independent of v_w , as expected from the sound-shell model. The values of $k_2 R_*$ and $k_1 R_*$ used in Ref. [97] are based on the numerical results of Ref. [58]. For weak PTs, we find $k_2 R_* \Delta_w$ consistent with the values used in Ref. [97], while we find the value of $k_1 R_*$ to be twice the one used in Ref. [97]. We note that the extraction of the knee k_1 in the IR part of our spectra is more sensitive to statistical variance, under-resolution, and the duration of our simulations.

Time evolution of the spectral shape in the simulations

We show in Fig. 11 the GW spectrum $\mathcal{I}_{\text{sim}}(\tilde{t}_{\text{init}}, \tilde{t}, \tilde{k})$ for different values of \tilde{t} of the simulation, indicating its dependence with the source duration $\tilde{\tau} = \tilde{t} - \tilde{t}_{\text{init}}$. The resulting spectral shape at the end of the simulation, $\tilde{t}_{\text{end}} = 32$, is then shown in Fig. 9 and used to provide the fits of the spectral shape presented above.

We find in general that the causal tail, proportional to k^3 at small k , is present from early times, and a more complex structure seems to develop below the peak as time advances. Although not very clear from our results, we remark that the bump feature developing in particular at high v_w is potentially consistent with analytical work [59] and numerical simulations [60]. Within the updated sound-shell model of Refs. [59, 60], this feature would correspond to the value of $k R_*$ after which the assumptions of the old sound-shell model [51, 54] are valid. This occurs around $0.1 \lesssim k_{\text{ft}} R_* \lesssim 1$ (the reasons behind the position of this feature, and a consequent more precise estimate, require further study). Depending on the duration of the GW sourcing τ_{fin} , Ref. [59] finds that this feature would be preceded either by the causal k^3 tail if $1 \lesssim \tau_{\text{fin}}/R_* \lesssim 10$, or by a linear tail if $\tau_{\text{fin}}/R_* \gtrsim 10$ (see also discussion in Sec. 2.4). It is important to point out that this linear tail has nothing to do with the linear increase between k_1 and k_2 . For the simulations, indeed, $\tau_{\text{end}} = (\tilde{t}_{\text{end}} - \tilde{t}_{\text{init}})/\beta = 16/\beta$ so that $\tau_{\text{end}}/R_* = 16/(\beta R_*) = 16/[(8\pi)^{1/3} \max(v_w, c_s)] \lesssim 10$. Therefore, the simulations results seem to be consistent with the predictions of the revised sound-shell model of Ref. [59] (at least for weak PTs), predicting a k^3 increase at low k , a feature at $0.1 \lesssim k_{\text{ft}} R_* \lesssim 1$, and a double peak structure at $k R_* \gtrsim 1$ (see Fig. 13 of Ref. [59]). If the simulation would continue for longer times and the GWs would continue to be sourced with no decay of the kinetic energy (e.g., for weak PTs), then we would expect the linear regime in k to develop in the IR tail [59].

Furthermore, we find that the growth of the GW amplitude with the source duration is faster than linear at small wave numbers and early simulation times. This is also consistent

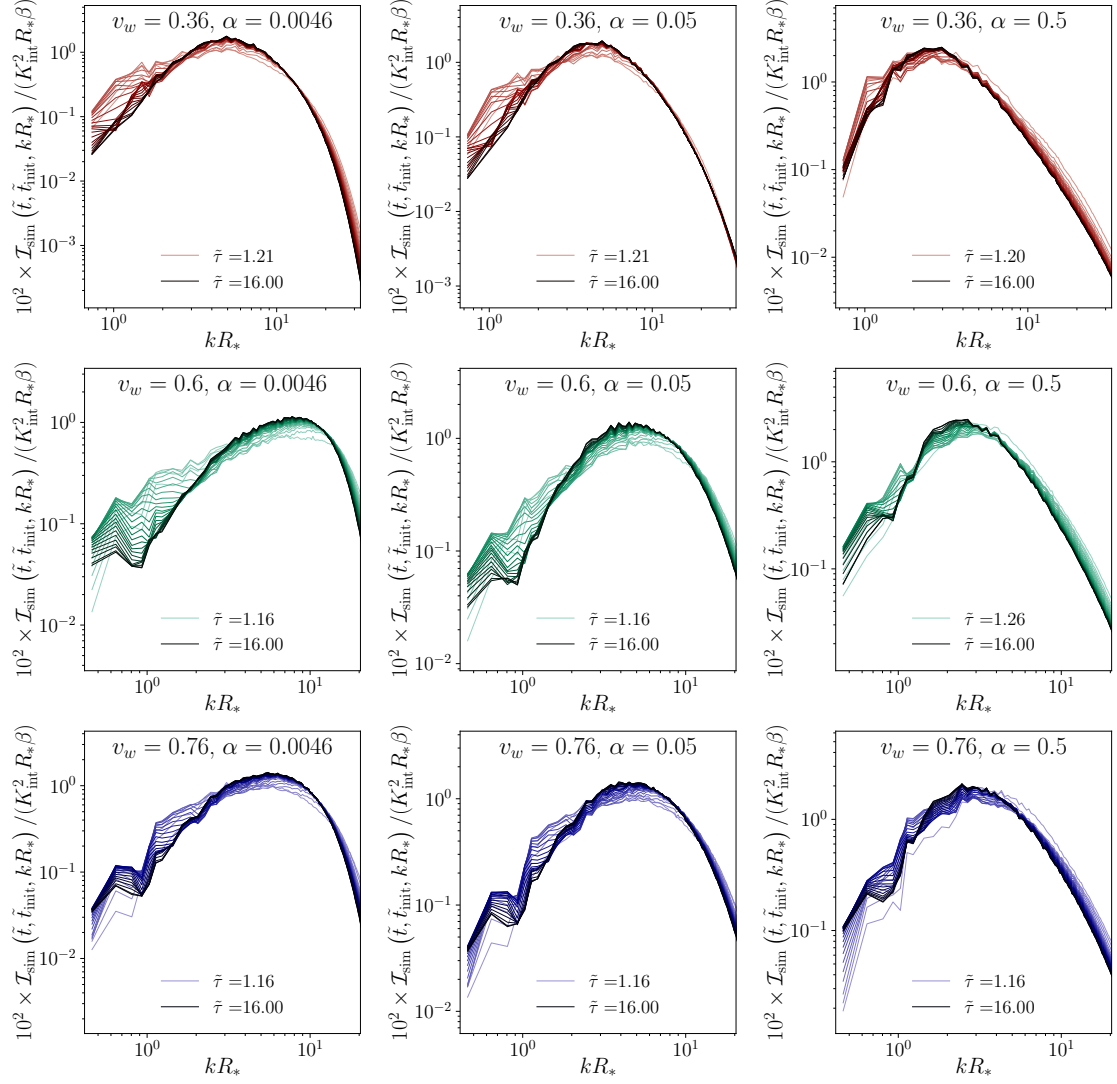


Figure 11. Time evolution of the GW spectral shape $\mathcal{I}(\tilde{t}_{\text{init}}, \tilde{t}, \tilde{k})$ evaluated at times $\tilde{t} \in [17, 32]$ with $\tilde{t}_{\text{init}} = 16$, for weak (left columns), intermediate (middle columns), and strong (right columns) PTs, for $v_w = 0.36$ (upper panel), 0.6 (middle panel), and 0.76 (lower panel). These simulation times correspond to source durations $\tilde{\tau} \equiv \tilde{t} - \tilde{t}_{\text{init}} \in [1, 16]$. The numerical resolution is $N = 512$ and the size of the simulation box is $\tilde{L}/v_w = 40$. The GW spectra are normalized by the reference value $\tilde{\Omega}_{\text{GW}} \simeq 10^{-2}$ and the expected scaling $K_{\text{int}}^2 R_* \beta$ as in Fig. 6 [see Eq. (2.23)].

with the predictions of Ref. [59], which, when no significant decay of K occurs, finds a quadratic growth with the source duration (i.e., with \tilde{t} in the present case), that transitions to a linear growth at later times the smaller is k . As discussed in Sec. 2.5, the modeling presented and validated for the integrated GW spectrum, based on the assumptions of a locally stationary UETC and its small compact support, is only expected to hold at wave numbers $kR_* \gg \beta R_*/(\tilde{t} - \tilde{t}_{\text{init}})$. Then, using the GW spectral shape as measured at \tilde{t}_{end} as the one that ultimately enters the proposed model in Eq. (2.23), effectively implies the assumption that all wave numbers evolve with the source duration in the same way

as the overall amplitude, until $\tilde{t}_{\text{fin}} > \tilde{t}_{\text{end}}$ is reached. However, different time evolutions than those validated for the integrated amplitude, even if occurring at wave numbers that do not significantly contribute to the integrated amplitude and/or at times after the end of the simulation, could still potentially affect the resulting spectral shape of the GW spectrum. This can occur within the sound-shell model in the IR regime, as shown in Ref. [59], where a transition from the linear towards a quadratic growth with the source duration is expected at small k in the stationary case. Moreover, modifications can also occur as the assumption of a stationary (or its extension to locally stationary in Sec. 2.5 to include decaying sources) UETC is no longer valid due to, for example, the potential development of non-linear fluid perturbations and vortical motion. In the latter case, the resulting GW spectrum is expected to have a different time evolution than the one for compressional motion [55, 62, 63, 65, 70, 71] and we expect that the GW modes would reach their saturation amplitudes in this regime. Finally, we note that this spectral shape is computed in flat Minkowski space-time; accounting for the expansion of the Universe could modify it, for source durations comparable or longer than the Hubble time. However, based on the results of Ref. [59], we expect the modifications to occur in the IR tail.

GW spectral slopes

In general, we find a clear $n_1 = 3$ slope at the smallest frequencies of our simulations, consistent with the expected causal tail, $S(k) \sim k^3$ [59, 64]. At intermediate wave numbers, we fix $n_2 = 1$, although this range of k is not large enough to have a clear prediction of the exact intermediate slope. As already mentioned, this intermediate slope bears no relation with the linear increase found in the IR tail in Ref. [59] that could appear at later times if the system remains in the linear regime (as argued above). However, it is clear that a smoothing with respect to the k^3 occurs in this range that eventually leads to the decrease k^{n_3} with $n_3 < 0$ at large wave numbers $k > k_2$. In this regime, the sound-shell model predicts a slope $n_3 = -3$ [40, 50–52, 56, 58–60], and our simulations show a clear $n_3 \approx -3$ whenever $k_2 \ll k_e$. However, we allow n_3 to be a parameter in our fits, since deviations might occur, potentially due to the development of non-linearities. From Fig. 9 it is apparent that, for strong PTs, the simulations offer sufficient dynamical range to sample the UV slope of the GW spectrum. This is particularly interesting, since for strong PTs, we expect a departure from $n_3 = -3$ if non-linearities lead to a cascade of energy into the UV, thus modifying the slope towards a Kolmogorov turbulence spectrum with $n_3 = -8/3$ [53, 55, 62, 63, 65, 71, 103], or a shallower acoustic turbulence spectrum [61, 104]. Hence, we allow $n_3 \geq -3$ when deriving the fit for strong and intermediate PTs, while we fix $n_3 = -3$ for weak PTs, since the dynamical depth is typically insufficient to recover the UV behavior in these cases. Indeed, for weak PTs, k_2 is determined by the sound-shell thickness [see Eq. (4.18)], leading to $k_2 \gtrsim k_e$ in general.

In Fig. 12, we plot the fitted values of n_3 . For intermediate transitions, we observe a marginal increase in n_3 towards -2.5 as the wall velocity is increased. Strong transitions exhibit a similar trend, while also preferring an optimal $n_3 \lesssim -2.75$ for small v_w .

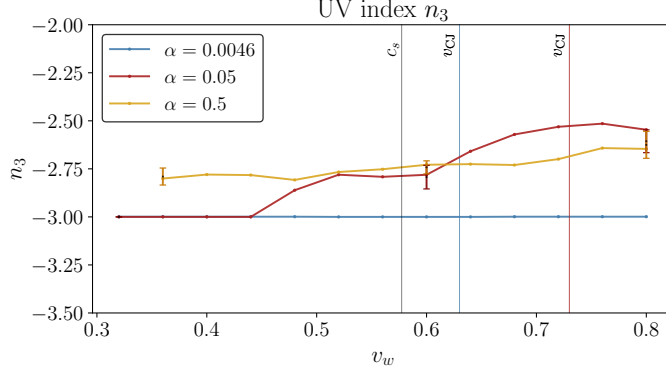


Figure 12. Fitted UV index $n_3 \geq -3$ for the spectral shape of weak (blue), intermediate (red), and strong (orange) PTs, found for simulations with $N = 512$ and $\tilde{L}/v_w = 20$. We note that $n_3 = -3$ is fixed for weak PTs. The error bars show the standard deviation from 10 different bubble nucleation histories. The black vertical line indicates the sound speed c_s , while colored lines indicate the Chapman-Jouguet v_{CJ} for weak and intermediate PTs ($v_{CJ} \simeq 0.89$ for strong PTs is out of the plot).

Smoothing/sharpening of the knees

Introducing two new free parameters a_1 and a_2 obviously improves the fits to the numerical data, compared to using the simpler Eq. (4.14) [56, 58]. Since the peak of the GW spectrum k_{peak} is of greatest phenomenological interest, we adjust the parameters a_1 and a_2 to constants that universally recover the peak position well for all wall velocities and strengths. Empirically, we find that a slight sharpening of the knee and a slight smoothing of the peak typically improve the peak position recovery and yield good results for the fit overall. Measurements of a_1 benefit from simulations with more data points in the IR, and we use exclusively simulations with $\tilde{L}/v_w = 40$ for its estimation, whereby $a_1 = 3.6$ (i.e., an increase from $a_1 = 2$ as used in Refs. [56, 58]) is found suitable. Measurements of a_2 , on the other hand, benefit from resolving the UV, for which we use exclusively simulations with $\tilde{L}/v_w = 20$, and find that $a_2 = 2.4$ (i.e., a reduction from $a_2 = 4$ as used in Refs. [56, 58]) is an adequate choice. We use these values for a_1 and a_2 throughout this study, but point out that in principle, the spectral fit could be improved by varying these parameters at the cost of a larger scatter in the parameter extraction (due to degeneracies). The parameters k_1 , k_2 , k_e , and k_{peak} shown in Fig. 10 have been obtained using the aforementioned values of a_1 and a_2 . In the different rows, these parameters are expressed in terms of the physical length scales discussed in the last section.

5 Summary and conclusions

We have conducted numerical simulations of cosmological first-order phase transitions (PTs) using the Higgsless approach [58] to compute the fluid perturbations in the primordial plasma induced by a PT and the resulting GW spectra, for PT strengths $\alpha = 0.0046$ (weak), 0.05 (intermediate), and 0.5 (strong); and a broad range of wall velocities $v_w \in (0.32, 0.8)$.

These results extend the previous numerical results of Ref. [58] to strong PTs, and include a larger number of numerical simulations for weak and intermediate PTs.

We present for the first time results of the GW amplitude and spectral shape sourced by fluid perturbations from strong PTs with $\alpha = 0.5$. We have slightly updated the numerical code, although with no significant impact on the numerical results. We have compared the results of our simulations to those obtained assuming a stationary unequal time correlator (UETC) for the GW source, an assumption usually made in analytical computations of compressional motion (e.g., sound waves in the limit of linear perturbations) based on the hypothesis that the GWs are produced by a stationary superposition of sound waves. This assumption is also commonly used to extrapolate/interpret the results of numerical simulations. We confirm that the stationary UETC assumption well describes the results of our simulations of weak PTs. However, this assumption only holds if the kinetic energy fraction K is constant in time, while we find strong numerical evidence for the decay of K with time for intermediate PTs with highly confined profiles, and for strong PTs. We also find a clear deviation with respect to the linear dependence of the GW amplitude with the source duration, found in previous analytical studies based on the stationary UETC, and commonly assumed in the GW templates used in the literature. We associate this deviation to the numerically found decay of the kinetic energy fraction K . Consequently, we propose a novel model to account for this decay, namely, we extend the stationary UETC model to a locally stationary UETC.

The numerical results presented in this work have allowed us to test the validity of the locally stationary UETC model when non-linearities develop in the system. In particular, we were able to find numerically the relevant scales that enter in the resulting GW amplitude and spectral shape; see Eq. (2.23). One important difference with the stationary UETC model is that the linear dependence with the source duration τ_{fin} [see Eq. (2.16)] is substituted with an integral in time of the squared kinetic energy fraction [see Eq. (2.24)]. We have tested the model prediction for the dependence of the GW energy density with the source duration with simulations. In the case of weak PTs, we have confirmed that the GW energy density depends linearly on the source duration. Within the sound-shell model, this is then assumed to coincide with the time of development of non-linearities, τ_{sh} . On the other hand, we have shown that, for strong and some intermediate PTs, the GW production does not stop at the time when non-linearities develop, but it keeps increasing within the simulations, following the integrated K^2 . We expect that the observed increase after non-linearities develop is universal and would also affect the GW amplitude of weak and some intermediate PTs for which non-linearities occur at times after the end of our simulations. At later times, we expect the GW amplitude to saturate. As the ultimate saturation stage is not present in our simulations, we present our results as a function of the GW source duration, treating it as a free parameter. However, for strong and some intermediate PTs, we also find that the decay rate b of the kinetic energy squared becomes larger than $1/2$ (see Fig. 5), leading to a converged value of the GW amplitude in the limit of long duration. Hence, in these cases, the dependence of the GW amplitude with the source duration is weaker and the error due to a possible wrong choice for the source duration is significantly reduced (see Fig. 8). In any case, it remains in general of

paramount importance to determine the exact value of the resulting saturated GW amplitude to further improve the accuracy of the predicted GW spectra expected from weak to strong first-order phase transitions. The modeling of the remaining stage, until saturation is reached, will also require numerical simulations as it is deep in the non-linear regime and potentially dominated by vortical turbulence.

In the following, we summarize our numerical results by providing a template that can be used by the community to estimate the GW amplitude from first-order phase transitions, validated for the duration of our simulations and extrapolated to later times, taking into account that some of the values presented might be sensitive to numerical uncertainty. The resulting template will be publicly available via [CosmoGW](#) [84]. It extends (and includes, when appropriate) previous templates based on the stationary UETC assumption of the sound-shell model, which correctly describes the stage of GW sourcing dominated by linear fluid perturbations. Based on the model presented in Sec. 2.5 and validated with our numerical simulations in Sec. 4.3, we find the following parameterization of the GW spectrum when the Universe expansion can be ignored

$$\Omega_{\text{GW}}(k) = 3 \mathcal{T}_{\text{GW}} \tilde{\Omega}_{\text{GW}} (H_*/\beta) K_{\text{int}}^2 H_* R_* S(k R_*), \quad (5.1)$$

where $S(k)$ denotes the shape function of the spectrum that is normalized to $\int d \ln k S(k) = 1$, and K_{int}^2 is the integrated kinetic energy fraction K^2 over $\tilde{t} \equiv t\beta$, such that $(H_*/\beta) K_{\text{int}}^2$ reduces to $K^2 H_* \tau_{\text{fin}}$ when K is constant, being τ_{fin} the GW source duration. Therefore, Eq. (5.1) is a generalization of the parameterization used in the stationary UETC assumption previously tested with numerical simulations [40, 50, 52] and usually assumed for sound-wave sourcing of GWs [22, 51, 54, 59, 85, 96, 97] that predicts a linear dependence with the GW source duration when K does not decay with time.

Our most robust result to prove the validity of Eq. (5.1) is the almost independent value of $\tilde{\Omega}_{\text{GW}}$ with the PT parameters. This is obtained when the typical bubble separation R_* , which determines the length scale of fluid perturbations, is given by the front of the expanding bubbles [22]

$$R_* \beta = (8\pi)^{1/3} \max(v_w, c_s), \quad (5.2)$$

where β^{-1} parameterizes the duration of the PT, v_w is the wall velocity, and c_s the speed of sound. This way, the residual dependence on the wall velocity in $\tilde{\Omega}_{\text{GW}}$ is quite limited and we estimate from our numerical simulations values for the GW efficiency $\tilde{\Omega}_{\text{GW}} \sim \mathcal{O}(10^{-2})$ for a range of PTs [see Fig. 7 and Eq. (4.12)],

$$10^2 \tilde{\Omega}_{\text{GW}} = \begin{cases} 1.04_{-0.67}^{+0.81}, & \text{for } \alpha = 0.0046; \\ 1.64_{-0.13}^{+0.29}, & \text{for } \alpha = 0.05; \\ 3.11_{-0.19}^{+0.25}, & \text{for } \alpha = 0.5, \end{cases} \quad (5.3)$$

consistent with previous numerical simulations [40, 50, 52] for weak and intermediate PTs, and with the sound-shell model [51, 54] for weak PTs. For intermediate and strong PTs, we find larger efficiencies and much less dependence with v_w than for weak PTs, clearly showing a departure with respect to the predictions of the sound-shell model (see Fig. 7).

We also provide an estimate of the relevant kinetic energy fraction \mathcal{K}_0 at the end of the PT using our numerical results [see Fig. 3 and Eq. (4.6)], given in units of the single-bubble K_ξ [see Eq. (2.19) and values in Tab. 3], which, averaged over wall velocities, becomes

$$\mathcal{K}_0 = 0.84_{-0.29}^{+0.24} K_\xi. \quad (5.4)$$

As a function of v_w , we generally find that K_ξ might slightly underestimate \mathcal{K}_0 for the smallest v_w , while it tends to overestimate it for larger v_w (see Fig. 3). This might be a consequence of the energy transfer between thermal and kinetic energies during the phase of collisions and the expected development of the sound-wave regime [51, 54, 59].

We have studied the decay of the kinetic energy fraction K with time t in Sec. 4.2, and provide a power-law fit $K(t > t_0) = K_0(t/t_0)^{-b}$, with $b \geq 0$ indicating the decay rate, that accurately reproduces the numerical results (see Figs. 4 and 5). For small or vanishing values of b , one can directly use

$$K_{\text{int}}^2(b=0) \rightarrow \mathcal{K}_0^2 \beta \tau_{\text{fin}} \rightarrow \mathcal{K}_0^{3/2} \beta R_* \quad (5.5)$$

in Eq. (5.1), assuming that the duration of the GW sourcing is given by the shock formation time $\beta \tau_{\text{fin}} \sim \beta \tau_{\text{sh}} = \beta R_*/\sqrt{K}$, when non-linearities are expected to develop. In general, we find $b \ll 1$ when the shock time is larger than our final simulation time $\beta \tau_{\text{sh}} \gg \beta t_{\text{end}} = 32$ (as it is the case for weak PTs and some intermediate ones, see values in Tab. 3). In these cases, the transition towards non-linearities is not explored in our simulations and, to improve the accuracy of the saturated GW amplitude, simulations covering the possible development of the non-linear regime are required in the future.

For non-negligible values of b , we find that the decay of K occurs within the duration of our simulations, potentially indicating that we are already modeling the GW production in the non-linear regime. We indeed find that this might be the case as the shock formation time is included in the duration of our simulations for some intermediate PTs and for strong ones, where we find larger values of b . For these PTs, we find that the integrated K_{int}^2 becomes

$$K_{\text{int}}^2(b, \tau_{\text{fin}}) \rightarrow \mathcal{K}_0^2 \beta \Delta t_* \frac{(1 + \tau_{\text{fin}}/\Delta t_*)^{1-2b} - 1}{1 - 2b}, \quad (5.6)$$

when one uses the power-law fit for $K(t)$ and assumes that the GW production roughly starts at the time $\beta \Delta t_* \simeq \beta \Delta t_0 \simeq 10$ (note that the actual value of $\beta \Delta t_0$ only appears as a consequence of our particular fit; see discussion in Sec. 2.5). It is unclear what should be the final time of GW sourcing in these cases, as the simulations seem to already be modeling the non-linear regime, so we leave τ_{fin} as a free parameter. We note that this is an indication that the GW spectrum keeps growing proportional to Eq. (5.6) once non-linearities develop in the fluid, such that the use of Eq. (5.5) would in general underestimate the GW production. We expect this additional growth to also occur for weak PTs for which non-linearities are expected to occur at times not covered in our simulations. We compare in Fig. 8 the numerical dependence of the GW amplitude with the source duration $\tilde{\tau}_{\text{fin}} \equiv \beta \tau_{\text{fin}}$ found in the simulations to the one obtained using Eq. (5.6), extending the analytical fit beyond the time when the simulations end. As mentioned above, as the decay rate increases

(and it is larger than $1/2$), the GW amplitude saturates, alleviating its dependence with the source duration. Therefore, we expect that for strong PTs, the GW amplitudes obtained at the end of our simulations are close to the saturated ones.

As a final remark on the integrated GW amplitude, we note that so far the Universe expansion has been ignored, which is not justified for long source durations. Taking into account that the fluid equations are conformally invariant if the fluid is radiation-dominated [42, 90], our simulations in Minkowski space-time would correctly model the fluid evolution after the end of the PT at $\tilde{t} > \tilde{t}_0 \simeq 10$ (see Sec. 3 for more details on our numerical setup). The simulations would also correctly model the PT at $\tilde{t} < \tilde{t}_0$ as long as its duration, measured from the time at which the first bubble nucleates at $\tilde{t}_n = 0.5$, is short ($\beta/H_* \gg 10$). However, the GW production is not conformally invariant: therefore, modifications in the GW spectrum are expected, with respect to the one obtained by numerical simulations (see discussion in Sec. 2.6). As a proxy to estimate the effect of the Universe expansion on the GW spectrum amplitude, we can use the following value for K_{int}^2 [see Eqs. (2.34) and (2.37)]

$$K_{\text{int,exp}}^2 \rightarrow \mathcal{K}_0^2 \Upsilon_b(\mathcal{H}_* \delta\eta_{\text{fin}}), \quad (5.7)$$

which generalizes the suppression factor $\Upsilon = \mathcal{H}_* \delta\eta_{\text{fin}} / (1 + \mathcal{H}_* \delta\eta_{\text{fin}})$ when the source does not decay [93, 96] to any decay rate b using Eqs. (2.34)–(2.36) for the power-law fit of $K(\eta)$, for which we have fixed $\Delta\tilde{\eta}_* = \Delta\tilde{\eta}_0 \simeq 10 H_*/\beta$ to compute \mathcal{K}_0 and b in the simulations. Then, the GW spectrum becomes [see Eq. (2.37)]

$$\Omega_{\text{GW,exp}}(k) = 3 \mathcal{T}_{\text{GW}} \tilde{\Omega}_{\text{GW}} K_{\text{int,exp}}^2 \mathcal{H}_* \mathcal{R}_* S_{\text{exp}}(k_c \mathcal{R}_*). \quad (5.8)$$

We also compare in Fig. 8 the expected evolution of the integrated GW amplitude with the source duration according to Eq. (5.8) for $\beta/H_* = 100$ and 1000. We note that when one associates $\delta\eta_{\text{fin}}$ to the shock time $\delta\eta_{\text{sh}} = \mathcal{R}_*/\sqrt{K}$, they should correspond to conformal time intervals, instead of cosmic time, due to the conformal invariance of the fluid equations.

Regarding the spectral shape $S(kR_*)$ in Eq. (5.1), we find that the following template fits accurately the numerical results (see Sec. 4.4),

$$S(k, k_1, k_2) = S_0 \times \left(\frac{k}{k_1}\right)^{n_1} \left[1 + \left(\frac{k}{k_1}\right)^{a_1}\right]^{\frac{-n_1+n_2}{a_1}} \left[1 + \left(\frac{k}{k_2}\right)^{a_2}\right]^{\frac{-n_2+n_3}{a_2}}, \quad (5.9)$$

with $n_1 \simeq 3$, $n_2 \simeq 1$, $a_1 \simeq 3.6$, and $a_2 \simeq 2.4$. To compare with the numerical results we have included an exponential damping $e^{-(k/k_e)^2}$ in Sec. 4.4 [see Eq. (4.13)], effective at $k > k_e$, but we omit it here as we expect it to correspond to numerical viscosity and not have physical relevance. The slope of the UV tail is $n_3 \simeq -3$ for weak PTs, and intermediate ones with small wall velocities $v_w \lesssim c_s$. The slope becomes slightly shallower (up to -2.5) for intermediate PTs with supersonic v_w and strong PTs (see Fig. 12). This effect should not play a major role in phenomenological studies, but a more detailed description is given in Sec. 4.4. Furthermore, this shallower GW spectral slope, together with the decay of the kinetic energy, would be consistent with the presence of a forward energy cascade, and therefore indicate the development of non-linearities. To confirm this statement would require a detailed study of the kinetic spectrum properties. For now, we present a

preliminary study of the vorticity production in our simulations in App. C. Note that the spectral shape in Eq. (5.9), fitted from the simulations, might be different from the one of the GW spectrum today. For example, when the fluid perturbations are still linear at the end of our simulations (e.g., for weak PTs), further sourcing of GWs would be expected, and this would change their spectral shape, mainly in the IR tail (see, e.g., Ref. [59] and the discussion in Sec. 4.4). Furthermore, the expansion of the Universe would also lead to changes in the spectral shape (see Ref. [59] and discussion in Sec. 2.6). In this work, we only provide a fit for the spectral shape derived from the simulations in flat space-time $S(k)$, and defer an evaluation of $S_{\text{exp}}(k_c \mathcal{R}_*)$ of Eq. (5.8) to a future study.

The most relevant feature of the spectrum is the position of the peak, determined by k_2 . In this regard, we find a distinction between weak and intermediate/strong PTs (as already previously seen in Ref. [58]). For weak PTs, the peak follows the thickness of the fluid shells, ξ_{shell} , as given in Eq. (4.15), while for intermediate and strong PTs the dependence on the wall velocity is much weaker. As shown in Eq. (4.18) and Fig. 10, we find the following results for k_2 , averaged over all wave numbers and 10 different nucleation histories: $k_2 R_* \simeq \pi/\Delta_w$ for weak PTs, $k_2 R_* \simeq 2\pi$ for intermediate PTs, and $k_2 R_* \simeq \pi$ for strong ones, where $\Delta_w = \xi_{\text{shell}}/\max(v_w, c_s)$ is the normalized sound-shell thickness, which is only found to enter in k_2 for weak PTs. Finally, the position of the knee that relates to the typical size of the bubbles does not even depend on the strength of the PT and, quite generally, we find $k_1 R_* \simeq 0.4 \times 2\pi$ (see Eq. (4.19) and Fig. 10).

Acknowledgments

This research was supported in part through the Maxwell computational resources operated at Deutsches Elektronen-Synchrotron DESY, Hamburg, Germany. TK and IS acknowledge support by the Deutsche Forschungsgemeinschaft (DFG, German Research Foundation) under Germany’s Excellence Strategy – EXC 2121 “Quantum Universe” - 390833306. HR is supported by the Deutsche Forschungsgemeinschaft under Germany’s Excellence Strategy EXC 2094 ‘ORIGINS’. (No.390783311). IS acknowledges support by the Generalitat Valenciana through the Programa Prometeo for Excellence Groups, grant CIPROM/2022/69 “Sabor y origen de la materia.” ARP acknowledges support by the Swiss National Science Foundation (SNSF Ambizione grant 182044). ARP and CC acknowledge the working space provided during the program on the “Generation, evolution, and observations of cosmological magnetic fields” at the Bernoulli Center in Lausanne. ARP and IS acknowledge the hospitality of the Centro de Ciencias de Benasque Pedro Pascual during “The Dawn of Gravitational Wave Cosmology” conference. CC was supported by the Swiss National Science Foundation (SNSF Project Funding grant 212125) during the development of this project. RJ is supported by JSPS KAKENHI Grant Numbers 23K17687, 23K19048, and 24K07013.

A Computation of the gravitational wave production in simulations

The tensor-mode perturbation h_{ij} enters in the metric line element as

$$ds^2 = a^2[-d\eta^2 + (\delta_{ij} + h_{ij}) dx^i dx^j]. \quad (\text{A.1})$$

To conform with simulations, we neglect the expansion of the Universe during the time of the GW generation, which is in general justified when the sourcing duration, $\tau_{\text{fin}} = t_{\text{fin}} - t_*$, is shorter than the Hubble time H_*^{-1} . In the following, time is therefore denoted by t . The solution of the GW equation while the source is active, $t < t_{\text{fin}}$, is [17]

$$h_{ij}(t < t_{\text{fin}}, \mathbf{k}) = \frac{6H_*^2}{k} \int_{t_*}^t \Pi_{ij}(t', \mathbf{k}) \sin k(t - t') dt', \quad (\text{A.2})$$

where t_* is the initial time at which the tensor anisotropic stresses, $\Pi_{ij} = \Lambda_{ijlm} T_{lm} / \bar{\rho}$, start to source GWs, being $\bar{\rho} = 3H^2 M_{\text{Pl}}^2$ the critical energy density and $\Lambda_{ijlm} = P_{il} P_{jm} - \frac{1}{2} P_{ij} P_{lm}$ the traceless and transverse projector, with $P_{ij} = \delta_{ij} - \hat{k}_i \hat{k}_j$. M_{Pl} is the reduced Planck mass, $M_{\text{Pl}} = (8\pi G)^{-1/2} \simeq 2.4 \times 10^{18}$ GeV.

The final time of GW sourcing t_{fin} is the time at which the source stops operating. After the sourcing has ended, the solution is

$$h_{ij}(t \geq t_{\text{fin}}, \mathbf{k}) = \frac{6H_*^2}{k} \int_{t_*}^{t_{\text{fin}}} \Pi_{ij}(t', \mathbf{k}) \sin k(t - t') dt', \quad (\text{A.3})$$

such that all GW modes propagate as free plane waves, with an amplitude that is determined by the sourcing process.

From Eq. (A.3), the time derivatives of the strains h_{ij} are

$$\partial_t h_{ij}(t \geq t_{\text{fin}}, \mathbf{k}) = 6H_*^2 \int_{t_*}^{t_{\text{fin}}} \Pi_{ij}(t', \mathbf{k}) \cos k(t - t') dt', \quad (\text{A.4})$$

which can be used to find the fractional energy density at present time t_0 [17],

$$\Omega_{\text{GW}}(t_0) = \frac{\rho_{\text{GW}}}{\rho_{\text{tot}}^0} = \frac{(a_*/a_0)^4}{12H_0^2} \langle \partial_t h_{ij}(t_0, \mathbf{x}) \partial_t h_{ij}(t_0, \mathbf{x}) \rangle. \quad (\text{A.5})$$

We consider the GW spectrum $\Omega_{\text{GW}}(t_0, k) \equiv d\Omega_{\text{GW}}(t_0)/d \ln k$, which describes the two-point correlation function of the statistically homogeneous and isotropic strain derivatives, following the notation of Ref. [66],

$$\frac{(a_*/a_0)^4}{12H_0^2} \langle \partial_t h_{ij}(t_0, \mathbf{k}) \partial_t h_{ij}^*(t_0, \mathbf{k}') \rangle = (2\pi)^6 \delta^3(\mathbf{k} - \mathbf{k}') \frac{\Omega_{\text{GW}}(t_0, k)}{4\pi k^3}, \quad (\text{A.6})$$

such that $\Omega_{\text{GW}}(t_0) = \int \Omega_{\text{GW}}(t_0, k) d \ln k$. Substituting Eq. (A.4) into Eq. (A.6), we find

$$\Omega_{\text{GW}}(t_0, k) = 3k \mathcal{T}_{\text{GW}} H_*^2 \int_{t_*}^{t_{\text{fin}}} \int_{t_*}^{t_{\text{fin}}} E_{\Pi}(t_1, t_2, k) \cos k(t_0 - t_1) \cos k(t_0 - t_2) dt_1 dt_2, \quad (\text{A.7})$$

where

$$\mathcal{T}_{\text{GW}} \equiv \left(\frac{a_*}{a_0} \right)^4 \left(\frac{H_*}{H_0} \right)^2 \simeq 1.6 \times 10^{-5} \left(\frac{g_*}{100} \right)^{-1/3}, \quad (\text{A.8})$$

is the transfer function, with

$$\frac{a_*}{a_0} \simeq 8 \times 10^{-16} \frac{100 \text{ GeV}}{T_*} \left(\frac{g_{*s}}{100} \right)^{-1/3}, \quad (\text{A.9})$$

being the ratio of scale factors, and g_* and g_{*s} denote respectively the relativistic and entropic degrees of freedom at the time of GW production. $E_\Pi(t_1, t_2, k)$ is the unequal-time correlator (UETC) of the anisotropic stresses,

$$\langle \Pi_{ij}(t_1, \mathbf{k}) \Pi_{ij}^*(t_2, \mathbf{k}') \rangle = (2\pi)^6 \delta^3(\mathbf{k} - \mathbf{k}') \frac{E_\Pi(t_1, t_2, k)}{4\pi k^2}. \quad (\text{A.10})$$

At present time, for modes $kt_0 \gg 1$, we can average the product of Green's functions in Eq. (A.7) over oscillations to find

$$\Omega_{\text{GW}}(k) = \frac{3k}{2} \mathcal{T}_{\text{GW}} H_*^2 \int_{t_*}^{t_{\text{fin}}} \int_{t_*}^{t_{\text{fin}}} E_\Pi(t_1, t_2, k) \cos k(t_1 - t_2) dt_1 dt_2. \quad (\text{A.11})$$

Therefore, once we know the UETC of the source of GWs, $E_\Pi(t_1, t_2, k)$, we can directly compute the GW spectrum. In the present scenario, the GW source corresponds to the fluid perturbations $\Pi_{ij} = w\gamma^2 \Lambda_{ijlm} v_l v_m / \bar{\rho}$, modeled through the simulations. Within a simulation, the UETC can be computed by approximating the ensemble average of the anisotropic stresses in Eq. (A.10) with the average over spherical shells of radius k in Fourier space,

$$E_\Pi(t_1, t_2, k) = \frac{k^2}{2\pi^2 V} \int_{\Omega_k} \frac{d\Omega_k}{4\pi} \Pi_{ij}(t_1, \mathbf{k}) \Pi_{ij}^*(t_2, \mathbf{k}). \quad (\text{A.12})$$

Then, substituting Eq. (A.12) into Eq. (A.11) and writing $\cos k(t_1 - t_2) = \cos kt_1 \cos kt_2 + \sin kt_1 \sin kt_2$, the double integral over t_1 and t_2 can be expressed as the following product:

$$\begin{aligned} \Omega_{\text{GW}}(k) = \frac{3k^3}{4\pi^2 V} \mathcal{T}_{\text{GW}} H_*^2 \int_{\Omega_k} \frac{d\Omega_k}{4\pi} \int_{t_*}^{t_{\text{fin}}} \Pi_{ij}(t_1, \mathbf{k}) e^{ikt_1} dt_1 \\ \times \int_{t_*}^{t_{\text{fin}}} \Pi_{ij}^*(t_2, \mathbf{k}) e^{-ikt_2} dt_2, \end{aligned} \quad (\text{A.13})$$

where we have used the fact that the resulting $\Omega_{\text{GW}}(k)$ is real. Finally, defining the following integral over the stress-energy tensor $T_{ij} = w\gamma^2 v_i v_j$,

$$T_{ij}(q, \mathbf{k}, t_*, t_{\text{fin}}) = \int_{t_*}^{t_{\text{fin}}} T_{ij}(t, \mathbf{k}) e^{iqt} dt, \quad (\text{A.14})$$

and using the property $\Pi_{ij}\Pi_{ij}^* = \Lambda_{ijlm} T_{ij} T_{lm}^* / \bar{\rho}^2$, we find the following expression

$$\Omega_{\text{GW}}(k) = \frac{3k^3}{4\pi^2 V \bar{\rho}^2} \mathcal{T}_{\text{GW}} H_*^2 \int_{\Omega_k} \frac{d\Omega_k}{4\pi} \Lambda_{ijlm}(\hat{\mathbf{k}}) [T_{ij}(q, \mathbf{k}) T_{lm}^*(q, \mathbf{k})]_{q=k}. \quad (\text{A.15})$$

This is the expression that is implemented in the Higgsless simulations to evaluate the GW spectrum: it has been previously used in Refs. [56, 58], where it is referred to as Weinberg's formula, due to its similarity with the expression obtained for the power emitted by isolated

deterministic binaries [105]. Each simulation produces one realization of the stochastic variables T_{ij} , and the assumption of statistically homogeneity and isotropy of the early Universe source is then implemented through the average over shells for each wave number k . The applicability of Eq. (A.15) is limited to this (very reasonable) assumption.

We have demonstrated that the expression in Eq. (A.15) allows to compute the GW spectrum at present time, after performing an average over oscillations in time, for $t > t_{\text{fin}}$. However, in the simulations, one computes numerically the right hand side of Eq. (A.15) only until the end of the simulation at t_{end} , which is, in general, smaller than t_{fin} . Indeed, as explained in the main text, the GW sourcing by fluid perturbations can last several Hubble times, as the physical decay of the fluid bulk motion is determined by the kinematic viscosity, which is very small in the early Universe. Therefore, the numerical result will correctly represent the physical GW amplitude at a given mode k only if the latter has already reached its free-propagation regime by the time t_{end} , i.e., if its amplitude has already saturated. Otherwise, the numerical result only provides the GW amplitude that would be obtained misleadingly assuming that the source is abruptly switched off at t_{end} .

B Corrections to the kinetic energy for multiple bubbles

In this section, we study in more detail the convergence of the numerical *reference* simulations of multiple bubbles used for the analyses of Sec. 4 by comparing it to that of single-bubble simulations. This is useful because, for the latter, we know exact solutions to compare them to: indeed, we expect the self-similar profiles described in Ref. [49] to develop in the simulations. For reference, we show in Fig. 13 these profiles, for the PTs considered in the present work (see Tab. 1). In order to evaluate the effect of the numerical resolution, we compare the kinetic energy of a single bubble K_ξ obtained by direct integration of the self-similar profiles, with the kinetic energy obtained numerically before collisions, both from single-bubble and multiple-bubble runs. In Tab. 3, we also present for reference the values of the efficiency κ_ξ and the kinetic energy fraction $K_\xi \equiv \kappa_\xi \alpha / (1 + \alpha)$ for a subset of the parameters used in the simulations. We also provide the values of the shock formation time, $\tilde{\tau}_{\text{sh}} \equiv \beta R_* / \sqrt{K_\xi}$, which allows us to estimate the time at which we expect non-linearities to develop in the system.

We have previously defined the kinetic energy fraction K such that $\bar{\rho} K(\tilde{t}) \equiv \langle \rho_{\text{kin}}(\mathbf{x}, \tilde{t}) \rangle$, where $\langle \rho_{\text{kin}} \rangle$ corresponds to the kinetic energy density averaged over the simulation volume V . However, we note that K_ξ for single bubbles, defined in Eq. (2.19), is taken as the average of the kinetic energy density fraction induced by a single bubble over the broken-phase volume. Then, defining the ratio of the volume in the broken phase (bp) to the total volume,

$$\mathcal{V}(\tilde{t}) = \frac{V_{\text{bp}}}{V}, \quad (\text{B.1})$$

we can define the analog of K_ξ for multiple bubbles as the ratio $K(\tilde{t})/\mathcal{V}(\tilde{t})$. Before fluid shells collide, and in the limit of infinite resolution, this ratio should be identical to K_ξ after a very short transient period, over which the fluid profiles develop. Deviations from K_ξ before collisions are thus artifacts due to numerical inaccuracy. We plot the ratio

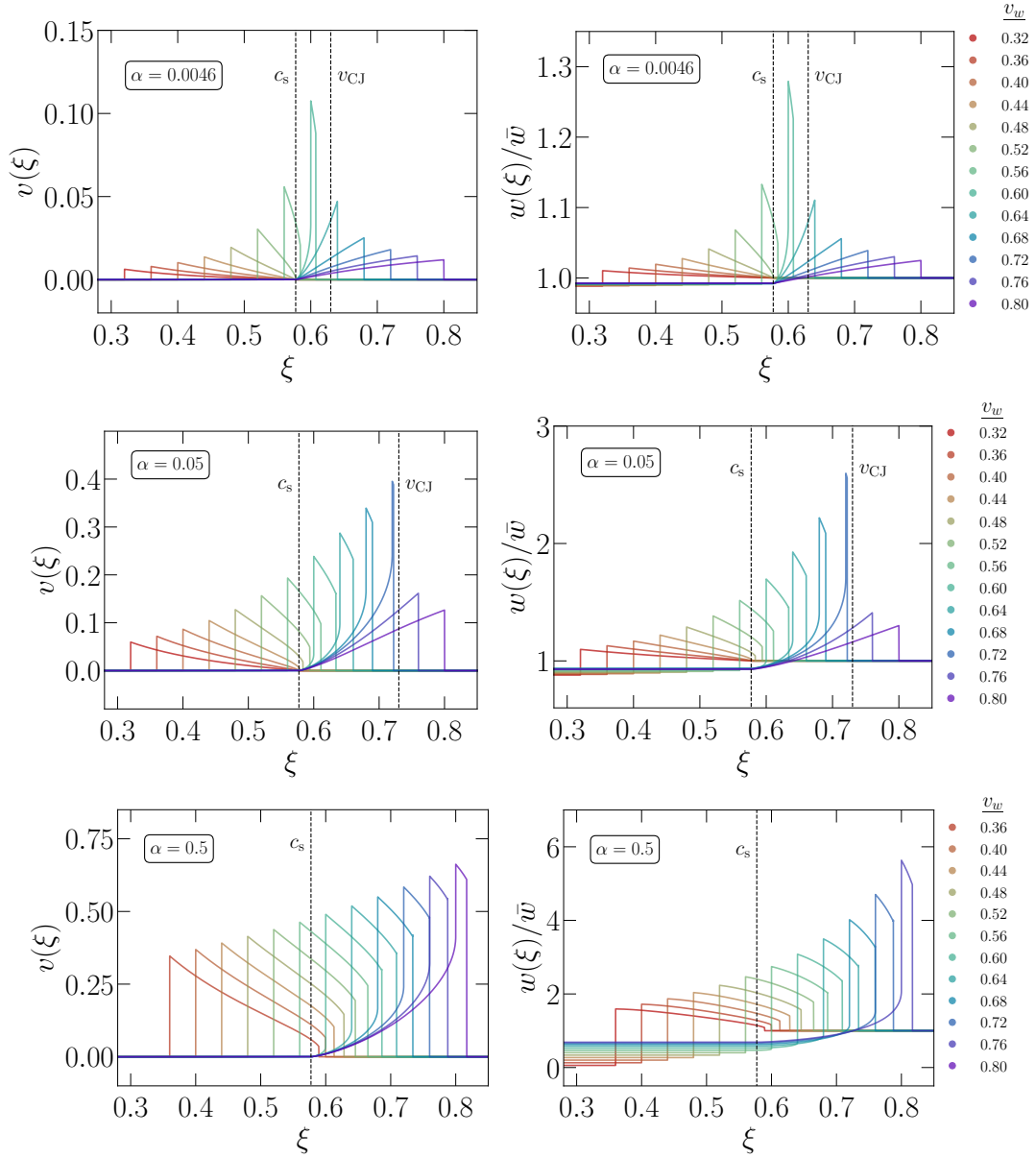


Figure 13. One-dimensional self-similar profiles of the fluid velocity (left columns) and enthalpy (right columns) perturbations for a single bubble as a function of $\xi \equiv r/(t - t_n)$ for weak (upper panel), intermediate (middle panel), and strong (lower panel) PTs, and for a range of wall velocities. The profiles are computed using COSMOGW [84]. Vertical dashed lines indicate the speed of sound c_s and the Chapman-Jouget velocity v_{CJ} [49]. These profiles correspond to the set of simulated PTs presented in this work (see Tab. 1).

$K(\tilde{t})/[\mathcal{V}(\tilde{t})K_\xi]$ as solid lines in Fig. 14 for all four resolutions $N \in \{64, 128, 256, 512\}$. Orange stars mark the time of first collision \tilde{t}_{coll} , where we assume that the maximum possible degree of convergence of the self-similar profiles is reached, as at later times collisions affect the development of the fluid-shell profiles. From Fig. 14, one can appreciate that $K(\tilde{t})/\mathcal{V}(\tilde{t})$ largely differs from K_ξ even before the collision time, for the parameter sets for which the self similar profiles approach thin hybrids, which is a clear effect of under-resolution. We show in Fig. 15 the single-bubble profiles found in the simulations at $\tilde{t}_{\text{coll}} - \tilde{t}_n$, where \tilde{t}_n is the time of nucleation, compared to the expected ones in the limit of infinite resolution, already shown in Fig. 13. We note that in the *single-bubble* runs, the accuracy of the self-similar profiles keeps improving at times after \tilde{t}_{coll} , as can be seen by the fact that the dashed lines in Fig. 14 become closer to one (see also discussion in Ref. [58]).

In the multiple-bubble runs, we can similarly define $\bar{\rho} K_i(\tilde{t}) = \langle \rho_{\text{kin},i}(\mathbf{x}, \tilde{t}) \rangle$ as the kinetic energy fraction of each of the single bubbles i before their corresponding first collision, and define the ratio $K_i(\tilde{t})/\mathcal{V}_i(\tilde{t})$, where \mathcal{V}_i corresponds to the fractional broken-phase volume occupied by each bubble i . To monitor the time-dependence of K_i , we simulate single bubbles nucleated at the center of the simulation box (see *single-bubble* runs in Tab. 1). As the convergence of the single-bubble profiles depends on the resolution in $\xi \equiv r/(t - t_i)$, where t_i is the nucleation time of the bubble i and r the radial distance to the nucleation center, we empirically find that doubling the resolution from N to $2N$ is equivalent to evaluating the profile at time $2(\tilde{t} - \tilde{t}_i)$ (see also discussion in Ref. [58]). Hence, the kinetic energy of single-bubble simulations (with $t_i = 0$) obeys $K_i^{2N}(\tilde{t})/\mathcal{V}_i(\tilde{t}) = K_i^N(2\tilde{t})/\mathcal{V}_i(\tilde{t})$ to an

| α | v_w | κ_ξ | K_ξ | $\tilde{\tau}_{\text{sh}}$ |
|----------|-------|-----------------------|-----------------------|----------------------------|
| 0.0046 | 0.36 | 9.73×10^{-3} | 4.46×10^{-5} | 253.34 |
| | 0.44 | 1.68×10^{-2} | 7.69×10^{-5} | 192.89 |
| | 0.52 | 3.79×10^{-2} | 1.73×10^{-4} | 128.44 |
| | 0.60 | 1.40×10^{-1} | 6.40×10^{-4} | 69.48 |
| | 0.68 | 2.70×10^{-2} | 1.24×10^{-4} | 179.17 |
| | 0.76 | 1.50×10^{-2} | 6.87×10^{-5} | 268.51 |
| 0.05 | 0.36 | 9.10×10^{-2} | 4.33×10^{-3} | 25.69 |
| | 0.44 | 1.36×10^{-1} | 6.47×10^{-3} | 21.02 |
| | 0.52 | 2.11×10^{-1} | 1.00×10^{-2} | 16.87 |
| | 0.60 | 3.30×10^{-1} | 1.57×10^{-2} | 14.02 |
| | 0.68 | 3.43×10^{-1} | 1.63×10^{-2} | 15.58 |
| | 0.76 | 1.55×10^{-1} | 7.40×10^{-2} | 25.88 |
| 0.5 | 0.36 | 4.66×10^{-1} | 1.55×10^{-1} | 4.29 |
| | 0.44 | 5.33×10^{-1} | 1.78×10^{-1} | 4.01 |
| | 0.52 | 5.91×10^{-1} | 1.97×10^{-1} | 3.81 |
| | 0.60 | 6.46×10^{-1} | 2.15×10^{-1} | 3.79 |
| | 0.68 | 6.89×10^{-1} | 2.30×10^{-1} | 4.16 |
| | 0.76 | 7.00×10^{-1} | 2.33×10^{-1} | 4.61 |

Table 3. Values of the efficiency κ_ξ , the kinetic energy fraction $K_\xi \equiv \kappa_\xi \alpha/(1+\alpha)$, and the estimated shock formation time $\tilde{\tau}_{\text{sh}} \equiv \beta R_*/\sqrt{K_\xi}$ of single bubbles for a subset of the parameters used in the simulations (see Tab. 1). These values have been computed numerically using COSMOGW [84]. For comparison to $\tilde{\tau}_{\text{sh}}$, the simulations run for durations $\tilde{t}_{\text{end}} = 32$ in units of β^{-1} and the PT ends at the time $\tilde{t}_0 \simeq 10$.

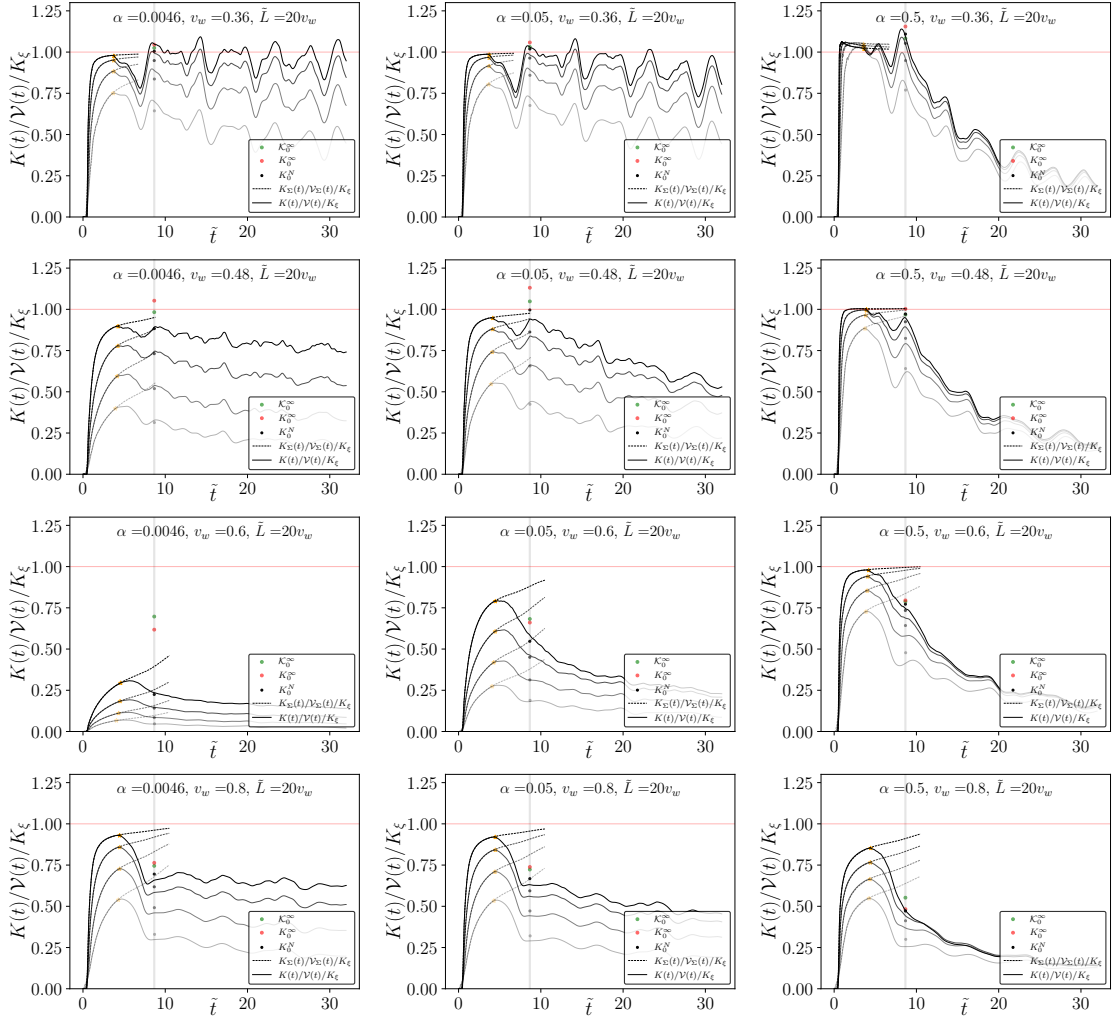


Figure 14. Time evolution of the kinetic energy fraction in the broken-phase volume $K(\tilde{t})/\mathcal{V}(\tilde{t})$ for multiple-bubble *reference* simulations (solid lines), normalized by the single-bubble K_ξ (see values in Tab. 3), for different resolutions $N = \{64, 128, 256, 512\}$ in increased opacity, and fixed box size $\tilde{L}/v_w = 20$. Results are shown for weak (left columns), intermediate (middle columns), and strong (right columns) PTs, and for a range of wall velocities $v_w = \{0.36, 0.48, 0.6, 0.8\}$. Dashed lines correspond to the ratio $K_\Sigma(\tilde{t})/\mathcal{V}_\Sigma(\tilde{t})$ computed from the single-bubble simulations, such that the departure between the solid and dashed lines indicates the time \tilde{t}_{coll} when the first fluid-shell collision takes place in the multiple-bubble simulations. This time is marked with orange stars and the corresponding numerical self-similar profiles obtained are shown in Fig. 15. Black dots are the values of K_0 obtained from the fit $K(\tilde{t}) = K_0(\tilde{t}/\tilde{t}_0)^{-b}$ studied in Sec. 4.2 for different N . Red and green dots correspond to the estimated values K_0 [see Eq. (B.4)] and K_0^∞ (obtained from the convergence analysis of Sec. 4.1). Orange stars also correspond to the inverse of the factor \mathcal{S} at the collision time \tilde{t}_{coll} , used to compute K_0 from K_0 [see Eq. (B.4)].

excellent degree and it suffices to run single-bubble simulations for the largest resolution $N = 512$. These simulations are run approximately until the front of the fluid profile collides with its own mirror image at the edge of the simulation box, which occurs around

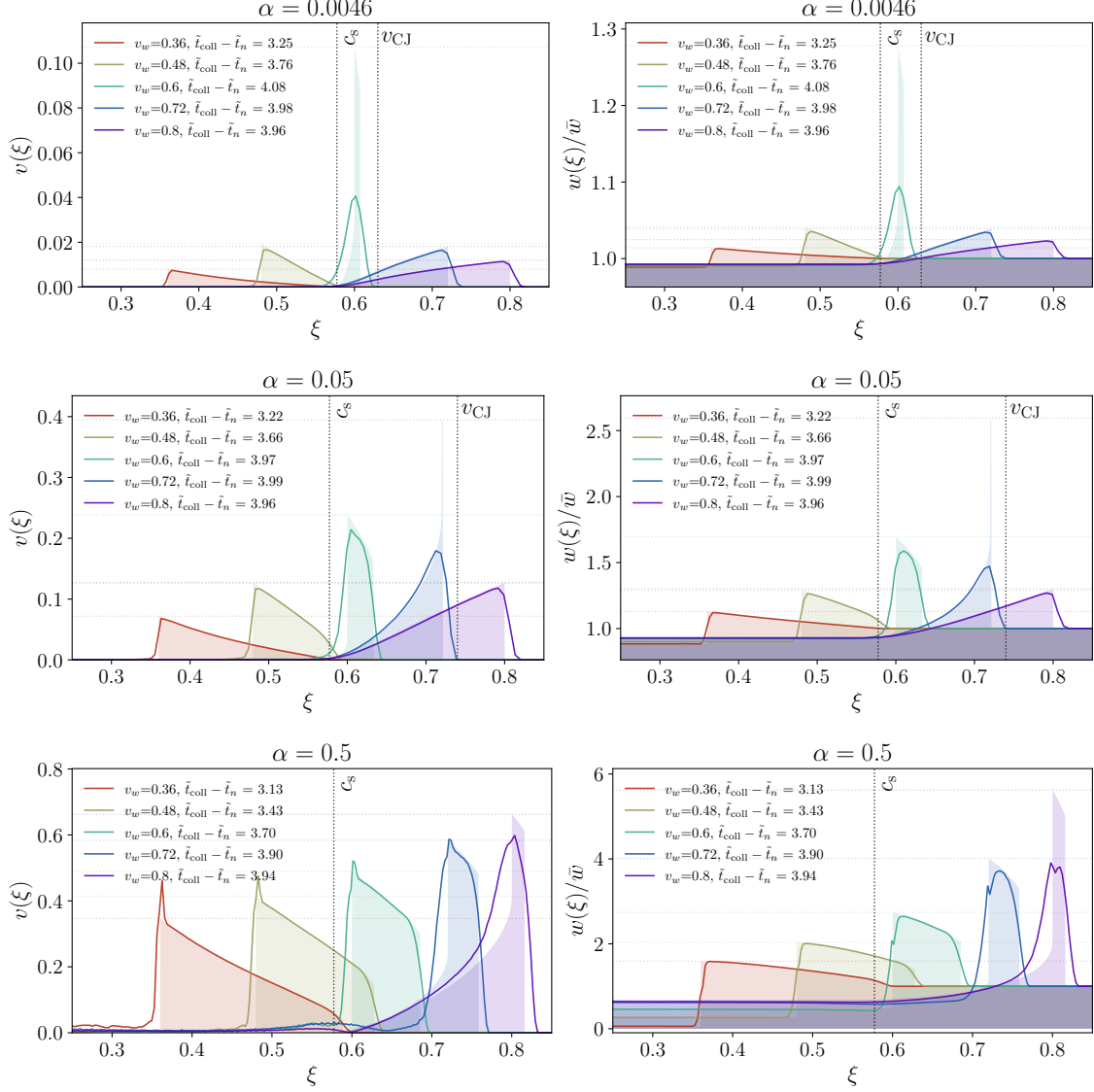


Figure 15. Self-similar profiles (filled regions) for fluid velocity (left columns) and enthalpy (right columns) perturbations for a single bubble as a function of $\xi \equiv r/(t - t_n)$ for weak (upper panel), intermediate (middle panel), and strong (lower panel) PTs, for a selection of representative wall velocities, over-plotted with the fluid profiles achieved by the *single-bubble* and *reference* simulations at the collision time, \tilde{t}_{coll} , when the kinetic energy fraction starts to be affected by collisions. The box size is $\tilde{L}/v_w = 20$ and $N = 512$. The self-similar profiles are a subset of those shown in Fig. 13.

$\tilde{t}_{\text{end}}^{\text{sb}} = \tilde{L}v_w/[2 \max(c_s, v_w)]$ and determines the end of the dashed lines in Fig. 14.

Then, in the full simulations and before fluid shells collide, the state of the simulation is exactly the superposition of single bubbles nucleated at times $\tilde{t}_i < \tilde{t}$ in the bubble nucleation history. We thus construct the sum

$$K_{\Sigma}(\tilde{t}) \equiv \sum_{i:\{\tilde{t}_i < \tilde{t}\}} K_i(\tilde{t} - \tilde{t}_i), \quad (\text{B.2})$$

which corresponds to the expected kinetic energy fraction for multiple-bubble simulations in the hypothetical case that no bubble would collide, following the bubble nucleation history up to time \tilde{t} . Then, before the first fluid-shell collision occurs, we have that $K_{\Sigma}(\tilde{t}) = K(\tilde{t})$, while $K(\tilde{t})$ starts to deviate from $K_{\Sigma}(\tilde{t})$ after the first collision at \tilde{t}_{coll} . Similarly, we can construct the fractional broken-phase volume occupied by the superposition of single bubbles as

$$\mathcal{V}_{\Sigma}(\tilde{t}) \equiv \sum_{i:\{\tilde{t}_i < \tilde{t}\}} \mathcal{V}_i(\tilde{t} - \tilde{t}_i), \quad (\text{B.3})$$

which can become larger than one, as it ignores interactions between bubbles. However, the ratio $K_{\Sigma}/\mathcal{V}_{\Sigma}$ is bounded by K_{ξ} .¹¹

We plot the time evolution of the ratio $K_{\Sigma}/\mathcal{V}_{\Sigma}$ as dotted lines in Fig. 14, using the nucleation history of the *reference* multiple-bubble simulations with $\tilde{L}/v_w = 20$. As for $K(\tilde{t})/\mathcal{V}(\tilde{t})$, the under-resolution of the self-similar profiles for the parameter sets leading to hybrids causes the ratio $K_{\Sigma}/\mathcal{V}_{\Sigma}$ to be very different from K_{ξ} in these cases. However, this quantity indicates the global degree of convergence of the full multiple-bubble simulations in the hypothetical case that all bubbles keep evolving without interacting with each other. Therefore, contrary to $K(\tilde{t})/\mathcal{V}(\tilde{t})$, this ratio does approach K_{ξ} as the simulation proceeds after collisions and the resolution in ξ improves. Furthermore, as expected, the ratio K/\mathcal{V} computed in the multiple-bubble simulations is initially identical to $K_{\Sigma}/\mathcal{V}_{\Sigma}$ at times $\tilde{t} < \tilde{t}_{\text{coll}}$. However, as collisions take place, we clearly see in Fig. 14 that these quantities deviate from each other, as a consequence of mainly four phenomena: (1) the self-similar profiles stop converging towards the expected ones when collisions take place; (2) oscillatory conversion between thermal and kinetic energy due to collisions and the development of sound waves; (3) upon and after collisions, the fluid self- and inter-shell interactions may be non-linear and result in the kinetic energy decay studied in Sec. 4.2, which is again affected by the previous two effects; and (4) numerical viscosity also results in damping of the kinetic energy. The first and last phenomena are purely numerical, while the remaining two are physical effects, which might also be affected by the numerical accuracy.

Because of (1), and since the kinetic energy of the uncollided bubbles is in general underestimated with respect to K_{ξ} because of under-resolution, the value of $K(\tilde{t})/\mathcal{V}(\tilde{t})$ found after a short transient period dominated by collisions is in general underestimated. This quantity is very relevant for us, since it determines the GW production in the period of time in which we calculate it, namely in the last part of the simulation from $\tilde{t}_{\text{init}} = 16$

¹¹This is the case for all the considered PTs, with the exception of strong PTs with $v_w = 0.36$ and $v_w = 0.4$, where values $K_{\Sigma}/\mathcal{V}_{\Sigma} \gtrsim K_{\xi}$ are found before collisions due to numerical inaccuracy (see Fig. 14).

to $\tilde{t}_{\text{end}} = 32$. The convergence analysis performed in this appendix allows us to find a way to attempt to compensate for the underestimation of the kinetic energy fraction due to insufficient resolution at $\tilde{t} > \tilde{t}_{\text{coll}}$: namely, multiplying $K(\tilde{t})$ by the factor $\mathcal{S} = \mathcal{V}(\tilde{t}_{\text{coll}}) K_\xi / K(\tilde{t}_{\text{coll}})$, effectively correcting it to the expected value K_ξ at the time when collisions take place. In particular, the kinetic energy fraction at the time when the PT ends, \tilde{t}_0 , can be corrected to the following value

$$\mathcal{K}_0 = \mathcal{S} K_0 = \frac{\mathcal{V}(\tilde{t}_{\text{coll}}) K_\xi}{K(\tilde{t}_{\text{coll}})} K_0. \quad (\text{B.4})$$

In Fig. 3, we plot \mathcal{K}_0 obtained for numerical resolutions $N \in \{64, 128, 256, 512\}$. The relative differences between \mathcal{K}_0 in the $N = 512$ simulations and \mathcal{K}_0 in the $N = 256$ simulations are smaller than the respective ones for K_0 . Therefore, \mathcal{K}_0 seems to be a more robust estimate of the actual value of K_0 in the continuum limit. We note that the computation of \mathcal{K}_0 takes into account the expected convergence of the numerical results of the self-similar profiles. Furthermore, the resulting values of \mathcal{K}_0 are closer to K_ξ than K_0^∞ and therefore are more conservative estimates, reducing potential deviations with respect to K_ξ that could originate from our extrapolation scheme. However, one needs to keep in mind that the under-resolution at the time of collisions might strongly affect the following evolution of the kinetic energy, when non-linearities dominate the dynamics.

C Preliminary results for vorticity

In this section, we present some preliminary measurements of the fluid vorticity in our numerical simulations.

C.1 Vorticity on the lattice

The vorticity is computed as

$$\nabla \times \mathbf{v} = \left(\frac{\partial v_z}{\partial y} - \frac{\partial v_y}{\partial z} \right) \hat{\mathbf{x}} + \left(\frac{\partial v_x}{\partial z} - \frac{\partial v_z}{\partial x} \right) \hat{\mathbf{y}} + \left(\frac{\partial v_y}{\partial x} - \frac{\partial v_x}{\partial y} \right) \hat{\mathbf{z}}. \quad (\text{C.1})$$

On the lattice, we approximate the derivatives using first-order central differences,

$$\frac{\partial v_i}{\partial \tilde{x}_j}(\tilde{\mathbf{x}}) \simeq \frac{v_i[\tilde{\mathbf{x}} + \delta \tilde{x} \hat{x}_j] - v_i[\tilde{\mathbf{x}} - \delta \tilde{x} \hat{x}_j]}{2 \delta \tilde{x}}, \quad (\text{C.2})$$

where $\delta \tilde{x}$ is the uniform grid spacing.

With this choice of derivative operator, the magnitude of the curl $|\tilde{\nabla} \times \mathbf{v}|$ is computed at every grid point. 2D simulation slices at different times are shown in the lower panels of Fig. 1. Note that the definition of the numerical derivative operator of Eq. (C.2) inevitably introduces potentially large vorticity at points where the velocity field varies considerably from lattice site to lattice site. This occurs, e.g., around the bubble shock fronts where discontinuities are present. Ideally, the velocity gradients are aligned with the radial direction, in which case no vortical component is present. However, on the lattice, artifacts may arise from the discretization, causing rather strong vorticity to appear at and just around

the bubble walls. This is clearly seen in the lower left frame of Fig. 1. The numerical nature of this vorticity is nevertheless clear from the observation that the vortical structure, as we traverse around bubble wall, is seen to inherit the symmetry of the lattice (see, in particular, the largest bubble in the center). Furthermore, mostly small but spurious oscillations of the fluid velocity occur at the bubble wall interface. These oscillations additionally give rise to extremely local but very steep velocity gradients, potentially showing up as spurious vorticity with large amplitude, confined to very small scales.

In the lower panel of Fig. 1 it is observed that production of vorticity occurs, upon collisions, at the interface of a sound shell from one bubble crossing over the bubble wall of another, as seen, e.g., immediately to the right of the top section of the central bubble in the left column. The velocity field in the upper panel is included to make vorticity production possible to correlate with the velocity field by eye. In this sense, the resulting vorticity pattern initially appears to track the *sweeping* of this sound-shell-bubble-wall-crossing interface over time.

We have described the expected and observed presence of spurious vorticity components associated with the choice of the derivative operator and the lattice structure, and spurious oscillations around the bubble wall interface. These are very localized effects and do not contribute meaningfully to large-scale vorticity correlated over macroscopic scales. Therefore, vorticity components that emerge from numerically induced oscillations and limited grid resolution are expected to contribute mostly to the UV part of the velocity spectra. The development of a transverse vortical component should be visible in the spectra of the velocity fields decomposed into longitudinal and transverse contributions, as we present in the following (see Fig. 16). In particular, physical macroscopic contributions should distinguish themselves from numerical contributions through a separation of scales.

C.2 Velocity power spectra

We generate the Fourier transform $v(\mathbf{k})$ of the fluid velocity field and then extract the power spectral density from the two-point correlation in Fourier space [106]

$$\langle v_i(\mathbf{k}) v_i^*(\mathbf{k}') \rangle = (2\pi)^3 \delta^3(\mathbf{k} - \mathbf{k}') P_v(k), \quad (\text{C.3})$$

where the ensemble average is performed over momenta with the same absolute value $|\mathbf{k}| = |\mathbf{k}'|$ due to statistical homogeneity and isotropy. We also construct the power spectral density of the longitudinal modes

$$\langle \hat{k}_i v_i(\mathbf{k}) \hat{k}'_j v_j^*(\mathbf{k}') \rangle = (2\pi)^3 \delta^3(\mathbf{k} - \mathbf{k}') P_{\parallel}(k), \quad (\text{C.4})$$

where $\hat{\mathbf{k}} = \text{saw}(\mathbf{k})/|\text{saw}(\mathbf{k})|$ is a unit vector according to the *saw* description, as discussed in Sec. 3.1 [see Eq. (3.3)]. Likewise, we extract the vortical component of the spectra

$$\left\langle [\hat{\mathbf{k}} \times \mathbf{v}(\mathbf{k})]_i [\hat{\mathbf{k}}' \times \mathbf{v}^*(\mathbf{k}')]_i \right\rangle = (2\pi)^3 \delta^3(\mathbf{k} - \mathbf{k}') P_{\perp}(k), \quad (\text{C.5})$$

such that $P_v(k) = P_{\perp}(k) + P_{\parallel}(k)$.

Figure 16 shows the power in longitudinal and vortical modes as well as the fraction of power in vortical modes for strong PTs. The power in longitudinal modes builds up

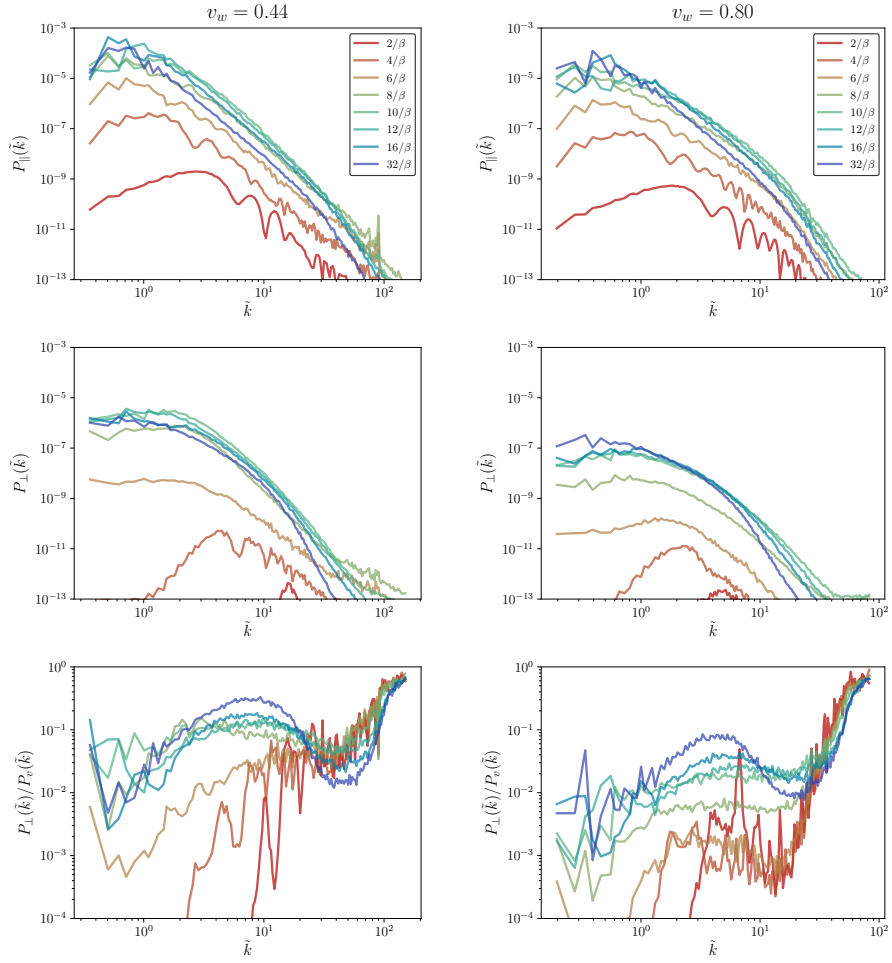


Figure 16. Transverse $P_{\perp}(k)$ and longitudinal $P_{\parallel}(k)$ velocity power spectra (in arbitrary units) of the fluid for a strong PT ($\alpha = 0.5$) with wall velocities $v_w = 0.44$ (left columns) and $v_w = 0.8$ (right columns). The panels show the power in longitudinal (top) and vortical (middle) modes as well as the fraction of power in vortical modes (bottom), $P_{\perp}(k)/P_v(k)$. The different lines correspond to different times in the simulation $\tilde{t} \in (2, 32)$. For reference, we remind that the first bubbles nucleate around $\tilde{t} \simeq 0$, the first collisions happen around $\tilde{t} \simeq 5$, and the simulation is filled with the broken phase at $\tilde{t}_0 \simeq 10$.

when the first bubbles nucleate while vorticity requires collisions, as expected. There are some artifacts in the UV even before collisions, which result from the discretization of space on a grid. Overall, the power in vorticity can reach values of around $P_{\perp}/P_v \simeq 0.3$ for the deflagration ($v_w = 0.44$), while this fraction is somewhat smaller, $P_{\perp}/P_v \simeq 0.1$, for the hybrid ($v_w = 0.80$). Still, a sizable fraction of vorticity is observable in both cases. Moreover, the power spectra in vortical modes appear somewhat less steep than the ones in longitudinal modes. All this is consistent with the hypothesis that the energy loss observed over time for strong PTs is due to the decay of fluid kinetic energy into vortical motion and eventually turbulence. This point deserves further attention in the future. We also have

obtained velocity power spectra for weak and intermediate PTs, finding that $P_{\perp}/P_v < 10^{-3}$ for those scenarios. This indicates that turbulence becomes progressively more important the stronger the PT, and that for strong PTs ($\alpha = 0.5$) it already has a dominant role in determining the hydrodynamical evolution after the PT ends. This observation underlines the importance of fully non-linear 3D simulations.

References

- [1] LIGO SCIENTIFIC, VIRGO collaboration, *Observation of Gravitational Waves from a Binary Black Hole Merger*, *Phys. Rev. Lett.* **116** (2016) 061102 [[1602.03837](#)].
- [2] LIGO SCIENTIFIC, VIRGO collaboration, *GW151226: Observation of Gravitational Waves from a 22-Solar-Mass Binary Black Hole Coalescence*, *Phys. Rev. Lett.* **116** (2016) 241103 [[1606.04855](#)].
- [3] LIGO SCIENTIFIC, VIRGO collaboration, *GW170817: Observation of Gravitational Waves from a Binary Neutron Star Inspiral*, *Phys. Rev. Lett.* **119** (2017) 161101 [[1710.05832](#)].
- [4] KAGRA, VIRGO, LIGO SCIENTIFIC collaboration, *GWTC-3: Compact Binary Coalescences Observed by LIGO and Virgo during the Second Part of the Third Observing Run*, *Phys. Rev. X* **13** (2023) 041039 [[2111.03606](#)].
- [5] EPTA, INPTA: collaboration, *The second data release from the European Pulsar Timing Array - III. Search for gravitational wave signals*, *Astron. Astrophys.* **678** (2023) A50 [[2306.16214](#)].
- [6] NANOGrav collaboration, *The NANOGrav 15 yr Data Set: Evidence for a Gravitational-wave Background*, *Astrophys. J. Lett.* **951** (2023) L8 [[2306.16213](#)].
- [7] D.J. Reardon et al., *Search for an Isotropic Gravitational-wave Background with the Parkes Pulsar Timing Array*, *Astrophys. J. Lett.* **951** (2023) L6 [[2306.16215](#)].
- [8] H. Xu et al., *Searching for the Nano-Hertz Stochastic Gravitational Wave Background with the Chinese Pulsar Timing Array Data Release I*, *Res. Astron. Astrophys.* **23** (2023) 075024 [[2306.16216](#)].
- [9] EPTA collaboration, *The second data release from the European Pulsar Timing Array: IV. Implications for massive black holes, dark matter and the early Universe*, [2306.16227](#).
- [10] NANOGrav collaboration, *The NANOGrav 15 yr Data Set: Search for Signals from New Physics*, *Astrophys. J. Lett.* **951** (2023) L11 [[2306.16219](#)].
- [11] LISA collaboration, *Laser Interferometer Space Antenna*, [1702.00786](#).
- [12] M. Colpi et al., *LISA Definition Study Report*, [2402.07571](#).
- [13] eLISA collaboration, *The Gravitational Universe*, [1305.5720](#).
- [14] P. Amaro-Seoane, H. Audley, S. Babak, J. Baker, E. Barausse, P. Bender et al., *Laser interferometer space antenna*, 2017.
- [15] LISA COSMOLOGY WORKING GROUP collaboration, *Cosmology with the Laser Interferometer Space Antenna*, [2204.05434](#).
- [16] M. Maggiore, *Gravitational Waves. Vol. 2: Astrophysics and Cosmology*, Oxford University Press (3, 2018).

- [17] C. Caprini and D.G. Figueroa, *Cosmological Backgrounds of Gravitational Waves*, *Class. Quant. Grav.* **35** (2018) 163001 [[1801.04268](#)].
- [18] E. Witten, *Cosmic Separation of Phases*, *Phys. Rev.* **D30** (1984) 272.
- [19] K. Kajantie, M. Laine, K. Rummukainen and M.E. Shaposhnikov, *Is there a hot electroweak phase transition at $m_H \gtrsim m_W$?*, *Phys. Rev. Lett.* **77** (1996) 2887 [[hep-ph/9605288](#)].
- [20] M. Gurtler, E.-M. Ilgenfritz and A. Schiller, *Where the electroweak phase transition ends*, *Phys. Rev. D* **56** (1997) 3888 [[hep-lat/9704013](#)].
- [21] F. Csikor, Z. Fodor and J. Heitger, *Endpoint of the hot electroweak phase transition*, *Phys. Rev. Lett.* **82** (1999) 21 [[hep-ph/9809291](#)].
- [22] C. Caprini et al., *Detecting gravitational waves from cosmological phase transitions with LISA: an update*, *JCAP* **03** (2020) 024 [[1910.13125](#)].
- [23] S.R. Coleman, *The Fate of the False Vacuum. 1. Semiclassical Theory*, *Phys. Rev. D* **15** (1977) 2929.
- [24] A.D. Linde, *Fate of the False Vacuum at Finite Temperature: Theory and Applications*, *Phys. Lett. B* **100** (1981) 37.
- [25] P.J. Steinhardt, *Relativistic Detonation Waves and Bubble Growth in False Vacuum Decay*, *Phys. Rev. D* **25** (1982) 2074.
- [26] V.A. Kuzmin, V.A. Rubakov and M.E. Shaposhnikov, *On the Anomalous Electroweak Baryon Number Nonconservation in the Early Universe*, *Phys. Lett. B* **155** (1985) 36.
- [27] A.G. Cohen, D.B. Kaplan and A.E. Nelson, *Progress in electroweak baryogenesis*, *Ann. Rev. Nucl. Part. Sci.* **43** (1993) 27 [[hep-ph/9302210](#)].
- [28] V.A. Rubakov and M.E. Shaposhnikov, *Electroweak baryon number nonconservation in the early universe and in high-energy collisions*, *Usp. Fiz. Nauk* **166** (1996) 493 [[hep-ph/9603208](#)].
- [29] A. Riotto and M. Trodden, *Recent progress in baryogenesis*, *Ann. Rev. Nucl. Part. Sci.* **49** (1999) 35 [[hep-ph/9901362](#)].
- [30] D.E. Morrissey and M.J. Ramsey-Musolf, *Electroweak baryogenesis*, *New J. Phys.* **14** (2012) 125003 [[1206.2942](#)].
- [31] A. Kosowsky, M.S. Turner and R. Watkins, *Gravitational radiation from colliding vacuum bubbles*, *Phys. Rev.* **D45** (1992) 4514.
- [32] A. Kosowsky, M.S. Turner and R. Watkins, *Gravitational waves from first order cosmological phase transitions*, *Phys. Rev. Lett.* **69** (1992) 2026.
- [33] A. Kosowsky and M.S. Turner, *Gravitational radiation from colliding vacuum bubbles: envelope approximation to many bubble collisions*, *Phys. Rev.* **D47** (1993) 4372 [[astro-ph/9211004](#)].
- [34] M. Kamionkowski, A. Kosowsky and M.S. Turner, *Gravitational radiation from first order phase transitions*, *Phys. Rev.* **D49** (1994) 2837 [[astro-ph/9310044](#)].
- [35] C. Caprini, R. Durrer and G. Servant, *Gravitational wave generation from bubble collisions in first-order phase transitions: An analytic approach*, *Phys. Rev. D* **77** (2008) 124015 [[0711.2593](#)].

- [36] S.J. Huber and T. Konstandin, *Gravitational Wave Production by Collisions: More Bubbles*, *JCAP* **0809** (2008) 022 [[0806.1828](#)].
- [37] T. Konstandin, *Gravitational radiation from a bulk flow model*, *JCAP* **1803** (2018) 047 [[1712.06869](#)].
- [38] R. Jinno and M. Takimoto, *Gravitational waves from bubble dynamics: Beyond the Envelope*, *JCAP* **1901** (2019) 060 [[1707.03111](#)].
- [39] D. Cutting, M. Hindmarsh and D.J. Weir, *Gravitational waves from vacuum first-order phase transitions: from the envelope to the lattice*, *Phys. Rev. D* **97** (2018) 123513 [[1802.05712](#)].
- [40] M. Hindmarsh, S.J. Huber, K. Rummukainen and D.J. Weir, *Gravitational waves from the sound of a first order phase transition*, *Phys. Rev. Lett.* **112** (2014) 041301 [[1304.2433](#)].
- [41] J.M. Quashnock, A. Loeb and D.N. Spergel, *Magnetic Field Generation During the Cosmological QCD Phase Transition*, *Astrophys. J. Lett.* **344** (1989) L49.
- [42] A. Brandenburg, K. Enqvist and P. Olesen, *Large scale magnetic fields from hydromagnetic turbulence in the very early universe*, *Phys. Rev. D* **54** (1996) 1291 [[astro-ph/9602031](#)].
- [43] J. Ahonen and K. Enqvist, *Electrical conductivity in the early universe*, *Phys. Lett. B* **382** (1996) 40 [[hep-ph/9602357](#)].
- [44] P.B. Arnold, G.D. Moore and L.G. Yaffe, *Transport coefficients in high temperature gauge theories. 1. Leading log results*, *JHEP* **11** (2000) 001 [[hep-ph/0010177](#)].
- [45] B. von Harling and G. Servant, *QCD-induced Electroweak Phase Transition*, *JHEP* **01** (2018) 159 [[1711.11554](#)].
- [46] D. Bodeker and G.D. Moore, *Electroweak Bubble Wall Speed Limit*, *JCAP* **05** (2017) 025 [[1703.08215](#)].
- [47] A. Kobakhidze, C. Lagger, A. Manning and J. Yue, *Gravitational waves from a supercooled electroweak phase transition and their detection with pulsar timing arrays*, *Eur. Phys. J. C* **77** (2017) 570 [[1703.06552](#)].
- [48] J. Ignatius, K. Kajantie, H. Kurki-Suonio and M. Laine, *The growth of bubbles in cosmological phase transitions*, *Phys. Rev. D* **49** (1994) 3854 [[astro-ph/9309059](#)].
- [49] J.R. Espinosa, T. Konstandin, J.M. No and G. Servant, *Energy Budget of Cosmological First-order Phase Transitions*, *JCAP* **06** (2010) 028 [[1004.4187](#)].
- [50] M. Hindmarsh, S.J. Huber, K. Rummukainen and D.J. Weir, *Numerical simulations of acoustically generated gravitational waves at a first order phase transition*, *Phys. Rev.* **D92** (2015) 123009 [[1504.03291](#)].
- [51] M. Hindmarsh, *Sound shell model for acoustic gravitational wave production at a first-order phase transition in the early Universe*, *Phys. Rev. Lett.* **120** (2018) 071301 [[1608.04735](#)].
- [52] M. Hindmarsh, S.J. Huber, K. Rummukainen and D.J. Weir, *Shape of the acoustic gravitational wave power spectrum from a first order phase transition*, [1704.05871](#).
- [53] P. Niksa, M. Schlexer and G. Sigl, *Gravitational Waves produced by Compressible MHD Turbulence from Cosmological Phase Transitions*, *Class. Quant. Grav.* **35** (2018) 144001 [[1803.02271](#)].
- [54] M. Hindmarsh and M. Hijazi, *Gravitational waves from first order cosmological phase transitions in the Sound Shell Model*, *JCAP* **1912** (2019) 062 [[1909.10040](#)].

- [55] A. Roper Pol, S. Mandal, A. Brandenburg, T. Kahniashvili and A. Kosowsky, *Numerical simulations of gravitational waves from early-universe turbulence*, *Phys. Rev. D* **102** (2020) 083512 [[1903.08585](#)].
- [56] R. Jinno, T. Konstandin and H. Rubira, *A hybrid simulation of gravitational wave production in first-order phase transitions*, *JCAP* **04** (2021) 014 [[2010.00971](#)].
- [57] J. Dahl, M. Hindmarsh, K. Rummukainen and D.J. Weir, *Decay of acoustic turbulence in two dimensions and implications for cosmological gravitational waves*, *Phys. Rev. D* **106** (2022) 063511 [[2112.12013](#)].
- [58] R. Jinno, T. Konstandin, H. Rubira and I. Stomberg, *Higgsless simulations of cosmological phase transitions and gravitational waves*, *JCAP* **02** (2023) 011 [[2209.04369](#)].
- [59] A. Roper Pol, S. Procacci and C. Caprini, *Characterization of the gravitational wave spectrum from sound waves within the sound shell model*, *Phys. Rev. D* **109** (2024) 063531 [[2308.12943](#)].
- [60] R. Sharma, J. Dahl, A. Brandenburg and M. Hindmarsh, *Shallow relic gravitational wave spectrum with acoustic peak*, *JCAP* **12** (2023) 042 [[2308.12916](#)].
- [61] J. Dahl, M. Hindmarsh, K. Rummukainen and D. Weir, *Primordial acoustic turbulence: three-dimensional simulations and gravitational wave predictions*, [2407.05826](#).
- [62] A. Kosowsky, A. Mack and T. Kahniashvili, *Gravitational radiation from cosmological turbulence*, *Phys. Rev. D* **66** (2002) 024030 [[astro-ph/0111483](#)].
- [63] G. Gogoberidze, T. Kahniashvili and A. Kosowsky, *The Spectrum of Gravitational Radiation from Primordial Turbulence*, *Phys. Rev. D* **76** (2007) 083002 [[0705.1733](#)].
- [64] C. Caprini, R. Durrer, T. Konstandin and G. Servant, *General Properties of the Gravitational Wave Spectrum from Phase Transitions*, *Phys. Rev. D* **79** (2009) 083519 [[0901.1661](#)].
- [65] C. Caprini, R. Durrer and G. Servant, *The stochastic gravitational wave background from turbulence and magnetic fields generated by a first-order phase transition*, *JCAP* **12** (2009) 024 [[0909.0622](#)].
- [66] A. Roper Pol, A. Brandenburg, T. Kahniashvili, A. Kosowsky and S. Mandal, *The timestep constraint in solving the gravitational wave equations sourced by hydromagnetic turbulence*, *Geophys. Astrophys. Fluid Dynamics* **114** (2020) 130 [[1807.05479](#)].
- [67] T. Kahniashvili, A. Brandenburg, G. Gogoberidze, S. Mandal and A. Roper Pol, *Circular polarization of gravitational waves from early-Universe helical turbulence*, *Phys. Rev. Res.* **3** (2021) 013193 [[2011.05556](#)].
- [68] A. Brandenburg, E. Clarke, Y. He and T. Kahniashvili, *Can we observe the QCD phase transition-generated gravitational waves through pulsar timing arrays?*, *Phys. Rev. D* **104** (2021) 043513 [[2102.12428](#)].
- [69] A. Brandenburg, G. Gogoberidze, T. Kahniashvili, S. Mandal, A. Roper Pol and N. Shenoy, *The scalar, vector, and tensor modes in gravitational wave turbulence simulations*, *Class. Quant. Grav.* **38** (2021) 145002 [[2103.01140](#)].
- [70] A. Roper Pol, S. Mandal, A. Brandenburg and T. Kahniashvili, *Polarization of gravitational waves from helical MHD turbulent sources*, *JCAP* **04** (2022) 019 [[2107.05356](#)].

- [71] A. Roper Pol, C. Caprini, A. Neronov and D. Semikoz, *Gravitational wave signal from primordial magnetic fields in the Pulsar Timing Array frequency band*, *Phys. Rev. D* **105** (2022) 123502 [[2201.05630](#)].
- [72] P. Auclair, C. Caprini, D. Cutting, M. Hindmarsh, K. Rummukainen, D.A. Steer et al., *Generation of gravitational waves from freely decaying turbulence*, [2205.02588](#).
- [73] R. Sharma and A. Brandenburg, *Low frequency tail of gravitational wave spectra from hydromagnetic turbulence*, *Phys. Rev. D* **106** (2022) 103536 [[2206.00055](#)].
- [74] R. Jinno and M. Takimoto, *Gravitational waves from bubble collisions: An analytic derivation*, *Phys. Rev. D* **95** (2017) 024009 [[1605.01403](#)].
- [75] U.-L. Pen and N. Turok, *Shocks in the Early Universe*, *Phys. Rev. Lett.* **117** (2016) 131301 [[1510.02985](#)].
- [76] A. Brandenburg, T. Kahniashvili, S. Mandal, A. Roper Pol, A.G. Tevzadze and T. Vachaspati, *The dynamo effect in decaying helical turbulence*, *Phys. Rev. Fluids.* **4** (2019) 024608 [[1710.01628](#)].
- [77] A. Brandenburg, T. Kahniashvili, S. Mandal, A. Roper Pol, A.G. Tevzadze and T. Vachaspati, *Evolution of hydromagnetic turbulence from the electroweak phase transition*, *Phys. Rev. D* **96** (2017) 123528 [[1711.03804](#)].
- [78] D. Cutting, M. Hindmarsh and D.J. Weir, *Vorticity, kinetic energy, and suppressed gravitational wave production in strong first order phase transitions*, *Phys. Rev. Lett.* **125** (2020) 021302 [[1906.00480](#)].
- [79] F. Giese, T. Konstandin and J. van de Vis, *Model-independent energy budget of cosmological first-order phase transitions: A sound argument to go beyond the bag model*, *JCAP* **07** (2020) 057 [[2004.06995](#)].
- [80] F. Giese, T. Konstandin, K. Schmitz and J. van de Vis, *Model-independent energy budget for LISA*, *JCAP* **01** (2021) 072 [[2010.09744](#)].
- [81] Y. Gouttenoire, R. Jinno and F. Sala, *Friction pressure on relativistic bubble walls*, *JHEP* **05** (2022) 004 [[2112.07686](#)].
- [82] A. Azatov, G. Barni, R. Petrossian-Byrne and M. Vanvlasselaer, *Quantisation Across Bubble Walls and Friction*, [2310.06972](#).
- [83] J. Ellis, M. Lewicki, J.M. No and V. Vaskonen, *Gravitational wave energy budget in strongly supercooled phase transitions*, *JCAP* **1906** (2019) 024 [[1903.09642](#)].
- [84] “COSMOGW, <https://github.com/CosmoGW/CosmoGW>.”
- [85] C. Caprini et al., *Science with the space-based interferometer eLISA. II: Gravitational waves from cosmological phase transitions*, *JCAP* **04** (2016) 001 [[1512.06239](#)].
- [86] R. Jinno, T. Konstandin, H. Rubira and J. van de Vis, *Effect of density fluctuations on gravitational wave production in first-order phase transitions*, *JCAP* **12** (2021) 019 [[2108.11947](#)].
- [87] S. Blasi, R. Jinno, T. Konstandin, H. Rubira and I. Stomberg, *Gravitational waves from defect-driven phase transitions: domain walls*, *JCAP* **10** (2023) 051 [[2302.06952](#)].
- [88] D.J. Weir, *Revisiting the envelope approximation: gravitational waves from bubble collisions*, *Phys. Rev. D* **93** (2016) 124037 [[1604.08429](#)].

- [89] K. Subramanian and J.D. Barrow, *Magnetohydrodynamics in the early universe and the damping of nonlinear Alfvén waves*, *Phys. Rev. D* **58** (1998) 083502 [[astro-ph/9712083](#)].
- [90] A. Roper Pol and A.S. Midiri, *Relativistic magnetohydrodynamics in the early Universe*, [2501.05732](#).
- [91] D. Bodeker and G.D. Moore, *Can electroweak bubble walls run away?*, *JCAP* **05** (2009) 009 [[0903.4099](#)].
- [92] T. Krajewski, M. Lewicki and M. Zych, *Bubble-wall velocity in local thermal equilibrium: hydrodynamical simulations vs analytical treatment*, *JHEP* **05** (2024) 011 [[2402.15408](#)].
- [93] H.-K. Guo, K. Sinha, D. Vagie and G. White, *Phase Transitions in an Expanding Universe: Stochastic Gravitational Waves in Standard and Non-Standard Histories*, *JCAP* **01** (2021) 001 [[2007.08537](#)].
- [94] C. Caprini, O. Pujolàs, H. Quelquejay-Leclerc, F. Rompineve and D.A. Steer, *Primordial gravitational wave backgrounds from phase transitions with next generation ground based detectors*, [2406.02359](#).
- [95] L. Giombi, J. Dahl and M. Hindmarsh, *Signatures of the speed of sound on the gravitational wave power spectrum from sound waves*, *JCAP* **01** (2025) 100 [[2409.01426](#)].
- [96] A. Roper Pol, A. Neronov, C. Caprini, T. Boyer and D. Semikoz, *LISA and γ -ray telescopes as multi-messenger probes of a first-order cosmological phase transition*, [2307.10744](#).
- [97] LISA COSMOLOGY WORKING GROUP collaboration, *Gravitational waves from first-order phase transitions in LISA: reconstruction pipeline and physics interpretation*, [2403.03723](#).
- [98] M.B. Hindmarsh, M. Lüben, J. Lumma and M. Pauly, *Phase transitions in the early universe*, *SciPost Phys. Lect. Notes* **24** (2021) 1 [[2008.09136](#)].
- [99] C. Gowling and M. Hindmarsh, *Observational prospects for phase transitions at LISA: Fisher matrix analysis*, *JCAP* **10** (2021) 039 [[2106.05984](#)].
- [100] C. Gowling, M. Hindmarsh, D.C. Hooper and J. Torrado, *Reconstructing physical parameters from template gravitational wave spectra at LISA: first order phase transitions*, *JCAP* **04** (2023) 061 [[2209.13551](#)].
- [101] A. Kurganov and E. Tadmor, *New high-resolution central schemes for nonlinear conservation laws and convection–diffusion equations*, *Journal of Computational Physics* **160** (2000) 241 .
- [102] M. Frigo and S.G. Johnson, *The Design and Implementation of FFTW3*, *IEEE Proc.* **93** (2005) 216.
- [103] C. Caprini and R. Durrer, *Gravitational waves from stochastic relativistic sources: Primordial turbulence and magnetic fields*, *Phys. Rev. D* **74** (2006) 063521 [[astro-ph/0603476](#)].
- [104] B.B. Kadomtsev and V.I. Petviashvili, *Acoustic Turbulence*, *Soviet Physics Doklady* **18** (1973) 115.
- [105] S. Weinberg, *Gravitation and cosmology*, John Wiley and Sons, New York (1972).
- [106] A.S. Monin and A.M. Yaglom, *Statistical fluid mechanics: Mechanics of turbulence*, vol. 2, MIT press, Cambridge, MA, USA. (1975).